# Quark and Gluon Jets at LEP

Mark Ian Parsons

Submitted for the degree of Doctor of Philosophy

The University of Edinburgh

1994

## Abstract

Using the large number of hadronic decays of the $Z^0$ particle recorded by the ALEPH detector at LEP between 1990 and 1992, a study of the properties of a sample of these events has been made. High transverse momentum lepton tagging has been used to identify the quark jets in three jet events. Evidence is shown that the angular distribution of the identified quark jets is described well by the theory of quantum chromodynamics. Using a log-likelihood statistical test a confidence level of 97% is obtained for the data to be in good agreement with JETSET Monte Carlo. An Abelian scalar gluon model is excluded. A separate study using symmetric three jet events and the same quark jet identification method is presented. This study compares quark and gluon jets in a configuration designed to minimise experimental biases. Gluon jets, when compared with a mixed flavour quark jet sample, are found to have a higher average charged track multiplicity ratio $N_g/N_q = 1.162 \pm 0.051$ (the error is predominately statistical). Evidence is also presented that they have a wider jet profile and that their particle energy spectrum is softer.

## Declaration

This work represents the efforts of many members of the ALEPH Collaboration at CERN, the European Centre for Particle Physics; the analysis and final results presented here are, however, entirely my own.

## Acknowledgements

I thank the Science and Engineering Research Council for their financial support of my studentship.

My main supervisor, Dr David Candlin, proved to be a constant source of help and encouragement. I thank him for giving me the chance to work on ALEPH and also for knowing when to leave me to my own devices and when to help and guide me. Dr Ken Peach and Mr Alan Walker deserve many thanks for their help and encouragement along the way. I am also grateful to our two research assistants, Liz and Owen, for many useful discussions.

At CERN, numerous physicists, engineers and technicians contribute to the LEP collider and the smooth running of ALEPH. My sincere thanks go to these people, who are too numerous to mention, but who have all helped to maintain the superb performance of both machines.

Whilst at CERN many fellow physicists gave their time freely to help me. Of particular note were Glen Cowan and Ramon Miquel of the QCD group who greatly increased my knowledge of QCD and were always ready to think about specific analysis problems I had encountered. Working on DALI with Hans Drevermann and Björn Nilsson resulted in a very enjoyable first year. I also thank Bill Maitland and Ann Moutoussi for their mutual support within the QCD group and Andy "professional code" Halley for making me write it.

Writing LEPTAG with Ingrid ten Have was an enlightening experience. I cannot thank her enough for the vast amount of help she has given me over the last three years, not least of which involved reading and commenting on this thesis.

Throughout my student years my parents have been a constant source of good advice, support, and pounds sterling. I thank them for all of this but most of all I thank them for always showing an interest in whatever I have done.

Finally, I thank Linda. My life over the last four years has involved several long absences from Edinburgh, little money, and very erratic hours, Linda has borne the brunt of these trials and it is to her that I dedicate this thesis along with my love and admiration.

To Linda

# Contents

# List of Figures

# List of Tables

# Chapter 1

# Introduction

> *It seems probable to me, that God in the Beginning form'd Matter in solid, massy, hard, impenetrable, moveable Particles ... and thus Nature will be very comfortable to herself and very simple, performing all the great Motions of the heavenly Bodies by the attraction of gravity ... and almost all the small ones of their Particles by some other attracting and repelling Powers ...*
>
> Isaac Newton, *Opticks* (1730)

The discovery that all the known matter of the Universe and its interactions can be described by a small number of elementary particles and four basic forces is one of the most important scientific achievements of all time. That Newton was already thinking along these lines more than 250 years ago is a startling insight into his genius. Today, those involved in particle physics research devote huge amounts of time, man-power, and ingenuity into studying these phenomena. That they should be able to do so is a tribute not just to the power of scientific reason but also to the combined will of all those who choose to support their endeavours.

The *Standard Model* of particles and interactions has evolved over the last 20 years into a highly successful framework containing the fundamental particles and their electromagnetic, weak, and strong interactions. The Large Electron Positron collider (LEP) situated at the European Centre for Particle Physics

(CERN) was designed and built during the 1980s to continue and enhance our understanding of the Standard Model and the deeper issues of the Universe as we understand it.

By any standards the performance of the LEP collider since its startup in 1989 has been spectacular, with luminosities well in excess of its design parameters now regularly being achieved. Four large, general purpose particle detectors are situated at four points on the collider ring. This thesis relates studies conducted using data collected by the ALEPH detector.

Over the last four years, LEP has been operated as a $Z^0$ particle factory. The $Z^0$ is one of the gauge bosons of the electroweak interaction and until the LEP era only a handful of these particles had been detected. Each experiment at LEP has now collected in excess of 2 million $Z^0$ events and hitherto impossible avenues of experimental research have been opened to the particle physicist. The decay of the $Z^0$ into a quark anti-quark pair and the subsequent radiation of a hard gluon from one of the quarks is the subject of this thesis.

The construction of the first $e^+e^-$ colliders took place in the 1950s and they have proven an extremely useful tool for the study of particle physics ever since. A period of particular excitement occured during the mid-1970s when the first evidence for the 2-jet structure of the hadrons emerging from an annihilation event were published [34]. At the same time theoretical advances [28] suggested that the next generation of $e^+e^-$ colliders might see evidence for 3-jet events where one of the jets was postulated to arise from a hard radiated gluon. That events of this nature were subsequently found in data collected at the PEP [22] and PETRA [38] $e^+e^-$ colliders is one of strongest confirmations that quantum chromodynamics (QCD) is a good model of the strong interaction.

Using the large number of 3-jet events now captured by ALEPH, this thesis employs the technique of high transverse momentum lepton tagging, first suggested for this purpose in [47], to identify one or two of the three jets as "quark" jets arising from the decay of the primary quarks. Two analyses have been completed both of which share common experimental techniques.

The first analysis of the 3-jet event data seeks to measure the angular distri-

bution of the quark jets by creating a 2-dimensional (or "Dalitz") plot of their scaled energies. This distribution has then been compared with various Monte Carlo predictions to test QCD and to attempt to exclude other models.

The second analysis looks for and measures any differences between the quark and gluon jets found in 3-jet events. A prime concern of this analysis was to minimise all sources of bias so that any measurable differences could be attributed to the different properties of quark and gluon jets as predicted by QCD.

The structure of the text is as follows:

- **Chapter 2:** The outstanding features of the Standard Model and QCD are described. In addition, some of the problems associated with extracting numerical predictions from perturbative QCD are discussed. Nevertheless, an attempt is made to give the reader some feeling for the expected results from both analyses.

- **Chapter 3:** The physical layout and operation of both the LEP collider and the ALEPH detector are discussed, including the ALEPH dataflow and analysis packages.

- **Chapter 4:** For reasons which will become apparent the careful definition of what is meant by the terms "quark jet" and "gluon jet" is of central importance. This chapter defines these terms from an experimental standpoint and introduces much of the analysis "machinery" used in later chapters.

- **Chapter 5:** As has already been mentioned, the quark jets in the 3-jet events are identified using high transverse momentum lepton tags. The analysis package (LEPTAG) used to select such particles and the tag method employed are described in detail.

- **Chapter 6:** The Dalitz plot analysis and its results are related. In particular a log-likelihood statistical method is described which was employed to compare the real data and Monte Carlo distributions.

- **Chapter 7:** The second analysis chapter describes the search for measurable quark and gluon jet differences and the special method developed to minimise any experimental biases. Each jet variable which was studied is carefully defined and distributions for both real data and Monte Carlo events are presented.

- **Chapter 8:** The results from both analyses are drawn together and concluding remarks are made.

- **Appendix A:** The proof of the log-likelihood statistical test is given.

# Chapter 2

# Quark and Gluon Jets - Theory

## 2.1 Introduction

By the end of the last century many physicists believed that the main scientific challenges had been addressed. The fundamental unit of matter was the atom with its interactions on the microscopic and macroscopic scales being described by Maxwell's electromagnetism and Newton's gravity. Then, as now, the two interactions had resisted all attempts at unification but it was believed that it was only a matter of time before this was achieved.

The discovery of radioactivity by Becquerel and the subsequent discovery of the nucleus by Rutherford revealed the inadequacies of the accepted theories. By the early 1930's the birth of quantum mechanics and relativity had lead to a completely new picture of the structure and function of the Universe at both ends of the distance scale. From these two theories Dirac developed the gauge theory of quantum electrodynamics (QED) which reformulated the interaction of charged particles in terms of a momentum transfer mediated by photons. The principle that fundamental interactions can, and should, be described as an exchange of particles is a central principle of all modern particle physics theories and a central tenet of the Standard Model. In addition to the above, such gauge theories must exhibit gauge invariance and renormalisability. Gauge invariance requires that any predicted values, which are in general magnitudes of quantum wave functions, be unchanged by the addition of arbitrary phases to the wave

functions. Renormalisability is the ability for certain divergent integrals to be collected into one factor and replaced with measured values, so allowing further predictions to be made from the theory.

Shortly after Pauli's hypothesis of the neutrino to explain $\beta$-decay, a model of the weak interaction was proposed by Fermi. One year later Yukawa presented the first rigorous treatment of the strong nuclear binding force. Both of these forces were viewed as short range due to the observation that Rutherford scattering was electromagnetic down to distances of $\sim 10^{-14}$m.

During the 1950s an abundance of hitherto unseen hadrons were detected as the energies attainable experimentally increased relentlessly. In 1964 Gell-Mann suggested that the hadrons comprising this "particle zoo" might all be composed of just three "quarks": the up, down, and strange. In this picture, the baryons were composed of three quarks (or three anti-quarks) and the mesons a quark anti-quark pair. This theory was very successful in explaining the observed hadron spectra but it failed in some notable cases. For instance, the $\Delta^{++}$ was predicted to contain three $u$-quarks in a symmetrical state. However, because quarks are fermions, this violates the Pauli exclusion principle which requires fermions to have anti-symmetric wave functions. The introduction of the "colour" quantum number, with three possible values normally given as red, green, and blue, allowed the quarks in the $\Delta^{++}$ to have an anti-symmetric wave function (rgb) and hence conform to the exclusion principle.

Over the last twenty years the quark model has been enhanced, first with the addition of the charm quark and later with the addition of the top and bottom quarks. This body of knowledge is contained in what is now known as the Standard Model. Tests of this model comprise all of the important present day research in high energy physics.

The information contained in this chapter has come from a variety of sources. Certain references are given explicitly, however several general texts worth mentioning are [2], [5], [33], [53], and [55]. In addition, the excellent "QCD and jets at LEP" [51] was a source of much useful information.

| Generation | Leptons | | Quarks | |
|---|---|---|---|---|
| | Charge = -1 | Charge = 0 | Charge = $+\frac{2}{3}$ | Charge = $-\frac{1}{3}$ |
| 1 | $e^-$ | $\nu_e$ | up (u) | down (d) |
| 2 | $\mu^-$ | $\nu_\mu$ | charm (c) | strange (s) |
| 3 | $\tau^-$ | $\nu_\tau$ | top (t) | bottom (b) |

Table 2.1: The three generations of fermions

## 2.2 The Standard Model

There are two basic types of particle: the integer-spin bosons and the half-integer-spin fermions. The spin 1 (or vector) gauge bosons are the mediators of the basic interactions and consist of the photon of electromagnetism, the gluon of the strong interaction, and the $Z^0$ and $W^\pm$ of the weak interaction. Notice that gravity is not included in this list, and indeed in the Standard Model, as it has so far resisted all attempts to describe it properly using a gauge theory.

The building blocks of all matter are the fermions and these can be divided into two classes: the leptons which interact via the electroweak interaction, and the quarks which also interact strongly. The electroweak interaction is the combination of the weak and electromagnetic forces which are clearly separated at low energies but are combined into a unified force at energy scales at and above that of the $Z^0$ particle. Both leptons and quarks are structureless at present scales of investigation and are therefore considered fundamental. Both have spin 1/2.

The leptons consist of the electron, the muon, the tau, and their corresponding neutrinos. The quarks consist of the up, the down, the strange, the charm, the top, and the bottom. Each of these particles has a corresponding anti-particle which has opposite attributes except for energy and spin. They are summarised in Table 2.1 arranged in doublets according to their coupling to the weak current. The Universe as we know it is constructed from members of the first generation.

Until very recently the top quark was merely predicted by theory. A recent paper [20] from the CDF Collaboration at Fermilab has shown evidence for a top

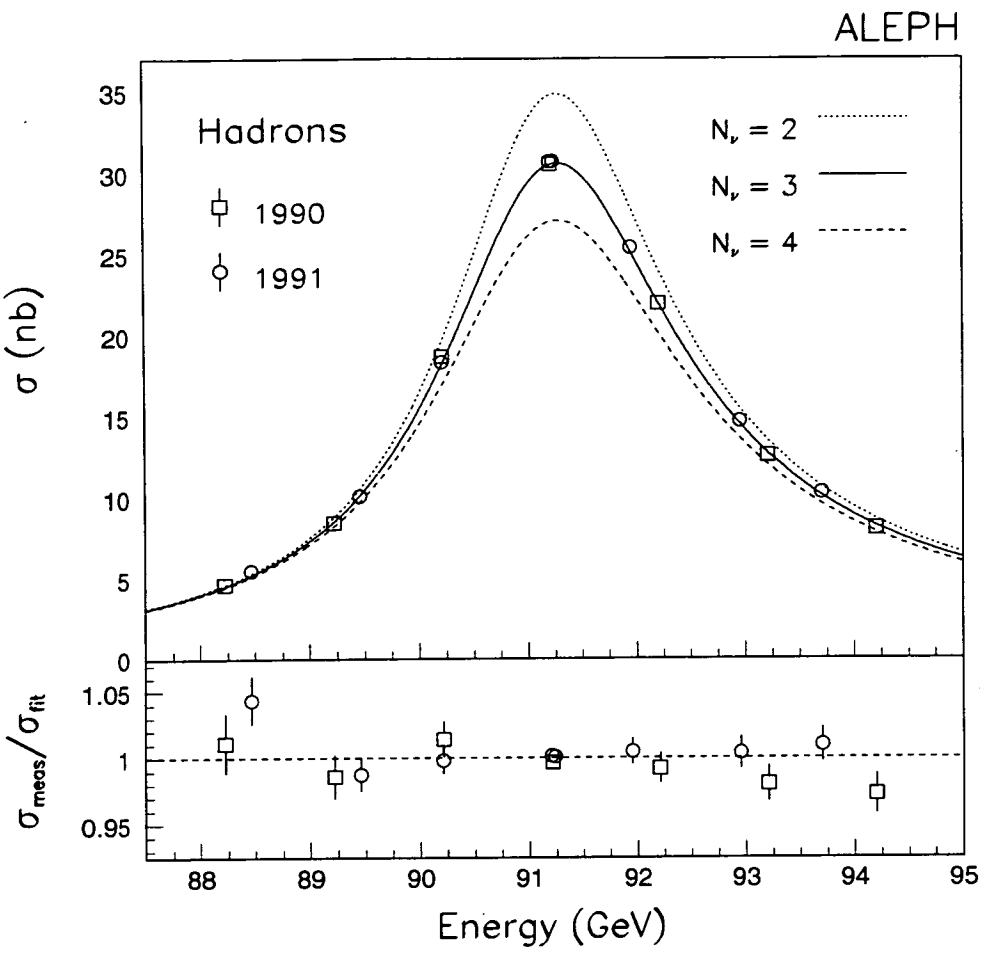


Figure 2.1: The hadronic cross section as a function of $E_{cm}$

quark with a mass of $174 \pm 10^{+13}_{-12}\mathrm{GeV/c^2}$.

That there are only three generations has been shown by the four LEP collaborations in their measurements of the shape of the $Z^0$ resonance. Figure 2.1 shows the ALEPH result for 1990 and 1991 data. The line shape varies according to the number of generations. The upper plot shows the hadronic cross section as a function of centre-of-mass energy. The three solid lines show the expected line shape for two, three and four neutrinos. The lower plot shows the ratio of measured over expected cross section for three neutrinos. At present all known neutrinos are believed to have negligible or zero mass therefore the chance that there is a further generation containing a massless neutrino is small. If there is another generation then the mass of the associated neutrino would have to be

greater than $M_{Z^0}/2$.

So far nothing has been said concerning the Higgs boson. The prediction of this particle, which has not yet been observed, arises from the formal structure of the fields used to construct the Standard Model and it is thought to be very massive. The electroweak part of the Standard Model is constructed from a SU(2)⊗U(1) symmetry group. The SU(3) colour group describes the strong force which is known as the theory of quantum chromodynamics (QCD). For gauge invariance to exist in the model it is found that vector fields must be used to describe the observed bosons. However, for the symmetry to hold, these bosons must also be massless - this is not found to be the case experimentally, for the electroweak interaction in particular. By introducing into the theory a scalar field with non-vanishing vacuum expectation value (the so called "Higgs field"), which couples to the boson and fermion fields, the interaction potential is moved from the origin although the symmetry is still preserved. This behaviour generates the mass terms for the bosons and fermions.

## 2.3 QCD and the Decays of the $Z^0$

The annihilation of $e^+e^-$ particles and the production of a $Z^0$ particle followed by its subsequent decay into a fermion anti-fermion pair is the process which is of interest to physicists at LEP I. The decays of the $Z^0$ studied in this thesis concern the process $e^+e^- \rightarrow Z^0 \rightarrow q\bar{q}$ where $q\bar{q}$ is a quark anti-quark pair whose production is described by electroweak theory. Its subsequent decay into a collection of hadrons is thought to be modelled by QCD.

The strong interaction as described by QCD, occurs between quarks because they possess colour. Colour can take one of three values and is analogous to electromagnetic charge. In further analogy there are colour-magnetic and colour-electric forces which are mediated by the exchange of gluons. Since strong interactions change colour and colour is conserved, the gluons themselves must be coloured. There are therefore eight colour changing bosons required to mediate the exchange of this force, one for each possible transformation from one colour

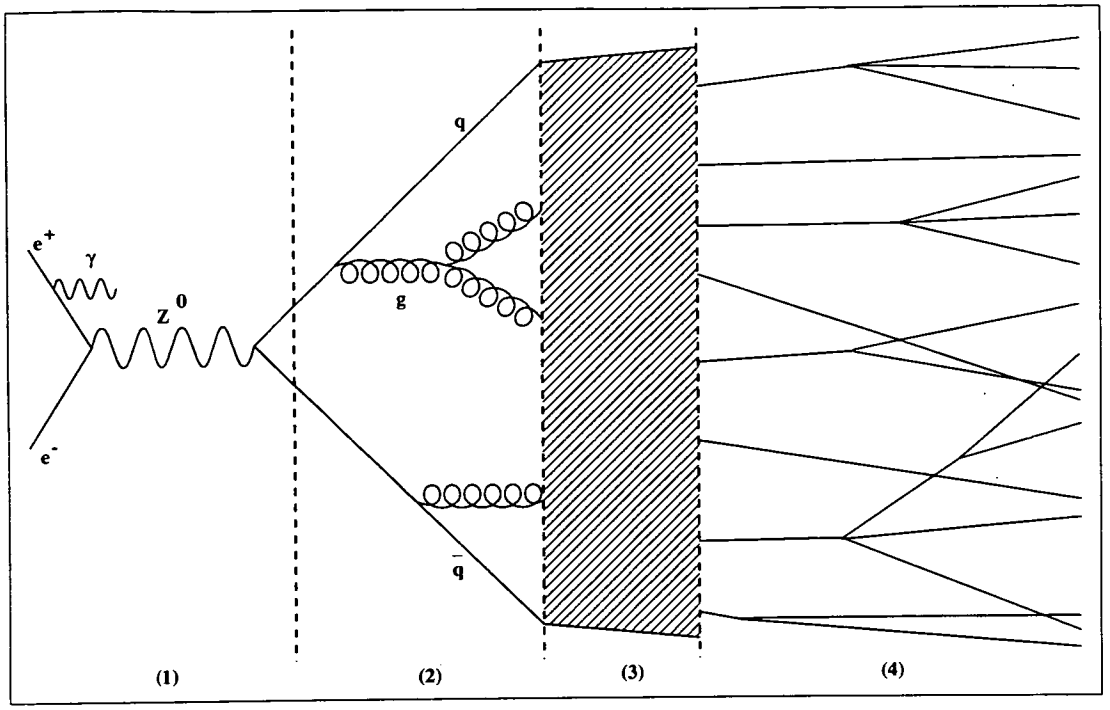


Figure 2.2: The various stages of an $e^+e^- \rightarrow Z^0 \rightarrow q\bar{q} \rightarrow hadrons$ decay

value to another. The fact that gluons possess the attribute which they mediate makes them unique among the gauge bosons. It also leads to self coupling eg. $g \rightarrow gg$ and therefore the gluon gauge field is known as a non-Abelian theory.

Free quarks have never been detected and are not expected to be. Experimentally all physically observed hadrons are colour neutral. It is hypothesised that the interaction potential of the quarks inside a hadron is coulomb like but increases linearly at distances greater than $\sim 10^{-15}$m. This implies that an infinite amount of energy would be required to separate two quarks in a bound state. In the string model, as two quarks are pulled apart, it becomes energetically favourable for $q\bar{q}$ pairs to materialise and form new separate hadrons. It is a process such as this which is believed to create the shower of hadrons observed as a result of $Z^0 \rightarrow q\bar{q}$ decays. This whole process is known as fragmentation.

Figure 2.2 shows the various stages of an $e^+e^- \rightarrow Z^0 \rightarrow q\bar{q} \rightarrow hadrons$ event. The first stage, which is described by electroweak theory, involves the annihilation of an $e^+e^-$ pair (preceded perhaps by initial state bremsstrahlung radiation which reduces the mass of the final state), the creation of a $Z^0$ and its decay into a $q\bar{q}$ pair.

The second stage is described by perturbative QCD. In this stage the initial $q\overline{q}$ pair may radiate hard gluons which in turn may radiate further quarks and gluons. The number of such branchings calculable by perturbative QCD is limited and the reasons for this will be discussed in detail shortly.

The third stage is thought to be given by QCD but because it is not calculable perturbatively it is an area which is described by phenomenological models. It is believed that what occurs is further branchings of $q \rightarrow qg$, $g \rightarrow q\overline{q}$, and $g \rightarrow gg$ until a number of colourless hadrons are produced.

In the final stage, any of the colourless hadrons which are unstable decay and may subsequently be detected experimentally. As will be discussed at length in Chapter 4 the detected particles are generally grouped in clusters of "jets" inside the detector. It is common at LEP to detect not just 2-jet but also 3-jet and 4-jet events. It has to be accepted that the arrangements of these jets correspond approximately to the direction and total energy of the original hard partons. This is known as the principle of "local parton-hadron duality".

Before describing the Monte Carlo modelling of these four stages it will be useful to briefly discuss the limitations of perturbative QCD.

The theory of QCD contains one common coupling parameter $\alpha_s$, which to $1^{st}$ order is given by:

$$\alpha_s(Q^2) = \frac{12\pi}{(33 - 2n_f)\ln(Q^2/\Lambda^2)} \tag{2.1}$$

where $n_f$ is the effective number of quarks ($n_f = 5$ at LEP), $Q^2$ is the momentum transfer scale at which $\alpha_s$ is being calculated (on the $Z^0$ peak $Q^2 = E_{cm} = 91.2\text{GeV}$), and $\Lambda$ is a free dimensional parameter of the theory. At short distances (or alternatively at large momentum transfer scales according to the uncertainty principle) $\alpha_s$ is small and the quarks and gluons behave like free particles. At larger distances $Q^2$ decreases and $\alpha_s$ becomes very large leading to the breakdown of the perturbative method.

The Born process $e^+e^- \rightarrow q\overline{q}$ is modified in $1^{st}$ order QCD by the probability that the $q$ or $\overline{q}$ radiate a gluon. It can conveniently be expressed in terms of the

scaled energy variables of the $q\bar{q}$ pair and is given below [28]:

$$\frac{1}{\sigma_0}\frac{d\sigma}{dx_1 dx_2} = \frac{\alpha_s}{2\pi} C_F \frac{x_1^2 + x_2^2}{(1-x_1)(1-x_2)} \tag{2.2}$$

where $x_1 = \frac{2E_q}{E_{cm}}$, $x_2 = \frac{2E_{\bar{q}}}{E_{cm}}$, $\sigma_0$ is the lowest order cross section, and $C_F$ is a colour factor for the process $q \rightarrow qg$. The expression assumes massless quarks. A more rigorous treatment [37] takes into account the quark masses but the differences at LEP are thought to be small.

Two additional event types are added in $2^{nd}$ order perturbative QCD, namely $Z^0 \rightarrow q\bar{q}q\bar{q}$ and $Z^0 \rightarrow q\bar{q}gg$. These configurations can be thought of as leading to 4-jet events. The formulae which predict the 4-jet rate are lengthy as they have to take into account the many different Feynman diagrams possible due to gluon loops etc. It is the large number of calculations required which has so far prevented a full $3^{rd}$ order calculation from being published.

The 4-jet rate as predicted by $2^{nd}$ order perturbative QCD is much lower than that observed experimentally. However, this may be explained by the fact that the $2^{nd}$ order corrections to the 3-jet rate were found to be large and therefore it is likely that the $3^{rd}$ order corrections to the 4-jet rate may be large also. To attempt to minimise the higher order contributions, optimised perturbation theory has been used where the choice of $Q^2$ scale is varied. Defining $Q'^2 = \mu E_{cm}$ with $\mu < 1$, equates to an increase in $\alpha_s$ which leads to an increase in both the 3-jet and 4-jet rates. However, loop corrections also depend on the $Q^2$ scale and compensate for the changes to the jet rates by large negative contributions (although more of the enhanced 4-jet rate remains). It is also possible to argue on kinematical grounds that a lower $Q^2$ is a sensible scale to work at as most gluon emission occurs with $E_g$ considerably less than $E_{cm}/2$. Values of $\mu$ as low as 0.001 have been used but these values are generally viewed as unphysical.

## 2.4 Matrix Element Monte Carlo

Matrix element Monte Carlos employ the $2^{nd}$ order calculations described above to determine the relative fraction of two, three and four parton final states.

As was explained earlier, the conversion of the final state partons into hadrons cannot be described by perturbative QCD. Instead, the final state partons are converted into colourless partons using one of the hadronisation models described shortly.

Matrix element Monte Carlo performed much better at low energies where the average hadron multiplicity was much closer to the parton multiplicity. Less predictive work was therefore left to the hadronisation model. At LEP the number of final state partons using this method is quite small, compared to the number of hadrons occuring directly after hadronisation, and therefore matrix element based programs have fallen out of favour.

## 2.5 Parton Shower Monte Carlo

Parton shower algorithms are based on an iterative use of the basic branchings $q \rightarrow qg$, $g \rightarrow gg$, and $g \rightarrow q\bar{q}$. Generally a primary 2-, 3-, or 4-parton final state is generated using the $2^{nd}$ order matrix element approach. This configuration is then allowed to "shower" in a tree-like fashion according to the various production probabilities of the branchings given above. An example of this will be shown in Chapter 4. It is a general property of the popular shower algorithms that they produce "coherent" showers. This is achieved by angularly ordering the radiated partons such that the production angle of each parton is never more than the production angle of the radiated parton which preceded it. The showering process continues until the evolution variable (which is generally defined in terms of the energy and/or momentum of each parton) reaches a predefined cut off.

The parton shower approach therefore seeks to model the fragmentation process to a much higher order than the matrix element method and has been used very successfully at LEP.

## 2.6 Hadronisation

Hadronisation is the modelling, using as a starting point the results of matrix element calculations or parton shower algorithms, of the process whereby final state partons are converted into colourless hadrons. These hadrons may subsequently decay and be detected experimentally. No theory of this process exists as the partons involved are assumed to have too low energies for perturbative QCD to be applicable. The two models which have been employed in this analysis are:

### 2.6.1 Cluster hadronisation

This model splits all gluons in the final state into $q\bar{q}$ pairs. The colour of each final state is carefully managed so that colourless quark anti-quark clusters are formed. These clusters are subsequently decayed into the final colourless hadrons.

### 2.6.2 String hadronisation

In this model a "string" connects the final state quarks. Any final state gluons are considered as momentum concentrations or "kinks" in the string. As the quarks in the string diverge in space the potential energy of the string increases until a $q\bar{q}$ pair materialises thereby splitting the string. Hadronisation is complete when there is insufficient energy left in any part of the string to produce new $q\bar{q}$ pairs and the resulting quarks are arranged into colourless hadrons.

## 2.7 Monte Carlo Programs

Two programs have been used in this analysis.

### 2.7.1 JETSET 7.3

By default a $2^{nd}$ order matrix element parton configuration is generated which is subsequently showered. The resulting parton shower is hadronised using string hadronisation. JETSET [53] may also be used, with appropriate tuning, to

generate purely matrix element based events where no shower has taken place. Both these configurations are used in this analysis.

### 2.7.2 HERWIG 5.6

The HERWIG program [45] also generates $2^{nd}$ order matrix element parton configurations which are subsequently showered. The main difference between it and JETSET is that it employs cluster hadronisation.

## 2.8 Quark and Gluon Jet Measurements

### 2.8.1 Philosophical implications

One of the primary aims of this thesis is to show how the quark and gluon jets in 3-jet events may be identified. It is easy to think of two of the three hadron jets in a 3-jet event as being quark jets and one as the gluon jet but the question arises as to whether or not this is a valid picture.

As will be shown, in the detector it is possible to identify two of the three jets as containing a $B$ meson using high transverse momentum ($P_\perp$) lepton tagging. The rationale behind calling the third jet a gluon jet is that the $B$ mesons are assumed to have been formed from ancestors of the primary $b$-quarks created from the decay of the $Z^0$. The probability of a gluon decaying into a $b\bar{b}$ pair is low.

Relating hadron jets to hard perturbative partons generated using matrix element Monte Carlo is conceptually straight forward. The method adopted might be to pair the hadron jets and partons according to their kinematics. Of course this assumes that the jet creation resolution parameter is defined such that the number of hadron jets equals the number of hard partons. This will obviously not always be the case and it is not clear how to deal with this experimentally.

The picture is even more confused if a parton shower model is considered. Here, perhaps ten partons may be found at the end of the shower before hadronisation. Perturbative QCD gives no clue as to which partons should be considered

as arising from a hard gluon or quark. It is therefore very difficult for any precise theoretical predictions about the differing properties of quark and gluon jets to be made.

The solution adopted, which is described in detail in Chapter 4, was to carefully define experimentally what was meant by the terms "gluon jet" and "quark jet" and to measure and compare their properties.

Obviously it was important to assess the purity of the lepton tag method and a carefully defined parton level procedure was evolved. This method essentially clustered the partons into three jets and, using mother to daughter Monte Carlo relationships, found which two of the three jets contained the direct ancestors of the primary quarks. The created jets were not used to predict any quark or gluon properties because of the conceptual difficulties outlined above.

The measurements which were undertaken can easily be split into two categories:

### 2.8.2 The 3-jet Dalitz plot

Equation 2.2 gives to first order the angular distribution of the primary quarks in 3-jet events. Because the expression is only to first order and diverges as $x_1,\ x_2 \rightarrow 1$, trying to compare its prediction with that of the measured two-dimensional $x_1$ versus $x_2$ distribution would obviously not have been a good test of QCD. Instead, the Dalitz plot study compared the measured distribution with that of the fully reconstructed[1] Monte Carlo prediction.

In addition to this, a study was made of various other Monte Carlo models in order to measure the effects of different predictions. One model was of particular interest. In this model [53] the spin 1 gluon was replaced by a spin 0 scalar gluon. The three jet cross section therefore takes the form:

$$\frac{d\sigma}{dx_1 dx_2} \propto \frac{x_3^2}{(1-x_1)(1-x_2)} \tag{2.3}$$

[1]The term "fully reconstructed" means that the final state hadrons were passed through the ALEPH detector simulation program (GALEPH).

where $x_1$ and $x_2$ are defined as before and $x_3 = \frac{2E_q}{E_{cm}}$. The predicted Dalitz plot distribution for this model is radically different to the QCD distribution. Chapter 6 describes the methods used and the results of this study.

### 2.8.3 Quark and gluon jet differences

The difficulties involved with the theoretical definition of quark and gluon jets become apparent when the literature is searched for numerical predictions of detectable differences between them. While it is documented in the literature that such differences should exist (see for instance [51][Page 40]) there is a dearth of numerical predictions for the actual magnitude of such differences. This is in part a result of the difficulty in defining theoretically what the terms "quark" or "gluon" or "jet" mean and also the complexity of the calculations involved.

A gluon has a larger colour charge than a quark. In perturbative QCD this is reflected in a higher probability for a gluon to radiate. Since the gluon has a colour factor associated with it of $C_A = 3$ and the quark a colour factor of $C_F = \frac{4}{3}$, naively, as in [42], one might expect the ratio of gluon jet to quark jet multiplicity to be $C_A/C_F = \frac{9}{4}$. Why this is not the correct prediction was explained in a talk given to the ALEPH QCD group by Dr B. Webber, and in much greater detail in [14], as follows:

$N_i(Q_0, Q_1)$ is defined as the mean number of particles resolved at a scale $Q_0 = Q\sqrt{y_0}$, inside a jet resolved at a scale of $Q_1 = Q\sqrt{y_1}$, where $i$ denotes the type of jet ($i = g$ or $i = q$) and $Q^2$ is the centre-of-mass energy of the event. The resolution parameter $y$ is known as the $y_{cut}$ in jet clustering algorithms and will be discussed in detail in Chapter 4. It can be shown that:

$$N_i(Q_0, Q_1) \sim 1 + C_i N(\alpha_s, \ln(y_1/y_0)) \tag{2.4}$$

where $C_i$ is the colour factor for gluons ($C_g = C_A = 3$) and quarks ($C_q = C_F = \frac{4}{3}$). $Q_0$ is obviously fixed as there must be a finite number of single particles in

the event. As $Q_1 \to \infty$ then

$$\frac{N_g}{N_q} \to \frac{C_A}{C_F} = \frac{9}{4} \tag{2.5}$$

However, at the $Z^0$ peak the resolution parameter $y_1$ used to select 3-jet events is considerably less than 1 (typically $y_1 = 0.01$). The behaviour of $N_g/N_q$ is therefore far from asymptotic and estimates suggest it should be closer to 1 than 2. Measuring this quantity is therefore of great interest.

There is strong theoretical support for the idea that a gluon jet ought to be broader and have a softer overall particle momentum spectrum than a quark jet. This is discussed in [27] and [50]. The effects are thought to arise simply because gluons have a larger colour factor than quarks and are therefore expected to radiate further gluons and quarks more readily.

In order to study these differences the gluon and quark jets must have roughly the same energies. The mean gluon jet energy in 3-jet events is considerably less than that of the quark jets. In the past gluon jets of a particular energy have been compared with quark jets selected from 2-jet events recorded at a lower experimental centre-of-mass energy. At LEP this is not possible and therefore for this analysis a symmetric event topology was defined to select quark and gluon jets of similar energy (see Chapter 7).

A suitable variable to study the distribution of longitudinal energy within quark and gluon jets is rapidity. This is measured for each particle with respect to the jet axis and is defined as:

$$\eta = \frac{1}{2} \ln \left( \frac{E + P_{\parallel}}{E - P_{\parallel}} \right) \tag{2.6}$$

where $E$ is the particle energy and $P_{\parallel}$ is its longitudinal momentum with respect to the jet axis. If the constituent particles of quark jets do indeed exhibit a harder and narrower momentum distribution than gluon jets then they should contain, on average, more particles with high values of rapidity. The softer and wider gluon jets by contrast should have lower average values of rapidity and a narrower distribution. Figure 2.3 shows the expected rapidity distributions for

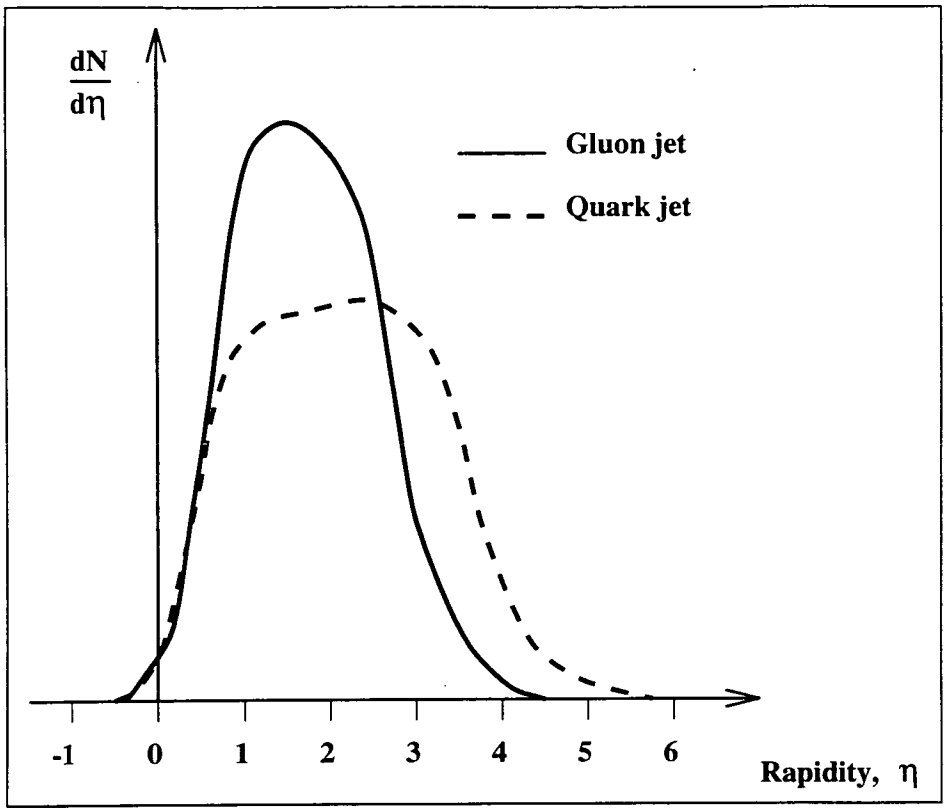


Figure 2.3: Expectation of the rapidity distribution for quark and gluon jets

quark and gluon jets based on Monte Carlo studies by Dr B. Webber.

In addition to the multiplicity and rapidity measurements, several other distributions were studied. These included:

- The fragmentation variable $X_E = \frac{E_{particle}}{E_{jet}}$.
- The transverse momentum ($P_{\perp jet}$) of the particles in the jet with respect to the jet axis.
- The jet profiles, measured using the number of particles in succesive cones centered around the jet axis and the amount of energy contained in each cone.

In all of these cases, which will be properly defined in Chapter 7, the aim was to discover if the prediction that quark jets were harder and narrower, and gluon jets softer and wider, was true. Through trying to quantify these differences it was hoped to provide new information to aid more accurate theoretical, and Monte Carlo predictions of quark and gluon jet properties to be made.

Before describing the analysis methods used to define the quark and gluon jets, the next chapter describes the ALEPH experiment and LEP.

# Chapter 3

# The ALEPH detector

## 3.1 Introduction

The LEP $e^+e^-$ storage ring was constructed by the members of the CERN laboratory in the second half of the 1980s. The collider has a circumference of approximately 26.7Km and is situated in an underground, nearly circular tunnel, which runs from the outskirts of Geneva to the foothills of the Jura mountains. For geological reasons the accelerator is inclined by 1.42% to the horizontal. Large experiments are situated at four points on its circumference, the ALEPH experiment being one of these. The first $e^+e^-$ collisions were observed by the experiments in September 1989. In the ring, counter circulating bunches of electrons and positrons are accumulated, accelerated, and brought into collision at the four experimental interaction points.

ALEPH is situated at the Echenevex interaction point (IP4), 143m below the foothills of the Jura mountains. It is designed to measure the events created by the $e^+e^-$ collisions first at the energy of the $Z^0$ (LEP I) and later at, or slightly above, the $W^+W^-$ pair production threshold (LEP II). The event rate at the $Z^0$ is quite low ($\sim$ 1Hz) and is expected to be two or more orders of magnitude smaller at LEP II. For this reason a fundamental design principle was to collect as much information per event as was reasonably practicable. To facilitate this, ALEPH was designed as a series of concentric cylinders (the beam pipe passing centrally along their axis) covering as much of the solid angle as was possible.

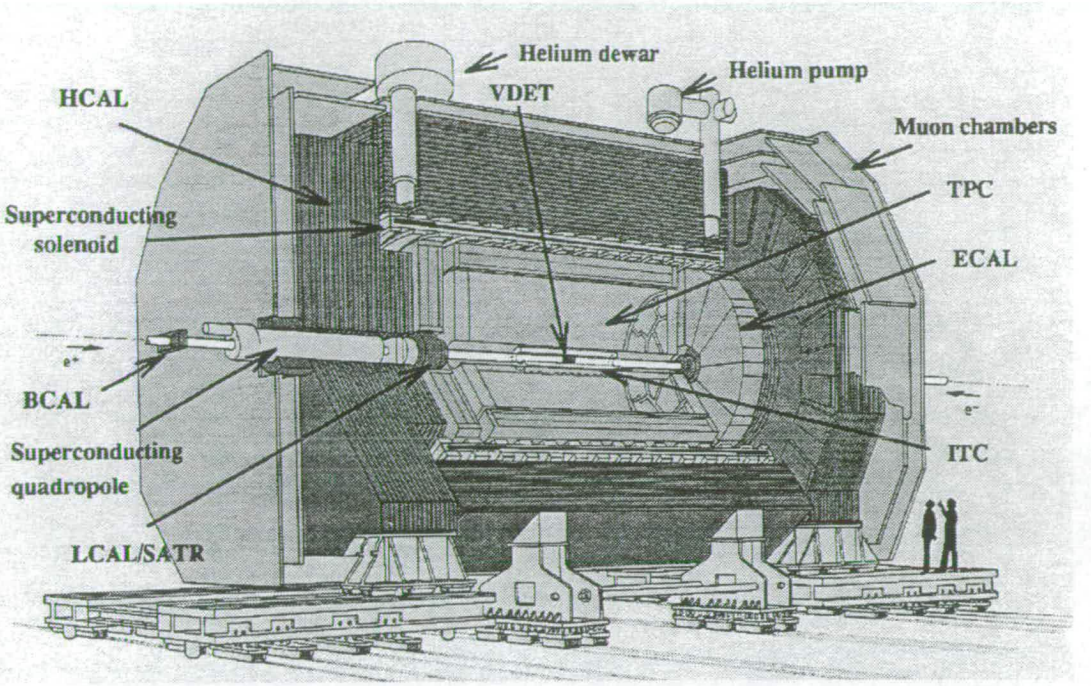


Figure 3.1: Cut away perspective view of the ALEPH detector

Rather than explicitly cite all the sources of information used in this chapter, for brevity they are cited here [3], [10], [11], [12], [16], [29], [30], [31], [35], [46], and [49]. Figure 3.1 shows a cut-away view of ALEPH. The detector is split into several sub-detectors each of which is labeled. The purpose and operating principles of each sub-detector will be described shortly. However, it may be instructive at this point to review the general principles behind single particle detection in high energy physics experiments.

## 3.2 Single Particle Detection Methods

In order to detect a single particle travelling through a medium we rely on it giving some or all of its energy to that medium. In any material there are continuous thermal excitation transitions taking place, therefore any useful signal must be created by the particle causing a transition in the material which is highly unlikely to be caused by thermal excitation. This effectively places a threshold of detection on any particle. In order to understand how virtually all particle detectors work it is necessary to be familiar with how a charged particle interacts with matter. The detection of neutral particles is generally performed

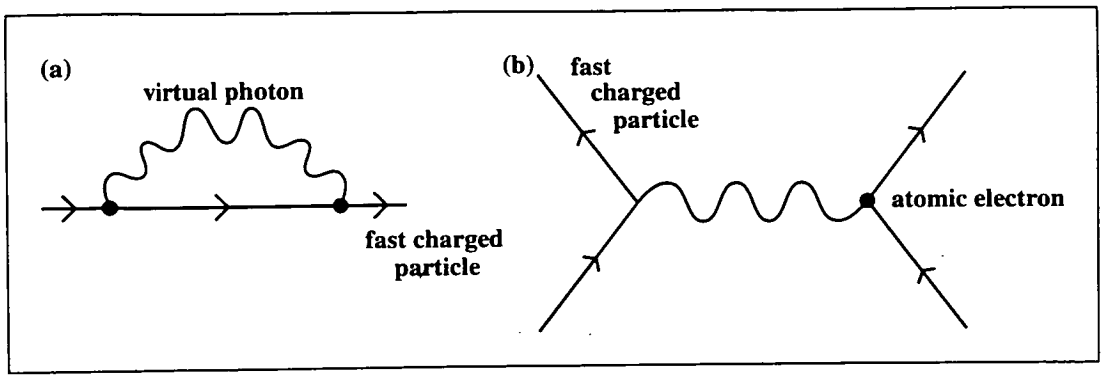


Figure 3.2: Feynman diagrams for (a) creation/destruction of a virtual photon and (b) interaction with an atomic electron

by requiring that they first create a charged particle of some description which may be subsequently detected.

Describing the classical coulomb force in terms of the exchange of quanta (photons) requires that the classical $\frac{1}{r}$ dependence of the force appears only when the energy of the emitted photon tends to zero. This energy is too small to base a detection method on and therefore the properties of "virtual" photons, as allowed by the Heisenberg Uncertainty Principle, must be relied upon. A photon may be emitted from a particle without conserving energy or momentum so long as it obeys the relations:

$$\Delta p \Delta x \leq \frac{\hbar}{2} \qquad \text{and} \qquad \Delta E \Delta t \leq \frac{\hbar}{2} \tag{3.1}$$

Figure 3.2a shows the Feynman loop diagram associated with the creation and destruction of a virtual photon. Virtual photons with high energy will therefore only propagate a very short distance from the charged particle. In general it is permissible to visualise a charged particle as the "bare" charge surrounded by a cloud of virtual photons which are capable of interacting with an atomic electron as shown in Figure 3.2b.

There are six possible photon interactions with matter [1].

**1. Coherent elastic scattering:** atoms not excited therefore not of use in par-

[1]Cherenkov radiation and transition radiation are not included in this list as they both arise from the bulk properties of matter. They are not used at any stage of ALEPH particle detection.

ticle detection.

2. **Photoexcitation:** photon absorbed by atom exciting it to a higher quantum state.

3. **Photoelectric effect:** total energy of photon is absorbed by an atomic electron giving the electron enough energy to leave atom (ionise it). The expelled electron has the photon energy minus its atomic binding energy.

4. **Compton scattering:** photon is scattered by an atomic electron which carries off some of the photon's energy. The electron may well have enough energy to leave its atom.

5. **Photon conversion:** at high enough energies it is possible for a photon to create an $e^+e^-$ pair. The threshold energy required is slightly more than double the electron mass as the process needs to occur close to a nucleus in order to conserve momentum.

6. **Photonuclear absorption:** high energy photons may excite nuclear states which subsequently decay with emission of a neutron, proton or another photon.

Charged and neutral hadrons may also interact strongly. Given sufficient amounts of dense matter the probability that an inelastic nuclear collision will occur is large. Such collisions lead to nuclear disintegrations of the target nucleus, the products of which may ionise or induce further nuclear reactions. A so called "hadronic shower" develops.

The high energy particles produced in an annihilation event may be grouped according to the way they interact with matter as follows:

- **Photons:** At energies sufficiently above twice the rest mass of the electron ($\sim$ 0.5MeV) photon interaction is dominated by photon conversion. The resulting $e^+e^-$ pair will lose energy by bremsstrahlung (the radiation of a photon). Given sufficient energy the radiated photon is likely to again produce an $e^+e^-$ pair. In this way, so called "electromagnetic showers"

develop. The radiated photons will eventually have insufficient energy for photon conversion and Compton scattering then dominates.

- **Electrons and positrons:** High energy electrons and positrons lose energy predominately through bremsstrahlung. Again, they produce electromagnetic showers which progress in exactly the same way as described for the photon.

- **Charged hadrons:** These particles have a lower rate of bremsstrahlung than electrons (because their $e/m$ ratio is much smaller) and if their energy is high (as in ALEPH), their rate of energy loss via ionisation is slow. They are therefore highly penetrating and substantial amounts of matter are required before an inelastic nuclear collision takes place as described above. The hadronic showers produced are much larger than electromagnetic showers due to the highly penetrating nature of the remnants of the nuclear collision.

- **Neutral hadrons:** As these particles carry no charge they do not ionise or lose energy through bremsstrahlung. Their only mode of interaction is via inelastic scattering. The resulting shower is indistinguishable from that of a charged hadron.

- **Muons:** Muons are unique in that they lose energy via bremsstrahlung slowly due to their high mass, and their high energy at ALEPH means energy loss via ionisation is also slow. As they are leptons they do not interact strongly (inelastic nuclear scattering will not occur) and therefore they travel an extremely long range in matter (they can traverse the entirety of ALEPH and escape). It is this characteristic which is used to identify them.

### 3.2.1 $dE/dx$

Charged particles, moving moderately relativistically, lose energy as they pass through matter via ionisation. A semi-classical treatment results in the Bethe-

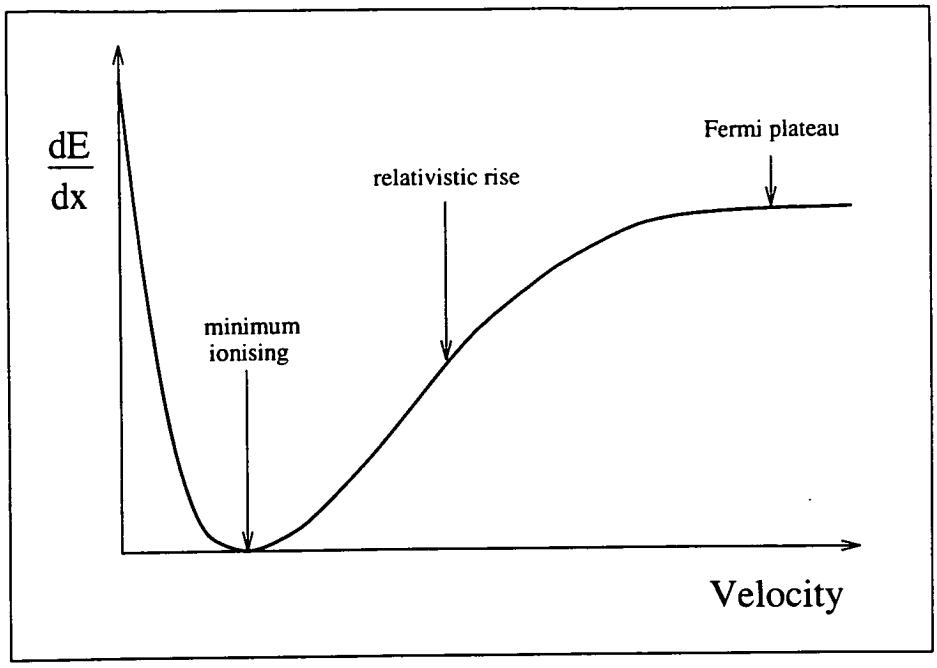


Figure 3.3: The variation of energy loss $\frac{dE}{dx}$ as a function of velocity for a fast particle passing through an ionising medium

Bloch formula:

$$-\frac{dE}{dx} = 4\pi N_A r_e^2 m_e c^2 z^2 \frac{Z}{A}\frac{1}{\beta^2}\left[\ln\left(\frac{2m_e c^2\gamma^2\beta^2}{I}\right) - \beta^2 - \frac{\delta}{2}\right]. \qquad (3.2)$$

Here a particle of charge $ze$ is assumed to be passing through matter with atomic number $Z$ and atomic weight $A$. $N_A$ is Avogadro's number, $m_e$ and $r_e$ are the mass and classical radius of the electron, $\beta = \frac{v}{c}$, and $\gamma = (1-\beta^2)^{-\frac{1}{2}}$. $I$ is the ionisation constant for the medium and $\delta$ is a correction factor related to its density. Any ionising particle will have a variation of $dE/dx$ with velocity as shown in Figure 3.3. As the velocity a particle attains for a given energy is proportional to its mass, lighter particles (eg. pions) will enter their relativistic rise well before heavier particles (eg. protons). By measuring a particle's $dE/dx$ it is possible to distinguish its type. An example of the $dE/dx$ response of kaons, pions, protons and electrons is shown in Figure 5.2 where $dE/dx$ measurements with ALEPH are described in more detail.

## 3.3 ALEPH Detection Methods

Many methods have been devised over the years to take advantage of the interactions with matter described above. For brevity only those methods used directly by ALEPH will be described.

### 3.3.1 Scintillation detectors

The passage of a fast charged particle through a medium excites some of the atoms in that medium to higher atomic energy states via the processes described previously. Scintillation detectors rely on counting the number of photons emitted as the excited atoms return to their ground state. Detection of the emitted photons is usually performed by photomultiplier tubes. These tubes produce an electrical signal on detection of a photon by converting the photon to an electron (via the photoelectric effect) and then causing a cascade of electrons within the tube (via a succession of dynodes with increasing positive voltage). The electron cascade is detected by an anode and suitable amplification electronics at the end of the tube. Only one subdetector, the BCAL, relies on the scintillation technique in ALEPH.

### 3.3.2 Gas filled wire chambers

Gas filled counters detect the ionisation left behind in the wake of a fast charged particle. The ionisation is created very close to the path of the fast particle through the gas and it is therefore necessary to attract the charge to an electrode so that a signal may be registered. This is accomplished by applying an electric field. As the charged particles are attracted to their respective electrodes they accelerate, but collide with other gas molecules and are slowed. They therefore have a constant drift time which some chambers use to make precise positional calculations (assuming the drift start time is available). Wires running through the centre of the chamber are generally used as the anode so that, due to the high charge/mass ratio of the electron (and hence high mobility), they will drift towards a wire. As they near a wire ($\sim$50$\mu$m assuming a $\sim$20$\mu$m wire) the electric

field gets very strong causing the ionisation of further electrons. The positive ions will not have moved significantly in this time and all these factors collude to enable the detection of an electronic signal.

Such chambers can be operated in two modes. In the first, the anode to cathode potential is held at a value such that the energy of the incident fast charged particle is proportional to the amount of ionisation detected at the anode. In the second mode the potential is held very high so that an avalanche of electrons occurs. This avalanche will not be proportional to the amount of ionisation. In either mode the ionisation will appear on the wire at a localised point. Timing the different arrival times of the semi-digital signal at either end may be used to discern this position. The TPC, ITC, ECAL and LCAL sub-detectors use the first approach. The HCAL, MUON, and SATR sub-detectors the second.

### 3.3.3 Silicon detectors

Nowadays all high energy physics detectors are read out via computer. One of the spin-offs from this industry has been the ability to produce very pure single crystals of silicon of appreciable size. Layers of silicon of different type ($n$ or $p$) may be grown one on top of the other. Complex arrangements of "tracks" of $pn$ material may be created. As a fast charged particle passes through the depletion layer of a $pn$ junction, so electron-hole pairs are created in the depletion layer. The electrons and holes are attracted to their respective sides and thus a current flows across the junction. Without further amplification these signals may be detected and processed "on-wafer" before being read out. The VDET and SiCAL sub-detectors use this technique.

## 3.4 ALEPH

A description of each major component of the ALEPH detector system follows. In addition to descriptions of the main detector components, the online data acquisition system, the reconstruction system, and the offline analysis programs are also discussed. The quality of the software for these latter steps being of at

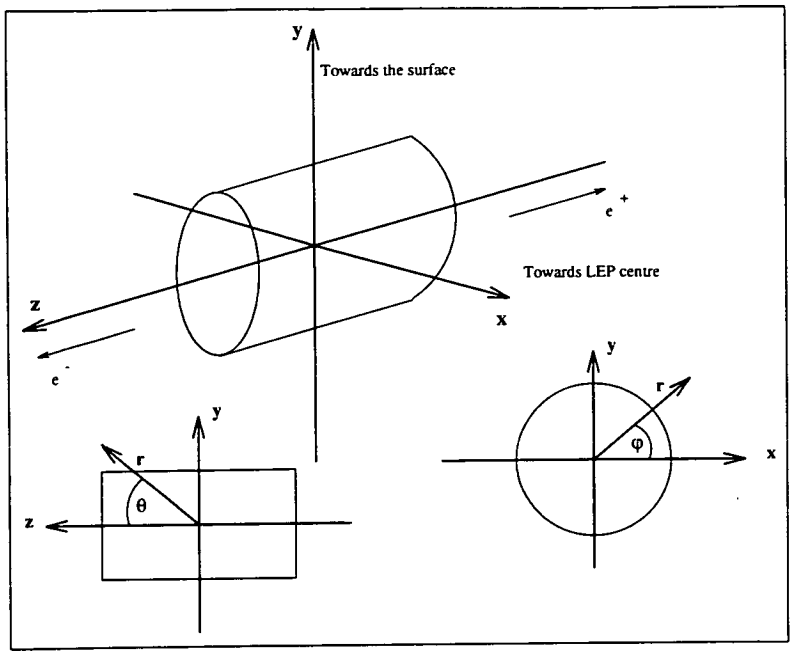


Figure 3.4: The ALEPH coordinate system

least equal importance to the detector hardware.

### 3.4.1 The ALEPH coordinate system

Figure 3.4 shows the ALEPH coordinate system. The $x$ coordinate points to the geometrical centre of LEP from the ALEPH interaction point. The $y$ coordinate points upward and the $z$ coordinate points along the beam pipe. It is positive in the direction of travel of the $e^-$ beam.

### 3.4.2 The vertex detector

The silicon microvertex detector (VDET) is the detector closest to the interaction point at the heart of ALEPH. Installed and commissioned at the start of the 1991 run it provides tracking information for charged particles very close to the interaction point and covers approximately 74% of the solid angle. It consists of two concentric barrels of double sided silicon microstrip detectors (faces). Nine faces comprise the inner layer which is positioned approximately 6.3cm from the beam axis while 15 faces comprise the outer layer positioned approximately 10.7cm from the beam axis. The faces are arranged in such a way as to ensure

that no gap in the angular coverage between both ends of the detector exists.

Each face consists of two independent modules. Each module consists of two double sided silicon microstrip wafers. One side of each wafer is used to measure the $r-\phi$ coordinate whilst the $z$ coordinate is measured using the other side. The total number of analogue channels is ~74000 and these are read out via custom designed VLSI chips, the most important of these being the CAMEX64A chip which provides signal amplification, noise filtering, parallel storage and serial read out. The output from the CAMEX64A appears as a sequence of 256 analog voltages which are routed to several SIROCCO IV modules. These modules digitise the analogue CAMEX64A signals and perform online cluster finding.

Performance of the detector has been very impressive although some damage (repaired at the end of each year's run) has been caused to the silicon wafers by beam loss accidents. Detector efficiency is as high as 93% (including damaged areas which account for 5% of the total area at any one time) the single hit resolution has been found to be 12$\mu$m in $r-\phi$ and 13$\mu$m in $z$.

### 3.4.3 The inner tracking chamber

The inner tracking chamber (ITC) is a cylindrical multiwire drift chamber which provides eight accurate $r-\phi$ points per track in the radial region between 160 and 260mm. It also provides the only tracking for the Level 1 trigger (see later). The wires run parallel to the beam axis and the active length of the chamber is 2m. The beam pipe passes through the centre of the cylinder and the VDET sits inside. The chamber is permeated by the magnetic field and is filled with either a Ar (50%) $C_2H_6$ (50%) or a Ar (80%) $CO_2$ (20%) gas mixture at atmospheric pressure.

Figure 3.5 shows a representation of the drift cell. The relative sizes of the various wires are shown (but not their actual sizes). The hexagonal drift cell consists of a central 30$\mu$m sense wire surrounded by six 147$\mu$m field wires. There are also three 100$\mu$m guard wire layers around which are wired hoops of aluminium wire to catch any wires which might break, and limit damage to a small section of chamber. The small diameter of the sense wires is required for high

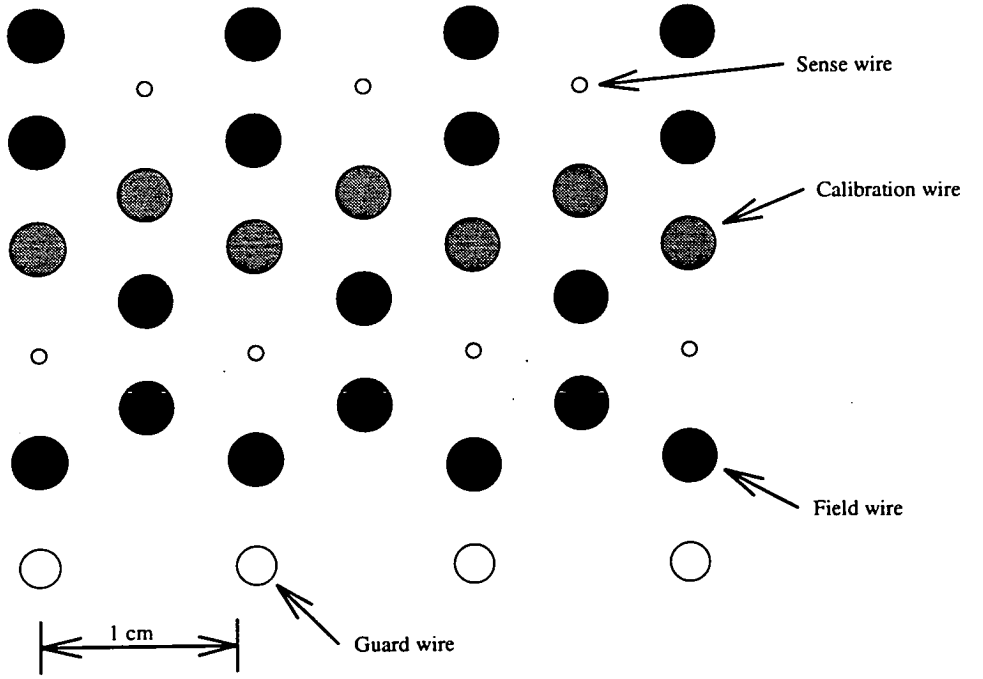


Figure 3.5: The ITC hexagonal drift cell

gas amplification of the ionisation close to the wire. The field wires are held at 0V during operation whilst the sense wires are held at ~+2.4kV. The 960 sense wires are strung in 8 concentric layers (96 wires in the four inner layers and 144 in the outer four). There are 960 calibration wires, 2880 ordinary field wires and 336 guard wires. During normal operation the calibration wires are held at the same voltage as the field wires. They are used to calibrate the $z$ coordinate measurement which is calculated by measuring the difference in time it takes a pulse registered by a sense wire to propagate to the end of the wire. During calibration both ends of the wire are pulsed simultaneously which induces a hit at $z = 0$ on the sense wire. The time expansion boards are calibrated to reproduce this measurement correctly.

The signals from the sense wires are passed to the central boards (known as AZ boards) which amplify and discriminate the signals. The discriminator outputs are fed to CAMAC time-to-digital converters (TDCs) where the drift time for each hit is calculated. In addition to discrimination the AZ boards also perform the time expansion calculation to find the $z$ position of the hit. The digital signals from one end of the chamber are used to switch on the charging of

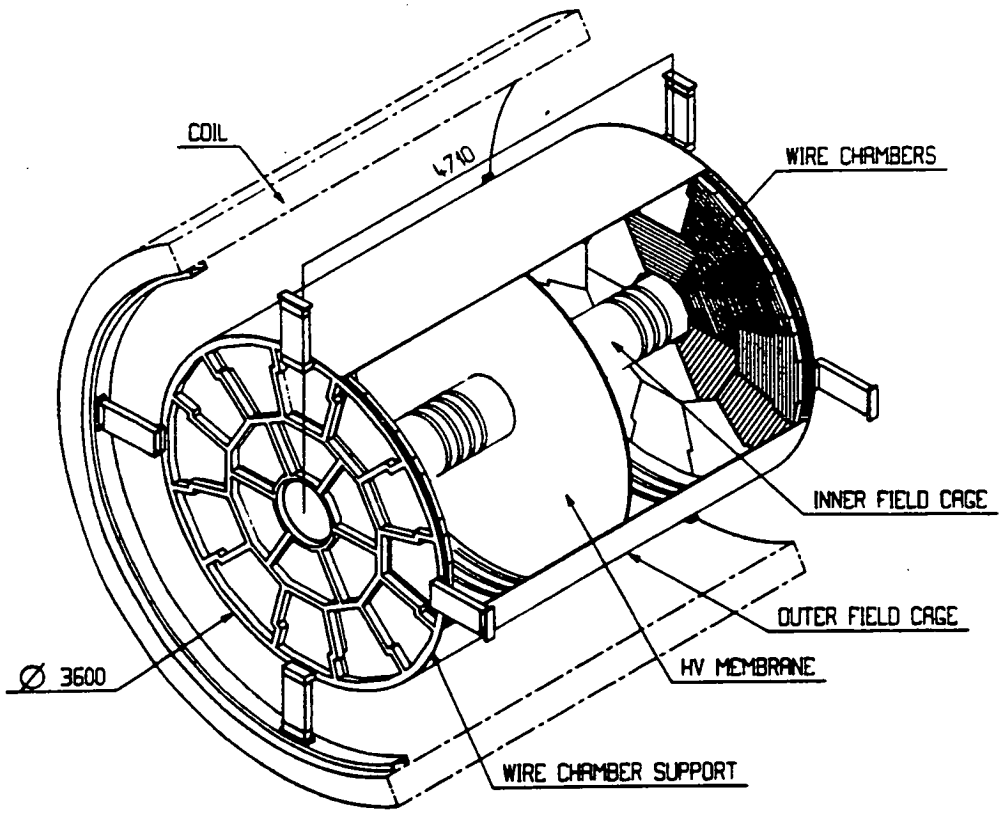


Figure 3.6: An overall view of the TPC

a capacitor and the signals from the other end (delayed 50ns) are used to switch off the charging. The time taken for the capacitor to discharge is proportional to the $z$ position of the pulse on the wire.

Initially Level 1 trigger information was found using the $r-\phi$ radial hit patterns and a lookup table of "acceptable tracks". This has now been improved with the implementation of a "space point processor" which also takes into account the $z$ position of the hit when looking for valid tracks. The Level 1 output in either case is available within $3\mu$s.

On receipt of a Level 2 "yes" trigger signal (see later) the detector is read out and the accurate $r-\phi$ TDCs are allowed to complete their conversion. Typical ITC read out time is 1.7ms. The detector resolution is $\sim 100\mu$m in $r-\phi$ and 3cm in $z$.

### 3.4.4 The time projection chamber

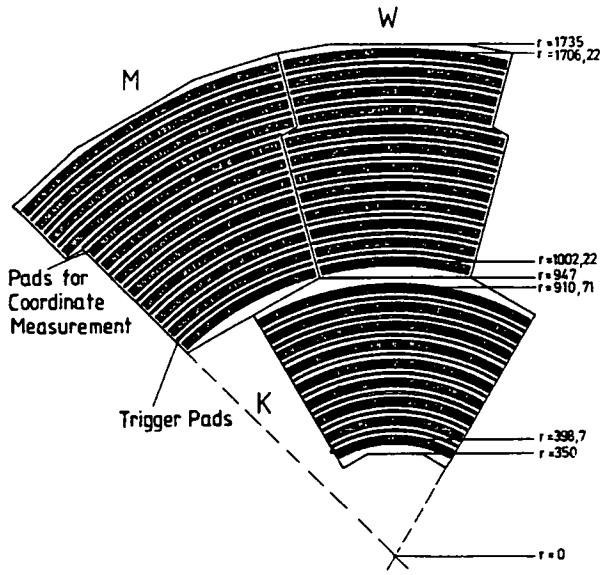


Figure 3.7: A detailed view of the TPC end sectors

Figure 3.6 shows the time projection chamber (TPC) which is a very large three dimensional imaging drift chamber. It is cylindrical about the ITC, has an inner radius of 31cm, an outer radius of 180cm, and is 4.7m long. The volume of the chamber is filled with a 9:1 mixture of Ar and $CH_4$. The 1.5T axial magnetic field provided by the superconducting magnet permeates the whole chamber (as it does the ITC and VDET) thus giving the ability to measure the momentum of charged particles. A central membrane, held at a voltage of -27kV, divides the chamber into two halves. The wire chambers at either end are at ground which implies a field gradient of $\sim$115Vcm$^{-1}$. In order to ensure a constant axial electric field, etched onto the inner and outer field cages are concentric electrodes held at compensating voltages.

A charged particle passing through the TPC will ionise the gas and leave behind a trail of electrons. These will then start drifting (with a well known constant velocity) to an end plate. Each end plate consists of 18 wire chambers (sectors) and Figure 3.7 shows a detailed view of one of the inner, and two outer, sectors. There are 6 inner sectors and twelve outer sectors on each end plate and each of these is covered with etched copper cathode pads. Two types of pad exist. The most abundant is the $r-\phi$ pad with an area of 6.2x30mm$^2$. The TPC has 41004 of these in total. As drift electrons approach the wire

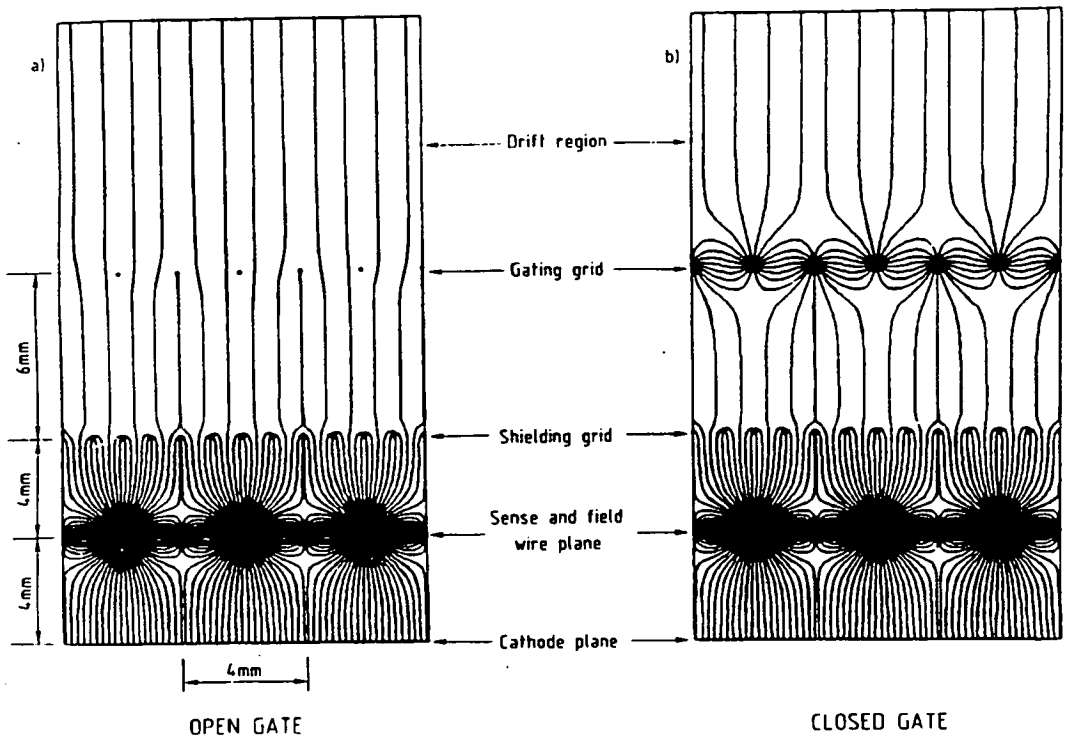


Figure 3.8: TPC gating grid showing electric field lines: (a) gate open, (b) gate closed

chamber they initially pass through the "gating" wire grid and then the cathode wire grid (see Figure 3.8). They then rapidly accelerate towards the sense wires causing an avalanche to occur. Since the process is proportional to the number of drift electrons the sense wires may be read out and the intensity of ionisation calculated providing the TPC with impressive $\frac{dE}{dx}$ capabilities. At the same time a signal is induced on the $r-\phi$ pads and the second type of pad, the "trigger" pad. The trigger pads are much larger than the $r-\phi$ pads (6.3mm in $r$ and $15^o$ in $\phi$). There are 32 trigger pads per sector and these are read out to form the Level 2 trigger.

The TPC gating wire grid is of particular importance to the operation of the detector. Figure 3.8 shows the electric field lines close to the wire chambers when the gating grid is off (a) and on (b). Without this grid, positive ions, created during the electron avalanche near the sense wires, would build up in the drift region and cause track distortions. In the open state the gate is held at the same potential as the cathode (shielding) grid. In the closed state alternate wires are held at a potential of $\Delta V_{gate} = \pm 150V$ thus making an opaque gate

both to incoming electrons and outgoing positive ions (which tend to follow a zig-zag path towards a gating grid cathode where they are neutralised). Switching between open and closed is done synchronously with the beam crossing signal. Immediately on receipt of a Level 1 "no" the gate is closed again. If the Level 1 result is a "yes" the gate remains open for the maximum 45$\mu$s drift time of electrons in the TPC.

Read out is performed via 660 time projection digitisers (TPDs) which amplify and convert to digital form the signals from the pads and wires. The TPDs are supervised and read out by 36 time projection processors (TPPs), one for each sector. Two event builders, one for either end plate, read out the TPPs before being read out themselves by a further event builder.

Calibration of the system to provide information on the distortion of particle tracks and to accurately measure the drift velocity of the chamber is performed regularly with the aid of two ultraviolet lasers. A number of straight tracks are ionised in the TPC by splitting the beams created by these lasers. The measured curvature of these tracks is used to apply corrections to those of real particles. It has been found that there are enough impurities in the TPC gas to produce ionisation from the ultraviolet light without the need for any special additives.

The performance of the TPC varies with track orientation with the $r-\phi$ resolution lying between 160 to 400$\mu$m and the $z$ spatial resolution lying between 0.7 to 2.3mm. The momentum resolution is given by $\Delta p/p^2 \simeq 1.5 \times 10^{-3}(\mathrm{GeV/c})^{-1}$.

### 3.4.5 The electromagnetic calorimeter

The electromagnetic calorimeter (ECAL) is arranged as a barrel surrounding the TPC closed by two end caps. Figure 3.9 shows an overall view and how the barrel and end caps are subdivided into modules which cover $3.9\pi$ of the solid angle in total. Each of these modules is a lead/wire-chamber sampling device of 22 radiation lengths designed explicitly to measure the position and energy of electromagnetic showers. Figure 3.10 shows the mechanical construction of a barrel module (left hand diagram) and an end cap "petal" module (right hand diagram).

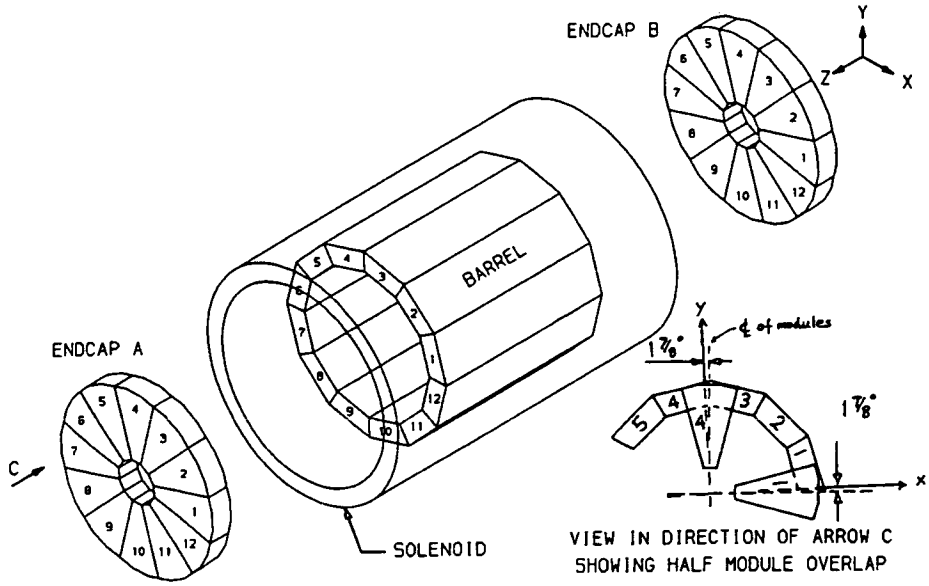


Figure 3.9: Overall view of the ECAL

Each module is a sandwich of 45 lead and proportional wire-chamber layers. A typical layer is shown in Figure 3.11. The total energy and the position of a shower is measured using small ($30 \times 30\text{mm}^2$) cathode pads connected into towers pointing towards the interaction point. Each tower is read out in three sections ("storeys") corresponding to 4, 9, and 9 radiation lengths from the interaction point outwards. Ionisation from an electromagnetic shower developed in the lead sheets is amplified in avalanches around the $25\mu$m gold plated tungsten wires. The signals, which are proportional to the amount of ionisation, are read out capacitively from the cathode pads.

The 12 barrel modules each have 4096 towers and 12288 channels (147456 for the entire barrel). Since the geometry is projective not all of these channels are fully equiped. The tungsten wires lie along the $z$ axis, parallel to the magnetic field. Each wire plane has approximately 200 wires. The width of the pad rows is the same in $\phi$ but increases from the centre outwards in $\theta$ in order to have the transverse width of the towers match the shower size.

The design criteria of the end cap petals were the same as for the barrel modules. Cathode pad sizes are given by the tower structure of the calorimeter. There is a maximum of 50 pad rows in $\theta$ in any layer of the petal. Each pad row is divided into equal $\phi$ segments across the full 30° angle of the petal.

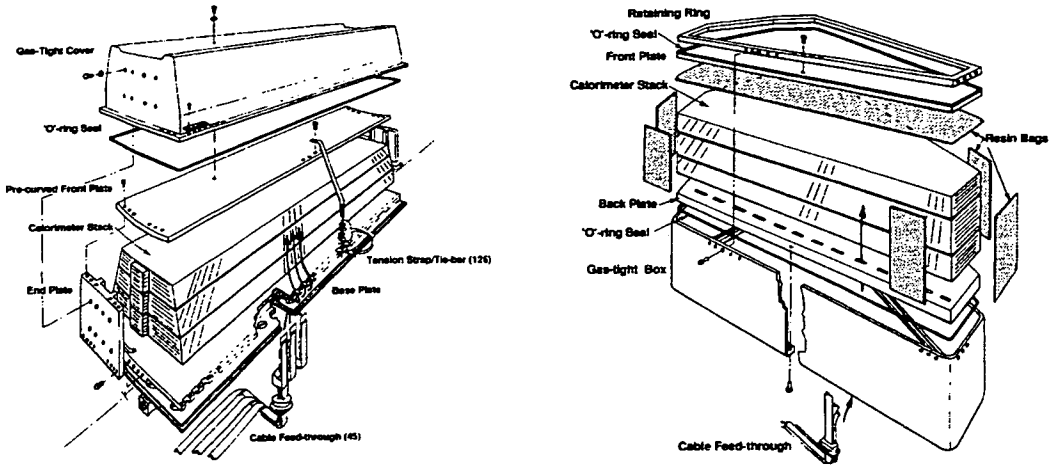


Figure 3.10: Mechanical construction of a barrel module (left) and end cap petal (right)

The main characteristic of the ECAL read out is its size: 221184 pads and 1620 wires. The low number of wire channels is because all the wires on a single layer are read out together on a single channel. In order to reduce the number of communication wires coming from the detector the read out is heavily multiplexed. After analogue to digital conversion, the data are read out by read out controllers (ROCs). The ROCs clean and format the data before they are themselves read out by the ECAL event builder which formats the data before passing it to the main ALEPH event builder. The energy resolution $\Delta E/E$ is $18\%/\sqrt{E}$.

### 3.4.6 The magnet

The magnet consists of a superconducting solenoid producing a homogeneous magnet field of 1.5T parallel to the beam axis with a useful magnetic volume of $123\text{m}^3$. The uniformity of the field is very high (demanded for accurate operation of the TPC) and the main field component has been found to be reproducibly uniform to the level of 0.2%. The hadron calorimeter serves as an iron yoke.

The solenoid consists of a main winding of diameter 5.3m and length 6.35m with 1532 turns (representing approximately 25km of wire) and two compensating coils situated at either end of diameter 5.45m and length ~40cm. The wire

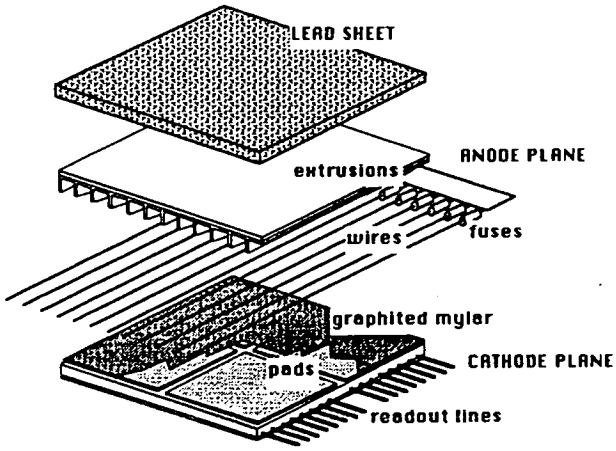


Figure 3.11: A typical ECAL layer

used is niobium-titanium (NiTb) alloy operated at 4.2K where it is superconducting. At the normal operating field of 1.5T the current in the coil amounts to 5000A and 136MJ of energy is stored. Liquid helium is used to cool the solenoid which is insulated by two jackets, one kept at 70K, the other at 4.2K.

### 3.4.7 The hadron calorimeter and muon chambers

The hadron calorimeter (HCAL) performs four important functions for the ALEPH experiment. Firstly it provides the main support structure for the detector and secondly it acts as the return yoke (it is predominately made of iron) for the magnet. In addition to this the large total thickness of the iron (1.2m) acts as an effective absorber of all energetic hadrons produced at the interaction point. Finally, by calorimeterising the layers of iron via the interspersion of "streamer tubes", useful hadronic shower information is provided. The only detectable particles capable of passing through the HCAL are muons. Two extra layers of double streamer tubes separated from each other and positioned on the outside of the HCAL form the muon chambers which provide positional and angular information for muon candidates. Figure 3.12 shows the HCAL barrel and muon chambers. Two end caps, with attached muon chambers, complete the detector.

The barrel consists of twelve modules each axially split into two parts which are mirror images of each other. Each module has 22 iron slabs of 5cm thickness plus an outer slab of 10cm. 23 layers of plastic streamer tubes equiped with pad

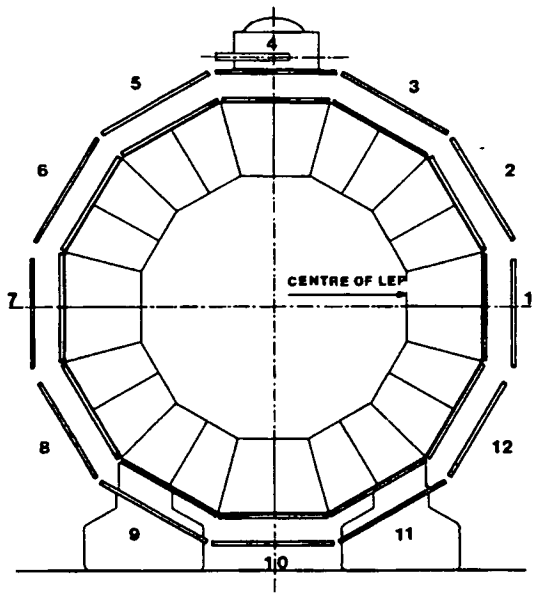


Figure 3.12: The HCAL barrel and accompanying MUON chambers

and strip read out are interspersed between the iron slabs. As in the ECAL, the pads are arranged in projective towers which are, however, of much greater size ($3.7^o \times 3.7^o$). In general the pattern of towers covered by one tower in HCAL corresponds to 14 towers in ECAL. The strips are arranged parallel to the wires (one per cell) and are used to derive a digital two dimensional picture of any detected hadronic shower. This is vital to the process of identifying muons. The end caps consist of 6 petals and are of similar construction (other than shape) to the barrel modules. The barrel and end caps contain 3456 and 2868 towers respectively, and of these, 768 are shared through overlap.

Streamer tubes are constructed in a similar way to proportional wire chambers but they operate in a higher sense wire voltage regime where the avalanche ionisation is not proportional to the amount of primary ionisation created by the incoming particle. The data from each module is read not from the wires but from the summed pads which comprise a tower (via FASTBUS units) and digitally from the strips by the ALEPH strip read out scanner (ASTROS) units. Hadron calorimeter processors (HCPs) control and read out these units before passing the data to the event builder. Figure 3.13 shows hit patterns recorded during a test-beam run for (a) a 10GeV pion, (b) a muon, and (c) an electron.

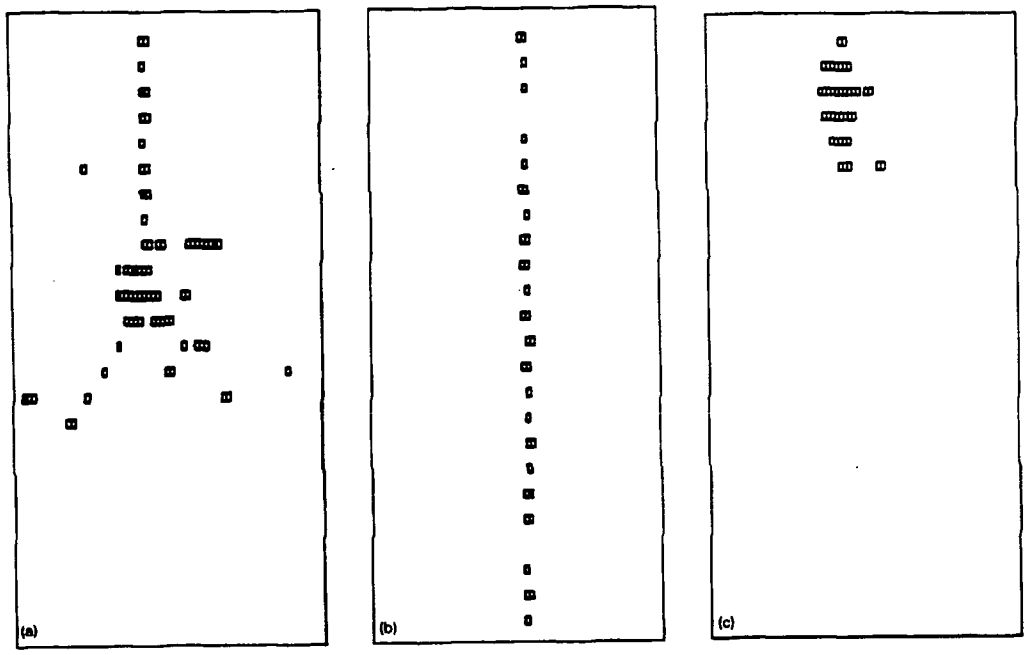


Figure 3.13: Typical hit patterns detected in the HCAL for (a) a 10GeV pion, (b) a muon, and (c) an electron

The muon chambers use the same streamer tubes arranged in two double planes separated by several centimetres. Only the digital strip read out is used and as the tubes in both planes of each chamber are arranged orthogonally and their position in space is known, a three dimensional hit coordinate for each chamber is available.

### 3.4.8 The luminosity detectors

As has already been described in Chapter 2, probably the most significant result published by the LEP experiments to date is their determination of the number of families of matter. The ALEPH value for combined data taking periods from 1989 to 1992 being $N_\nu = 2.980 \pm 0.035$. In order to precisely determine this value (and others) an accurate determination of the "luminosity" delivered to the experiment over time is required.

Luminosity is simply a measure of the rate at which opportunities for a reaction to occur are created. It is process independent. By definition the luminosity ($\mathcal{L}$), the cross section for process $x$ ($\sigma_x$), and the reaction rate for the process

$(R_x)$ are related by

$$\mathcal{L}\sigma_x = R_x \tag{3.3}$$

In ALEPH the luminosity measurement is determined from the rate of Bhabha events ($e^+e^- \rightarrow e^+e^-$) at small scattering angles. In this low angle region the interference between the $\gamma$ and $Z^0$ is at a minimum (Bhabha events dominate) and the cross section is well known in QED to third order. To first order the cross section is

$$\frac{d\sigma}{d\Omega} = \frac{4\alpha^2}{E_e^2}\frac{(\hbar c)^2}{\theta^4} \tag{3.4}$$

where $E_e$ is the electron energy. The inclusion of high quality luminometers close to the beam pipe was therefore of high importance to the ALEPH design.

Three small sub-detectors provided the luminosity information until late 1992 when a fourth sub-detector was installed. Until late 1992 two sub-detectors provided the measurements of electron/positron energy and position - the luminosity calorimeter (LCAL) and the small angle tracker (SATR [2]). In addition a small Bhabha calorimeter (BCAL) was installed on the beam pipe some distance from the experiment on either side. The BCAL operates at very low angles and provides fast relative luminosity measurements in the control room during data taking. At a luminosity of $10^{31}\text{cm}^{-2}\text{s}^{-1}$ the LCAL sees a luminosity of 0.3Hz. This is increased at the BCAL, due to the low angle, by around 20 times providing an immediate, though low accuracy, luminosity measurement.

Figure 3.14 shows half of the LCAL and SATR. The LCAL being the larger of the two cylinders. The two sub-detectors are split into two halves which are located at $z \simeq \pm 2.7$m from the interaction point.

The SATR consists of 36 half planes of drift tube chambers operated non-proportionately. Each half plane consists of four 45° sections each of which contains 14 drift tubes. The tracker accepts electrons/positrons with polar angles between 40 and 90mrad. There are 1152 read out channels each equipped with a TDC. The angular resolution of the whole chamber is ~0.08mrad with an

[2]The SATR has now been replaced by the small angle monitor of background (SAMBA). This was designed to be more robust than SATR and to sit in front of the SiCAL measuring the LEP machine background as accurately as possible.

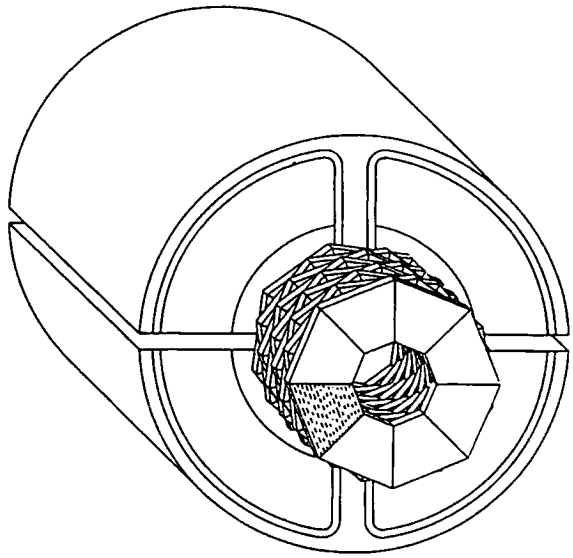

Figure 3.14: The half of the LCAL and SATR - the LCAL is the larger cylinder

efficiency of 99%.

The LCAL is a lead/wire-chamber very similar in construction to the ECAL. The total energy and position of the electromagnetic showers are measured using small $30 \times 30\text{mm}^2$ cathode pads. Each half has 38 sampling layers. There are 4608 read out channels which are multiplexed into the read out ADCs. The energy resolution is $0.014E + 0.20\sqrt{E}$ (GeV) and the positional resolution is 1.4mm in both the $x$ and $y$ directions. The angular acceptance of the LCAL lies between 45 and 155mrad.

The four scintillation counters which make up the BCAL lie $\pm$7.8m from the interaction point. The four monitors are located on either side of the beam pipe in the $x-z$ plane, two on either side of ALEPH. Each of the four counters consists of sheets of tungsten converter interspersed by layers of plastic scintillators. In addition to signals read from the scintillators, one layer of 160 silicon strips is also read out. The aim of BCAL is to provide minute by minute luminosity information to both the shift crew and the LEP control room. Its data has no further physics use.

In addition to the three devices already discussed a fourth luminometer, the silicon calorimeter (SiCAL), was installed in September 1992 (after commission-

ing during the summer). It is a silicon-tungsten sampling device which consists of two homogeneous cylinders surrounding the beam pipe at $z \simeq \pm 2.5$m (ie. in front of the LCAL). The twelve layers of tungsten, alternated by layers of silicon pad detectors, cover the angular range 25 to 58mrad. Every layer is segmented into 16 cylindrical pad rows in radius, each of which is further segmented into 32 sectors giving a total of 12288 pads, all of which may be read out. Successive layers are rotated by 3.75° to avoid the problem of aligned cracks. The energy and positional information provided by SiCAL is of much higher accuracy than LCAL.

### 3.4.9 The ALEPH trigger

Because of the low event rate at LEP the ALEPH trigger was designed to accept all $e^+e^-$ interactions. No specific event type selection is performed and the main purpose of the trigger is to reduce the background to a manageable level. An important quantity when discussing the efficiency of a trigger is the "dead-time". This is the percentage of data taking time, immediately after a beam crossing, where the experiment is not ready to accept new data because it has not recovered from processing a previous event (in ALEPH the TPC read out time defines the dead-time). One of the goals of trigger design is to minimise dead time and hence decrease the probability that a real event, as opposed to a background event, will be missed.

The trigger system is based on three levels of refinement known (unsurprisingly) as the Level 1, Level 2, and Level 3 triggers. For the purposes of the trigger the detector is split up into segments of projective geometry as shown in Figure 3.15. Four detector components play a major role in the logic of the trigger: the HCAL, the ECAL, the ITC, and the TPC. In addition, the LCAL (now SiCAL) is used to trigger on Bhabha candidates. The salient points of the three trigger levels are given below.

**Level 1:** This trigger delivers a decision within $\sim 5\mu$s of a beam crossing (the time between beam crossings is $\sim 23\mu$s). Its has two main purposes. Firstly if the Level 1 result is "No" then it must quickly close the TPC gating grid.

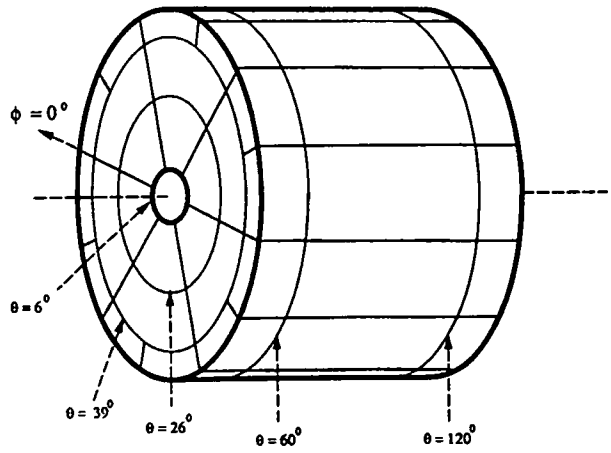


Figure 3.15: The projective geometry of the trigger

Secondly, if the result is a "Yes" it must provide track information, using the ITC, for the Level 2 trigger. The sub-detectors involved in making the Level 1 decision are the ITC, the HCAL, the ECAL and the LCAL.

**Level 2:** This trigger uses the TPC trigger pads and is based on hard wired processors searching for tracks in the $r-z$ plane which are pointed to by those segments already flagged as containing a track by the ITC. The $r-z$ plane is used so as to be independent of the magnetic field (ie. straight tracks ). The time constraints on the trigger are governed by the TPC drift time and ECAL clearing time which is $\sim 61\mu$s in total. If the Level 2 trigger rejects a Level 1 trigger the experiment has to be ready to accept the third bunch crossing after the first trigger (ie. $67\mu$s later). On receipt of a Level 2 "Yes" the whole detector is read out.

**Level 3:** The Level 3 trigger is applied to the event data after it has been read out but before it is recorded. Primitive event reconstruction is performed in an array of dedicated computers attached to one of the data acquisition VAXes. The Level 3 trigger is used to re-apply, more accurately, criteria applied "roughly" at the prior two trigger levels.

The beam conditions at LEP I have been of considerably lower background than might have been the case. The Level 1 and Level 2 triggers have therefore performed well within their design specifications.

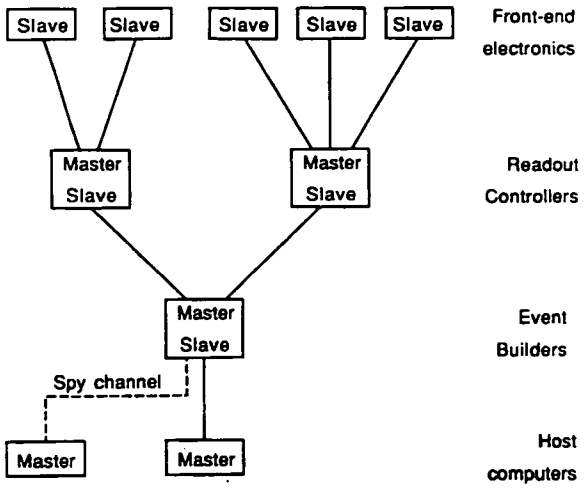


Figure 3.16: The ALEPH read out architecture

## 3.5 The Data Acquisition System

The basic ALEPH read out architecture is shown in Figure 3.16. Adopting a tree-like structure, with no communication between components at the same read level, allowed two important features to be implemented. Firstly, multiple parallel data streams are established, optimising the processing and buffering. Secondly, an extra processing element may be added or skipped without disrupting the data flow. The data acquisition (DAQ) data flow is as follows:

- Timing, trigger, and main trigger supervisor signals synchronise and inform read out controllers (ROCs) about the availability of data. They also keep track of the state of all controllers and ensure the proper protocol is followed.
- The ROCs initialise the front end modules, read them out and format the data into standard banks.
- The sub-detector event builders (EBs) build the information from the ROCs into sub-events for each sub-detector.
- The main EB (MEB) collects all the pieces of an event, ensures the pieces all belong together and that they are all present.
- The Level 3 trigger reduces the event size and may even discard it.

- The online VAX (AL0VOL) collects the data for each event and stores it on disk. The spy VAX (AL0VSD) utilises a secondary read out channel connected to the MEB to provide event and detector monitoring whilst not affecting the main event acquisition provided by AL0VOL.

Figure 3.17 shows an overview of the ALEPH read out[3]. This has changed over time and will continue evolving. Having written a run to disk, the disk is passed to the quasi-online reconstruction VAX cluster known as FALCON (the **F**acility for **AL**EPH re**CON**struction). This consists of approximately 12 VAX computers each running the VMS operating system and the ALEPH reconstruction program JULIA (see later). The data is split into small subsets each of which is farmed out to one of the VAXes exploiting the coarse grained parallelism inherent in the event structure of the data. The reconstructed events are written separately to disk and then reassembled into a reconstructed run when processing of all of the subsets is complete. The reconstructed output of a run is available for offline analysis within 24 hours of data acquisition.

The whole data acquisition system underground is based around FASTBUS and the 680x0 family of microprocessors. Connection to the surface (where the control room and all VAXes are situated) is via a custom designed fibre optic link which connects the VAX online cluster (2 main VAXes and a cluster of $\sim$20 VAX workstations) to the detector. Control of the detector is via the "Zebedee" slow control program which is used to control the high voltage. It enables the whole detector to be switched on and off by clicking on a mouse button. DAQ control is via the run controller which implements the read out as a finite state machine[4]. At any one time a DAQ component is either in a pre-defined state or in a defined transition between two of these states. During run preparation the run controller is used to take all of the DAQ components from state to state thus ensuring all of the read out is initialised correctly and that it is ready to take data when the trigger is enabled.

[3]This figure will change considerably in 1994 due to the introduction of the new VME based slow control and read out system.

[4]Having completed $>$ 20 shifts as third man in 1991 and $>$ 30 shifts as shift leader in 1992 the author has had first hand experience of controlling the detector using these tools

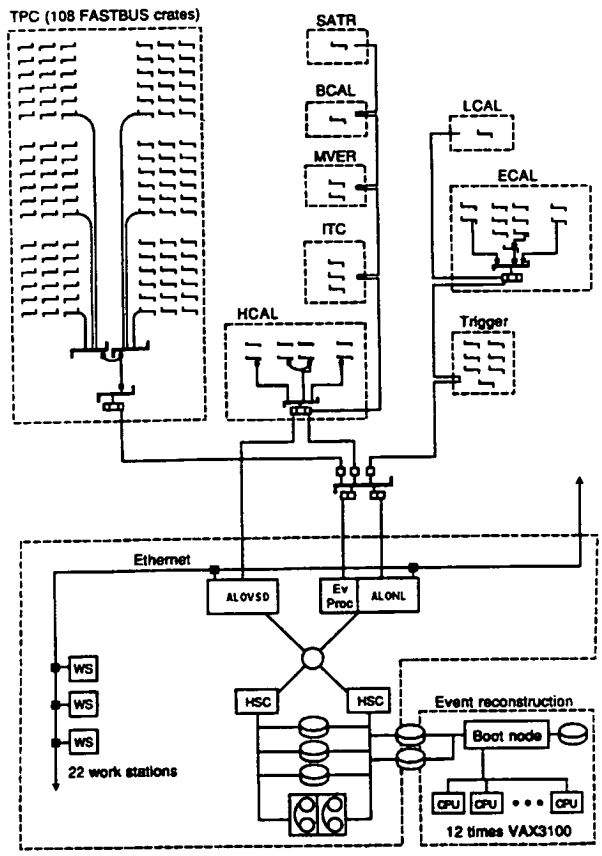


Figure 3.17: An overview of the ALEPH read out

Shift crews are non-expert and only number two volunteers. To aid the shift crews various tools have been developed. The two most useful of these being the DAQ expert system and the online monitoring of histograms system. DEXPERT is programmed to respond to common error conditions in the finite state machine making the job of the DAQ operator (the shift leader) much more enjoyable. Operator intervention is only required when novel or repetitious problems arise. The histogram monitoring is also very useful. A database keeps track of over 3000 online histograms produced by the detector monitoring tasks. A subset of 200 histograms is compared against reference histograms provided by the sub-detector groups. Histograms which fail comparison against their reference by some predefined limits are displayed immediately to the shift crew and computerised help pages are also generally available in response to the error mesages. This system works well and is much appreciated by the shift crews. At all times sub-detector experts are available by telephone.

### 3.5.1 Reconstruction and offline analysis

Any large experiment produces copious amounts of software. ALEPH is no exception. Space precludes a full description of each program; however, the main software components are listed below.

**JULIA:** This is the ALEPH event reconstruction program which runs on the FALCON cluster and may also be run elsewhere when processing Monte Carlo data. The program reads RAW data files (straight from ALEPH) and outputs files in POT (**P**roduction-**O**utput-**T**ape) format. Its functions are to find tracks in the data, to calculate the $dE/dx$ value associated with these tracks, to find vertexes (pairs of oppositely charged tracks not originating from the interaction point), to cluster energy deposited in the calorimeters into "objects", to perform an elementary energy flow analysis (see later), to identify particles such as muons, electrons, and photons (or at least provide estimators for them), and also to perform an accurate luminosity calculation for each run.

**KINGAL:** To understand and test proposed particle theories one of the most useful methods is to generate Monte Carlo data sets. This program is the first step in that process. KINGAL is a jacket program which provides access to a large number of pre-existing Monte Carlo event generators. The two used in this analysis being HVFL03 (based on JETSET 7.3) and HRWG07 (based on HERWIG 5.6). The output produced by KINGAL is designed to be fed straight into GALEPH.

**GALEPH:** This is the detector simulation program which follows the initial state particles generated by KINGAL through the detector elements and attempts to model the electronic response to them as would be expected from the detector. The passage of particles through matter is modelled by the CERN GEANT program which GALEPH uses extensively. GALEPH also calls the TPCSIM program which provides an accurate model of the TPC and its responses - a non-trivial task. Of all of the stages required to produce fully reconstructed Monte Carlo events it is this step which takes

an enormous amount of CPU time and precludes the production of large event samples. The amount of CPU required per $Z^0$ in CERN units (which are based on 1 CPU second on an IBM 370/168) is for KINGAL trivial, for JULIA 35seconds, and for GALEPH 290seconds. A modern DEC AXP workstation is rated at approximately 19 CERN units which gives an idea of the processing time required.

**DALI:** It is often very useful to be able to display on the screen of a workstation a graphical representation of an event. The name DALI is an acronym of **D**isplay of **AL**EPH **I**nteractions. The program has evolved over time[5] into a multiple platform (VMS and UNIX) X Windows implementation. Several different projections of an event may be displayed concurrently. Examples are the $xy$, $yz$, $r-\phi$, 3-dimensional, and $\phi-\theta$ projections. Extensive "zooming", "stretching", and "picking" facilities are available as are many easy ways to apply cuts to the displayed data. There is even a "physics processor" which enables the user to do kinematic calculations on the displayed event and provide hypotheses for the type of a displayed track.

Printing facilities allow the user to create PostScript files of their displayed events. A large amount of online help is also available. DALI has been used to generate all of the event Figures in this text and is regularly in use as a publicity tool for ALEPH.

[5] **Author's note:** During the first year of my studies it was suggested that I could make a useful contribution to ALEPH by converting DALI from the VAX UIS graphical environment to the industry standard X11 Window System (which I already had experience in). At this time DALI consisted of ~100000 lines of Fortran code. Luckily, all of the VMS and UIS specific calls were grouped in just three source files (corresponding to ~10000 lines of code). Two of these files were completely rewritten in the C language using X11 graphics calls in place of the UIS equivalent. The third source file, which was mainly concerned with VMS QIO handling, was modified to remove the VMS dependence. One of the major challenges of the conversion was that the UIS event methodology was different to that of X11. UIS relied heavily on the VMS Asynchronous System Trap (AST) mechanism to respond to mouse movement etc. Since X11 is non-reentrant in places, the AST calls were completely replaced with X11 event handling routines. At the point where DALI used to wait for keyboard input, an event dispatch loop now waits to service the event handlers. Towards the end of my first year a working, reasonably complete version of "X" DALI was passed to its main authors and maintainers Hans Drevermann and Björn Nilsson.

| Data type | Description | Size per $Z^0$ | |
|---|---|---|---|
| RAW | Pre-reconstruction data set | 501K | 100% |
| POT | Production output tape from JULIA | 223K | 44% |
| DST | Data summary tape - same as POT but background/noise events removed | 95K | 19% |
| miniDST | Stores selection of data most useful for Physics analysis | 9.8K | 2.0% |
| nanoDST | Very reduced format, small information content | 1.1K | 0.2% |

Table 3.1: Various ALEPH data formats and relative sizes

**BOS77:** As most of the ALEPH software is written in Fortran 77 (apart from the online code which is written predominately in "C") a simple method for structuring the data of an event was required. In the early days of high energy physics, common blocks were set aside for all the pieces of data which *might* exist in an event. This was very wasteful and therefore memory management packages were produced which operated on a pre-declared large array and tabulated the event information into banks (all of this being required because Fortran 77 cannot dynamically allocate memory). BOS77 is such a system and is used throughout the experiment. An example of BOS bank definition is given in Chapter 5.5. Running parallel with the use of BOS was the first use of the "entity-relationship" model for structuring data. This proved very useful in planning and avoiding coding mistakes. These ideas are now being expanded upon for the next generation of experiments.

Having been reconstructed, the data and Monte Carlo events are made available to the collaboration on a number of computer platforms and either on disk or tape. As such a large amount of data is produced by ALEPH there are various data formats which are given in Table 3.1. The vast majority of this analysis was based on miniDST data sets.

**ALPHA:** Analysis of the data sets by standard Fortran 77 would have been tedious and continually involved reinventing the wheel. An analysis framework program called ALPHA is used by the majority of analyses which requires the user to supply initialisation, event processing, and termination subroutines. In return ALPHA unpacks the data arrayed in the BOS

banks in an event and provides user friendly macros and subroutines with which to access it. Examples are given below.

| | |
|---|---|
| `mom = QP(ITK)` | returns the momentum of track `ITK` in variable **mom**. |
| `daugh = KDAU(ITK,1)` | returns the $1^{st}$ daughter particle track number of Monte Carlo track `ITK` in variable **daugh**. |

ALPHA was used for nearly all of the following analysis.

# Chapter 4

# Towards event analysis

As has been discussed already (Chapter 2: Philosphical implications) the definition of a quark or gluon jet is, by its very nature, rather arbitrary. Indeed, the definition of a "jet" is just that - a definition. In order to make any measurements using identified quark and gluon jets it is therefore crucial that they are defined, along with the methods used to create them, in a logical and clear manner.

## 4.1 Energy Flow

In a typical hadronic event the total energy of the decay of the $Z^0$ into a $q\overline{q}$ and subsequently into a collection of hadrons would, assuming a perfect detector, result in the correct association of detector information with each particular hadron under study.

Obviously, ALEPH is not a perfect detector. In order to reconstruct an event back into its underlying hadrons using the incomplete information supplied, an intimate knowledge of the detector response to different particles is required. Modelling detector response using Monte Carlo events and test-beam data has allowed procedures which reconstruct hadronic events into a "best guess" approximation of their true structure to be developed. Such procedures are termed *Energy Flow algorithms* within the ALEPH collaboration and several have been implemented. They all use the same principles.

The simplest way to determine the total energy of an event would be to sum

all of the energy in all calorimetric cells. This method, in ALEPH, yields a mean energy of 69GeV with a resolution of ~11GeV. However, this can be improved upon by using the detector's particle identification abilities - indeed, if ALEPH could perfectly identify all leptons, photons, and charged and neutral hadrons a resolution of ~3GeV would be expected. The energy flow algorithm described below goes some way to achieving these aims[1]. It is described in [40] whence came most of this information.

### 4.1.1 Cleaning

The first stage of the algorithm is to perform a cleaning operation on all of the charged particle tracks and calorimeter clusters in order to remove spurious signals originating from non-beam spot interactions (see Section 5.2) occasional noise from the front end electronics, data acquisition problems, or reconstruction anomalies. It proceeds as follows:

1. All charged tracks reconstructed using information from the VDET, the ITC and the TPC are subject to a series of cuts similar to those of a normal hadronic event selection (see Section 5.2). They are required to have at least 4 TPC hits and to originate from a cylinder of length 20cm and diameter 4cm coaxial with the beam pipe and centred at the nominal interaction point. The momentum resolution and spatial resolution of the tracking detectors is degraded for high energy tracks with few hits. To account for this effect at least 8 TPC hits and 1 ITC hit are required for tracks with energy greater than 15GeV. All charged tracks must have a momentum greater than 200MeV.

2. Any charged track rejected in step (1) is now reinstated if it forms part of a $V^0$ pair[2]. The $V^0$s are identified in much the same way as is used inside LEPTAG (see Section 5.3.1). The decay vertex of the $V^0$ pair must lie

[1]Known as the *Janot energy flow algorithm* (after its inventor Patrick Janot) it is the standard energy flow algorithm used by most ALEPH analyses.

[2]A $V^0$ is defined as a pair of charged tracks with opposite sign originating from the decay of a neutral $K$, $\Lambda$ or $\overline{\Lambda}$ inside the detector volume.

within a cylinder of length 30cm and diameter 10cm coaxial with the beam pipe.

Tracks rejected by cleaning steps (1) and (2) are ignored in the following steps:

3. Any noisy channels which appear systematically in every event in the ECAL or HCAL are rejected.

4. Fake energy deposits are rejected by insisting on a coincidence between the anodic and cathodic read-outs of the calorimeters. In the case of the ECAL the total difference in energy measured by the towers and the wire planes must not be greater than 500MeV. For the HCAL it is required that an HCAL tower cluster must be topologically connected to a streamer tube signal.

Subsequent to the cleaning process outlined above, the kinematics of the energy flow for the event is then constructed. Each remaining charged track is extrapolated to the calorimeters where groups of topologically connected tracks and clusters are formed (known as *cal-objects* from here onwards). This grouping process is similar to jet formation which is described in Section 4.2. Each cal-object is then processed as follows:

### 4.1.2 Cal-object processing

1. Charged tracks positively identified as electrons in a similar manner to that described in Section 5.3.1 are removed from the cal-object. In addition, the energy contained in the ECAL towers associated with the charged track is also removed. If the difference between this energy and the momentum of the track is greater than three times the expected energy resolution then the excess energy is counted as neutral electromagnetic energy and is classed as originating from a bremsstrahlung photon.

2. Charged tracks positively identified as muons in a similar manner to that described in Section 5.3.2 are removed from the cal-object. In addition two subtractions from the cal-object are made. In the first, a maximum of

1GeV is subtracted from the closest associated ECAL cluster (if one exists in the cal-object). Secondly, a maximum of 400MeV per-plane-fired, near the extrapolation of the charged track, is subtracted from its corresponding HCAL cluster.

3. Photons and $\pi^0$s are now searched for. If found, they are counted as neutral electromagnetic energy and are removed from the cal-object. Photon identification relies on the facts that: (1) electromagnetic showers generally start in the first stack of ECAL and (2) unlike hadronic showers, they have a compact arrangement, sharing energy with only their nearest neighbour storeys[3]. The method proceeds as follows [6] [43]:

   - The storeys of the first stack of ECAL are scanned in order of decreasing energy. A storey without a more energetic direct neighbour defines a new cluster. If it has one or more energetic neighbours then a cluster is formed with the highest energy neighbour.
   - The same procedure is followed for stacks 2 and 3 but in these cases, when processing a storey, the algorithm looks first for a neighbour in the previous stack.
   - Photon candidates are rejected if they lie too close to the extrapolation of a charged track (<2cm). They are also required to have deposited energy in two consecutive stacks and the sum of the energy in stacks 1 and 2 must be greater than 250MeV.
   - The position of the photon candidate is calculated using an energy weighted mean of the position of the storeys contained in the cluster. It is then corrected for the finite size of the ECAL pads.
   - The energy of the photon is calculated using the four central towers of the cluster. Because the expected value of this fraction of the total energy of the photon is known from the parameterisation of the shower shape for a single photon in the ECAL (from test beam data),

[3]Nearest neighbour meaning those storeys with which the current storey shares a face.

the energy measurement from the four central towers is corrected back to the full energy.

Since a $\pi^0$ decays almost instantaneously ($\tau = (8.4 \pm 0.6) \times 10^{-17} s$) into a $\gamma\gamma$ pair ($\frac{\Gamma_{\gamma\gamma}}{\Gamma_{Total}} = 98.8\%$) [7] the $\pi^0$ identification method relies upon searching for $\gamma\gamma$ pairs with an invariant mass compatible with that of a $\pi^0$. In order to improve upon the limited energy resolution of the ECAL, the $\pi^0$ energy is recalculated using a fitting process where the opening angle of the photons is kept constant and the $\gamma\gamma$ mass is constrained to $m_{\pi^0}$. Unfortunately this is slightly more complicated at high energies because the $\gamma\gamma$ pair will be very close together in the ECAL (they may even share storeys). In this case, the opening angle of the $\gamma\gamma$ pair is allowed to vary slightly during the fit.

4. All remaining charged particle tracks and their associated calorimeter clusters, coming from the nominal interaction point or belonging to a reconstructed $V^0$ are now counted as charged energy within the cal-object (but not removed).

5. The cal-object will contain charged and neutral hadrons at this stage. Although feasible, a direct identification of neutral hadrons is difficult and has not yet been attempted. Instead a neutral hadron is identified as a significant excess of calorimetric energy in a cal-object over and above that accounted for by the charged energy contained in the object. The equation

$$E_{neutral} = E_{HCAL} + rE_{ECAL} - E_{charged} \tag{4.1}$$

can be written where $E_{neutral}$ is the residual calorimeter energy, $E_{HCAL}$ is the total HCAL energy remaining in the cal-object, $E_{ECAL}$ is the total ECAL energy remaining in the cal-object, and $E_{charged}$ is the total charged energy contained in the cal-object. $r$ is the response ratio for electrons and pions in the ECAL and has been found to be $\sim$1.3 with test-beam data. This is complicated by the fact that low energy photons escape detection

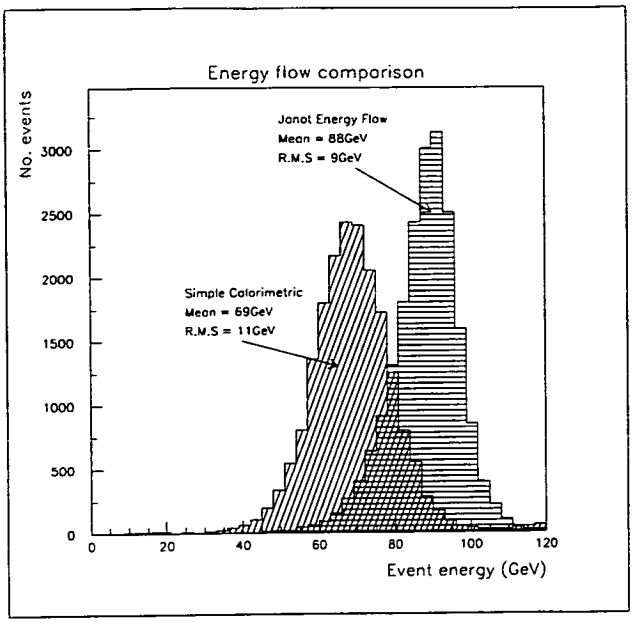


Figure 4.1: Comparison of the Janot energy flow with a naive calorimetric determination of the total energy at $E_{cm} = 91.2\text{GeV}$

in stage (3) above and so $r$ is set to 1.0, 1.3, and 1.6 in the first, second, and third stacks of the ECAL respectively to account for this.

The above procedure is repeated for all cal-objects resulting in a collection of *energy flow objects* (electrons, muons, photons, $\pi^0$s,charged hadrons, and neutral hadrons). To this list is added all the clusters found in the LCAL, where no particle identification is possible. In the following text the phrases *energy flow objects* and *energy flow particles* will be used interchangeably when referring to the output from the above algorithm.

### 4.1.3 Performance of the algorithm

In order to measure the performance of any energy flow algorithm three questions can be posed:

1. Does it recreate the centre-of-mass energy of an event reliably and with an acceptable resolution?

2. Do the number of energy flow objects match the true number of charged and neutral particles?

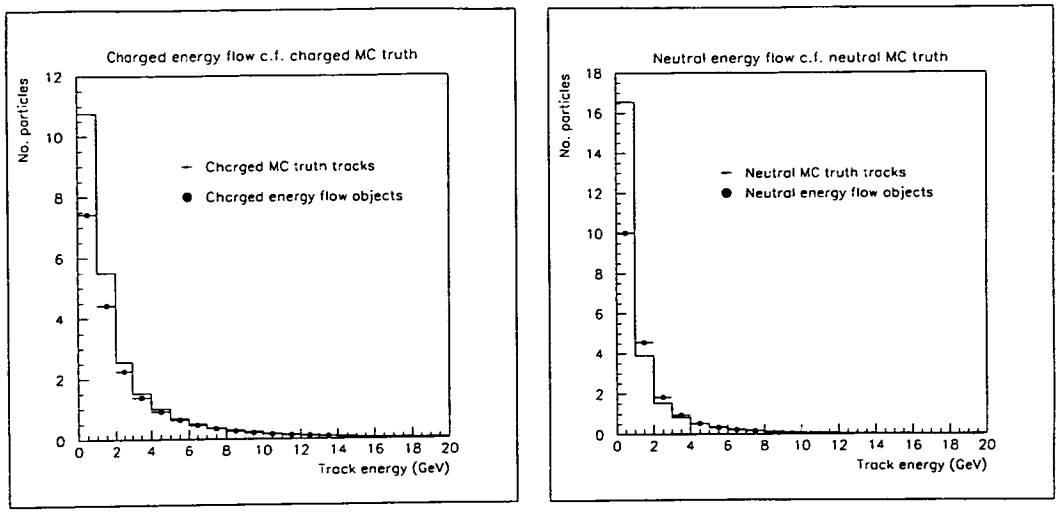


Figure 4.2: (a) Charged object energy spectrum (b) Neutral object energy spectrum

3. Does the energy spectrum of the energy flow objects correctly describe that of the true charged and neutral particles?

Any method used to determine answers to questions (2) and (3) has to rely on Monte Carlo. Question (1) however, can be answered using both real data and Monte Carlo.

Figure 4.1 shows the results of a study[4] of 20000 $q\bar{q}$ real data events. Simultaneously displayed on the plot are results from the Janot energy flow algorithm and a simple calorimetric determination of the event energy flow as was described in Section 4.1. The Janot algorithm is clearly far superior at reconstructing the centre of mass energy than the simplistic method.

The following two plots (Figures 4.2(a) and 4.2(b)) show the charged and neutral particle energy spectra of 20000 $q\bar{q}$ Monte Carlo events. As can be seen, both the reconstructed charged track and neutral object energy spectra agree tolerably well with Monte Carlo truth information (although low momentum tracks are lost as expected).

As a further example of the algorithm's power, Figure 4.3 shows a plot of total reconstructed energy against event multiplicity[5]. The total event energy and

[4]Unless otherwise stated all event data sets used in this thesis were captured or generated at the $Z^0$ peak - $E_{cm} = 91.2$GeV

[5]Inspiration for this example comes from [40].

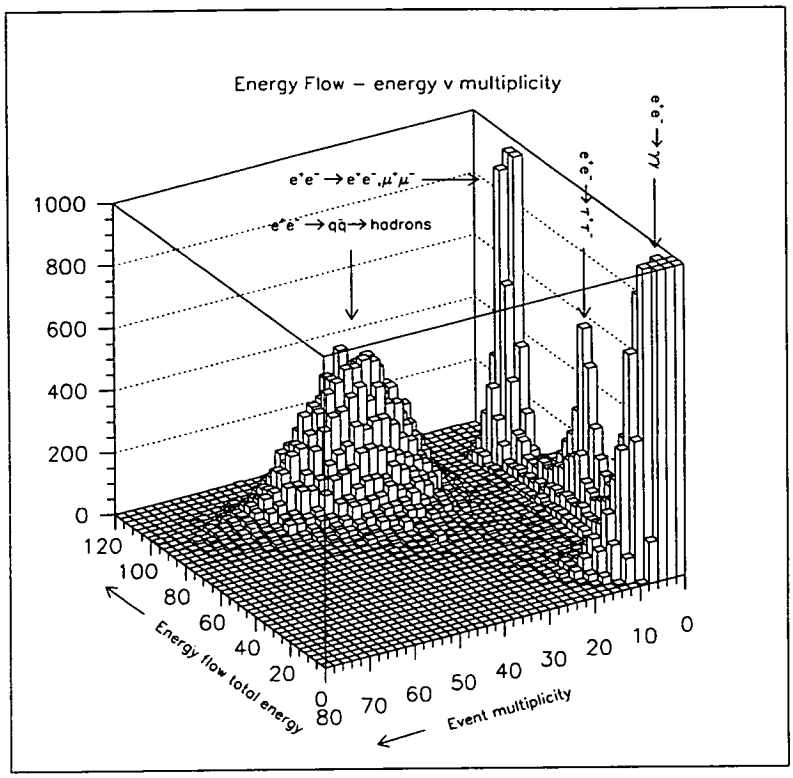


Figure 4.3: A demonstration of the power of the energy flow algorithm

total event multiplicity of 200 000 events recorded in 1992 were entered into the histogram. The $e^+e^-$ and $\gamma\gamma$ peaks have been truncated for presentation purposes. Note that placing a cut of $30\text{GeV}/c^2$ and requiring at least 15 energy flow objects in an event provides a very efficient (99.6%) multihadronic event selection mechanism. This is similar to a standard ALEPH hadronic event selection (as described in Section 5.2) but uses neutral object information in addition to the charged tracks. The charged track only method is the standard method used by ALEPH because it was available well before the Janot energy flow algorithm was implemented.

## 4.2 Jet creation algorithms and $y_{cut}$

### 4.2.1 JADE

In Chapter 1 it was stated that the principal aim of this thesis was to study 3-jet events and to compare their constituent quark and gluon jets. So far the nature of these "jets", their relation to the physics problem under study, and a definition

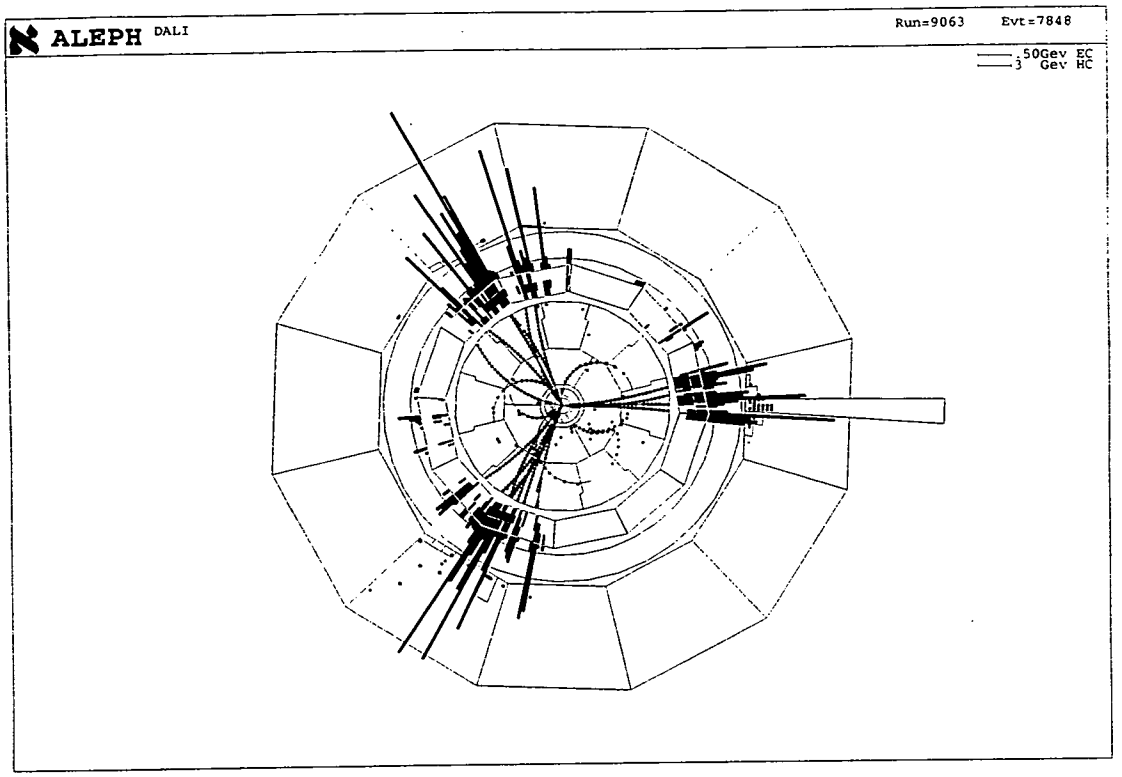


Figure 4.4: A DALI image of an hadronic event

of the methods and parameters used in this work have not been discussed. In this section we intend to shed light on these vitally important, but rather confusing, issues.

Figure 4.4 shows an hadronic event captured by ALEPH. This particular event was chosen because it clearly shows that the charged tracks and calorimeter hits are not distributed evenly over the whole detector volume but rather that they are grouped into three "jets" of particles. The task of any jet creation algorithm is therefore to select those tracks which belong to a particular jet and combine them together in some way. Obviously, few events have such clearly defined jets as shown in Figure 4.4 and the definition of theoretically predictable algorithms has been a subject of interest in QCD for some time.

Since the first experimental evidence for jet structure was reported [34] many different algorithms have been suggested. Some of these, for instance hemispheric algorithms which split a 2-jet event into two halves assigning all the tracks in one hemisphere to one jet and vice versa, were obviously not useful for this analysis. Instead, a particle by particle clustering algorithm was chosen. Several such

algorithms exist (LUCLUS, JADE, DURHAM, PTCLUS, etc.) and these may also have subtle variations (for instance the recombination scheme chosen [see later]).

The most commonly used algorithm within the ALEPH collaboration is the JADE algorithm [38]. This uses an invariant mass measure to decide which particles to cluster together. The clustering process proceeds as follows:

- The algorithm starts with a set of clusterable particles (eg. charged tracks or energy flow objects).
- For each pair of tracks the invariant mass measure (usually denoted by $y$) is calculated.
- The particle pair with the smallest value of this measure are then combined into a single particle using a recombination scheme (see later).
- The previous two steps are then repeated. On each repetition the number of particles will reduce by one.

If allowed to continue unchecked the algorithm will result in a single particle (not a desirable result). For this reason the concept of $y_{cut}$ is introduced. The algorithm is forced to stop clustering when the minimum value calculated by the invariant mass measure, for each remaining pair of objects in an event, is greater than the value of $y_{cut}$. In this way the initial particles in an event are clustered into jets.

Naively one might choose the scaled squared invariant mass

$$\frac{M_{ij}^2}{E_{vis}^2} = \frac{(E_i + E_j)^2 - (P_i + P_j)^2}{E_{vis}^2} \equiv y \tag{4.2}$$

as $y$ in the algorithm. Unfortunately it has been known for some years [53](page 264) that this metric suffers from severe instability. This is due to its preference to start by clustering the particles of low momenta and only subsequently to cluster the higher momentum tracks. Therefore, rather than clustering slow particles around the fast ones the algorithm will proceed in the opposite manner producing jets with rather bizarre assignments.

In order to ameliorate the problem somewhat, the JADE collaboration [38] proposed the following definition for $y$ which is essentially a scaled pseudo invariant mass measure:

$$y_{ij} = \frac{2E_iE_j(1-\cos\theta_{ij})}{E_{vis}^2}. \tag{4.3}$$

The use of $E_{vis}$ (the visible energy) rather than $E_{cm}$ (the centre of mass energy) in the denominator attempts to make the metric less sensitive to detector effects. In the case of $m_i = m_j = 0$ the two metrics are identical. However, in the case where $m_i$ and $m_j$ both have non vanishing masses, as the net momentum increases ($\theta_{ij} \to 0$) so $y_{ij}$ will tend to zero in the JADE case. In the squared invariant mass measure however, $y$ can never reach zero and low energy pairs are favoured. As a result, the JADE metric is considerably more stable.

### 4.2.2 DURHAM

The JADE algorithm has been used successfully for many years. However, it became apparent relatively recently that the algorithm has some limitations at low values of $y_{cut}$. It is easiest to understand this by considering Figure 4.5 which shows the number of jets after clustering versus $y_{cut}$. One of the most powerful methods devised for measuring the strong coupling constant ($\alpha_s$) at LEP has been the use of the variation of the 3-jet fraction ($f_3(y)$) which is known using fixed-order perturbation theory to next-to-leading order and therefore provides a direct measurement of $\alpha_s$. In order to minimise the statistical error on the measurement, small values of $y_{cut}$ are used where the 3-jet rate is greatest. However, at such low values of $y$, attempts to fit $f_3$ require very small (unphysical) values of the renormalisation scale factor $\mu$ (see Section 2.3).

In [8] Stirling and Brown discuss this problem and show that it arises due to the effective expansion parameter at low $y$ in the fixed-order perturbative calculation of $f_n$ being $(C_F\alpha_s/\pi)\ln^2 y$. At small $y$ these double logarithms become important and must be cancelled from the perturbative calculation by resumming them to all orders in $\alpha_s$ before a reliable prediction can be made. Stirling and Brown investigated the possibility that there was some natural exponential

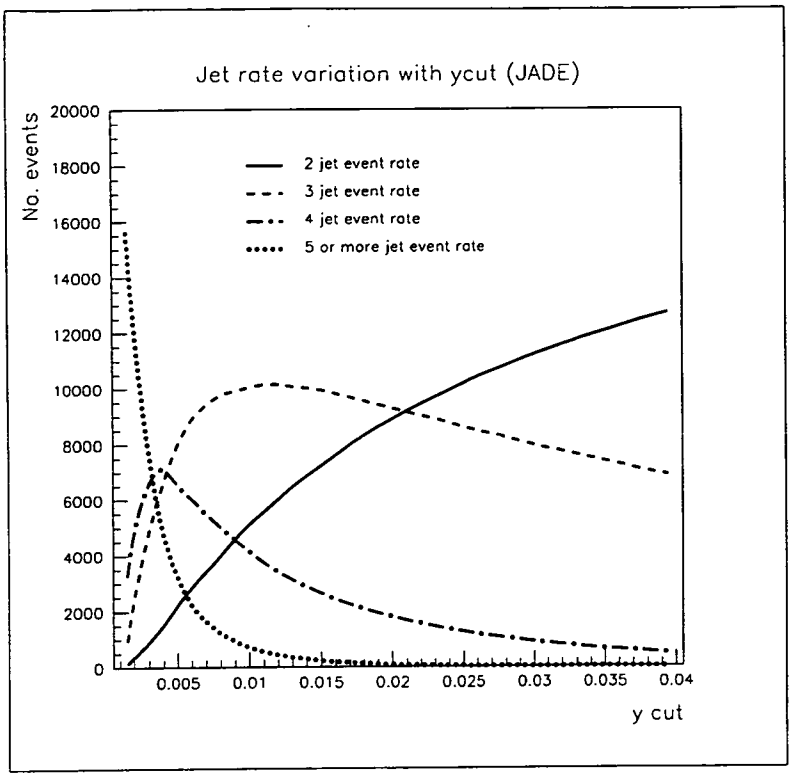


Figure 4.5: The variation of number of jets in an event with $y_{cut}$ using the JADE algorithm

series of these leading double logarithms over all orders (exponentiation has been found to be required wherever the resummation technique has been applied successfully). They discovered that no simple exponential series exists and that the reason for this is closely linked to the definition of the JADE algorithm.

The above statements are best explained using the same example as Stirling and Brown do in [9]. Consider Figure 4.6. Assume that $E_1$ and $E_2$ are close to

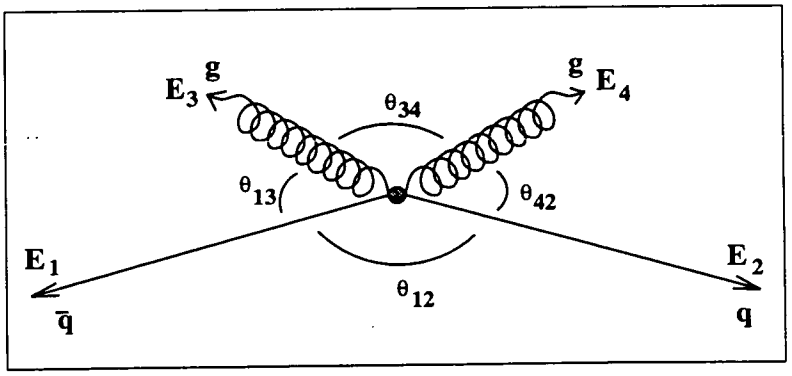


Figure 4.6: A $q\bar{q}gg$ configuration which the JADE algorithm incorrectly assigns to a 3-jet final state

$E_{beam}$ (the beam energy), while $E_3$ and $E_4$ are much less. Given that $\theta_{13}$ and $\theta_{42}$ are small it is easy to imagine a situation where the scaled invariant mass ($y$), calculated according to the JADE metric, is approximately equal for $y_{13}$, $y_{34}$ and $y_{42}$. If it happens to be the case that $y_{34}$ is the smallest then JADE will cluster the two soft gluons into a single cluster of momentum $(\vec{p_3} + \vec{p_4})$. This cluster is obviously erroneous - the natural pairing being $y_{13}$ and $y_{42}$. As the new cluster is approximately perpendicular to the two quarks, and given a reasonable value of $y_{cut}$, it is unlikely that the new cluster would be combined with either of the two quarks at the next step. A natural 2-jet configuration has resulted in a spurious 3-jet final state. This is mainly due to the $E_iE_j$ product in the numerator of the metric. As Stirling and Brown show in [8] this unnatural assignment by the JADE algorithm is enough to spoil any chance of simple resummation via exponentiation.

To resolve this problem a new algorithm was proposed at the Durham Workshop on Jet Studies at LEP and HERA held at Durham University in 1990 [52]. This has (unsurprisingly) become known as the "DURHAM" algorithm. It proceeds in exactly the same manner as the JADE algorithm except the JADE minimum invariant mass metric is replaced by a relative transverse momentum measure:

$$y_{ij} = \frac{2\min(E_i^2, E_j^2)(1 - \cos\theta_{ij})}{E_{vis}^2}. \tag{4.4}$$

This cures the problem discussed in the example above (a correct 2-jet configuration results) and in addition it has been shown in [9] and [13] that the leading logarithms do resum exponentially to any order at low $y_{cut}$. The DURHAM algorithm has been used throughout this analysis except when attempting to identify high $P_\perp$ leptons where the JADE algorithm was used in accordance with the official ALEPH high $P_\perp$ lepton identification definition [1].

### 4.2.3 Recombination scheme

In addition to the choice of clustering metric another decision has to be made concerning how the chosen particles are combined together. Nearly as many

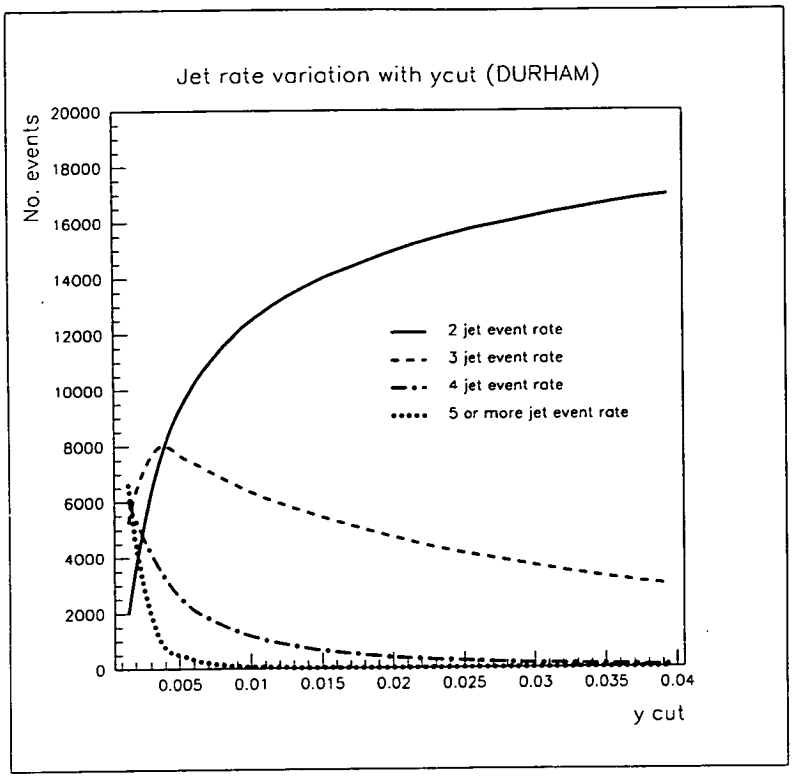


Figure 4.7: The variation of number of jets in an event with $y_{cut}$

choices for this exist as there are clustering algorithms. The simplest of these schemes is known as the "E-scheme" whereby particles are clustered simply by summing their energy and momentum:

$$\begin{aligned} E_{ij} &= E_i + E_j \\ \vec{P}_{ij} &= \vec{P}_i + \vec{P}_j \end{aligned} \tag{4.5}$$

As no reason was found during this work to prefer one of the other schemes the E-scheme was used throughout.

### 4.2.4 What value of $y_{cut}$?

So far little has been said about which value of $y_{cut}$ to use. It should be apparent by now that there is no single correct value and the final choice greatly depends on the proposed application. Figure 4.7 shows the variation of number of jets in an event with $y_{cut}$ using the DURHAM algorithm and the E-scheme[6]. The

[6]If this plot is compared with Figure 4.5 it is obvious that JADE $y_{cut}$ is not identical to DURHAM $y_{cut}$. A "rule of thumb" exists however which states that $y_{JADE} \simeq 4 \times y_{DURHAM}$.

| $y_{cut}$ | 3-jet events N°. of events | % of total | Overlap $O_{ij} \geq 1$ | % |
|---|---|---|---|---|
| 0.0010 | 5254 | 26.3 | 3681 | 70.1 |
| 0.0025 | 7799 | 39.0 | 4332 | 55.5 |
| 0.0050 | 7534 | 37.7 | 3210 | 42.6 |
| 0.0075 | 6837 | 34.2 | 2420 | 35.4 |
| 0.0100 | 6217 | 31.1 | 1891 | 30.4 |
| 0.0250 | 4050 | 20.3 | 696 | 17.2 |
| 0.0500 | 2370 | 11.9 | 185 | 7.8 |

Table 4.1: The variation of overlap with $y_{cut}$.

data used for this plot correspond to 20000 hadronic events recorded by ALEPH in 1992. The natural choice for this analysis would have been to maximise the 3-jet rate suggesting a $y_{cut}$ of ~0.004. However, as $y_{cut}$ decreases and the 3-jet rate increases the "extra" 3-jet events are likely to be natural 2-jet events where one of the jets has been artificially split into two. The implication of this is that as $y_{cut}$ decreases the chances that a jet in a 2-jet event which is most naturally described as belonging to a 2-jet configuration will be reclassified erroneously as coming from a 3-jet configuration. In an attempt to understand this the following procedure was designed:

- The maximum width ($\theta_i$) of each jet in a 3-jet event is found by calculating the angle each particle in each jet makes with its jet axis.
- The angle $\theta_{ij}$ between each pair of jets is calculated.
- The overlap ($O_{ij}$) is then calculated for each pair of jets ($i$ and $j$):

$$O_{ij} = \frac{\theta_i + \theta_j}{\theta_{ij}} \tag{4.6}$$

- If $O_{ij} < 1$ no jet overlap is possible. If $O_{ij} \geq 1$ then the particles in the two jets may overlap each other.

Table 4.1 shows how overlap varies with $y_{cut}$ and is based on the same data set as was used for Figure 4.7. Only the maximum value of overlap in an event was used to generate the table. Too low a $y_{cut}$ implies poorly defined jets with a high probability that some jet overlap will have occured. Too high a value of

$y_{cut}$ implies well defined jets but at a low rate. It is important to note that a value of $O_{ij} \geq 1$ only suggests the jets *may* overlap, not that they do.

The value of $y_{cut}$ finally chosen for this analysis was 0.01, this being a compromise between jet definition and high jet rate. Similar work performed by the OPAL collaboration [32] chose the same $y_{cut}$ independently.

## 4.3 Analysis levels

When analysing real data there is only one type of information available - the data from the detector consisting of tracks, calorimeter hits, run information etc. etc. When analysing Monte Carlo data there is obviously a much more comprehensive array of information available since all particle information from the $e^+e^-$ beam particles, through the $Z^0$ shower, string formation, hadronisation products, and reconstructed detected particles is stored as part of the event. Retaining this information and the links between different parts of it is extremely useful, particularly in an analysis such as this where the ability to trace the particle flow from the primary quarks through to the detected particles was vital to assess tagging purity and efficiency.

The definition of three "levels" of analysis within Real and Monte Carlo data proved useful. These became known as the parton level (comprising the particles occuring just before hadronisation in the Monte Carlo truth), the hadron level (comprising the particles occuring just after hadronisation in the Monte Carlo truth), and the detector level. They are detailed below.

### 4.3.1 Detector level

This was obviously the only level available in real data. Events were selected according to the standard ALEPH hadronic event selection (see Section 5.2). The energy flow objects provided by the Janot algorithm were clustered using the DURHAM algorithm and E-scheme recombination method with $y_{cut} = 0.01$. By definition the primary aim of the Monte Carlo is to recreate this level as closely as possible. Real and Monte Carlo data were treated identically.

At the two lower levels the total energy of each jet was known with complete accuracy because no detector effects were included at these levels. At the detector level the measured energy of a jet is given by the sum of the energy of each energy flow object comprising that jet. This is known as the measured energy of the jet. It was found that the energy of a jet could also be determined using the constraint that the sum of the three jet energies should equal the centre-of-mass energy and the sum of the momentum should be zero. The calculated energy method is outlined below. It was found that using the calculated energy of a jet reflected the true jet energy better than using the measured energy.

For momentum to be conserved the three jets in an event must lie in a plane. The energy calculation method uses this constraint and the angles between the jets, after they have been projected onto the calculated event plane, to calculate the energy of the jet relative to the centre of mass energy. The method proceeds as follows:

- The sphericity tensor

$$S^{\alpha\beta} = \frac{\sum_{i=1}^{N} p_i^{\alpha} p_i^{\beta}}{\sum_{i=1}^{N} |p_i|^2}, \tag{4.7}$$

  is computed where $\alpha, \beta = 1, 2, 3$ correspond to the $x$, $y$, and $z$ components of the $N$ energy flow objects in the event.

- The resulting matrix $S^{\alpha\beta}$ is then diagonalised and three eigenvalues, $\lambda_1 \geq \lambda_2 \geq \lambda_3$ where $\lambda_1 + \lambda_2 + \lambda_3 = 1$, are found.

- Eigenvectors, $v_1$, $v_2$, and $v_3$, corresponding to the three eigenvalues are then found.

- The cross product, $v_1 \times v_2$, defines a normal vector to the event plane of the event.

- Each jet is projected onto the event plane as a unit vector. The angles between each of these projected jets, $\theta_{12}$, $\theta_{23}$ and $\theta_{31}$, are then found.

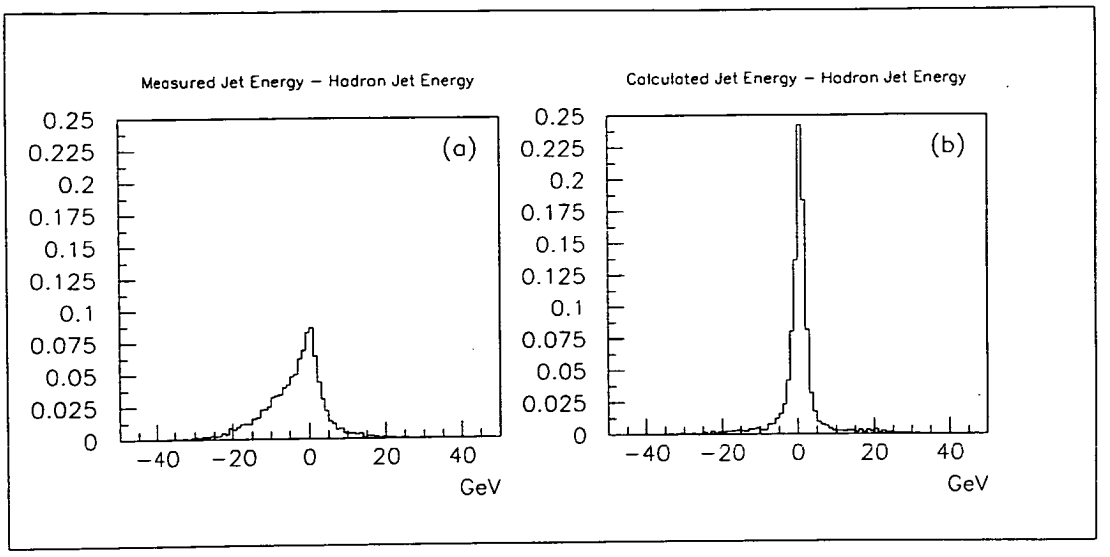


Figure 4.8: Comparison of (a) the measured energy flow jet energy and (b) the calculated jet energy methods

- The energy of each jet is then calculated using the formula:

$$E_{jet}(i) = E_{c.m.}\frac{\sin\theta_{jk}}{\sin\theta_{12} + \sin\theta_{23} + \sin\theta_{31}} \tag{4.8}$$

where $i = 1, 2, 3$ with $jk = 23, 31, 12$.

Figure 4.8 shows the suitability and good performance of this technique compared to using the measured energy of the jets. The data used corresponds to the same set of tagged 1992 Monte Carlo events as will be discussed in Section 6.2. The plots rely on using jets created at the hadron level (the level which is described next) and matching these jets to the detector level jets. Angular matching is used which will be described shortly. In Figure 4.8(a) the difference in energy between the energy flow measured energy of each jet minus the hadron level energy is shown. Figure 4.8(b) shows the equivalent plot but using the calculated energy of the jet instead of the measured energy. The superiority of the calculated jet energy method is apparent.

### 4.3.2 Hadron level

In fully reconstructed Monte Carlo data the complete decay structure (the Monte Carlo "truth" information) produced by the event generator is stored in addition

to the reconstructed detector level information. This level was useful because it is in some respects an interface between the detector level and the most fundamental level. The particles in this level were selected from the complete set of Monte Carlo truth particles by requiring that they were stable where, to be classed as stable, they must have one of the following three attributes:

1. The particle does not decay.
2. The particle is a neutral particle which decays in the calorimeter volume or a charged particle which decays in the TPC or calorimeter volume.
3. The particle interacts with matter before reaching the detector volume.

If a particle was selected then none of its ancestors or descendants were included in the selection (ie. double counting does not occur). Particles of type 3 were selected as opposed to their descendants so that the sum of the energy of all selected particles was equal to that of the $Z^0$ decay. This level therefore represented a clean picture of the post-hadronisation products of the $Z^0$ decay with no smearing or particle loss due to the limited detection capabilities of ALEPH.

Jets at this level were created in identical fashion to those at the detector level. Because energy was conserved at this level $E_{vis}$ was equivalent to $E_{Z^0}$. At some instances during this work it was useful to cluster the selected particles until exactly three jets remained (irrespective of the final value of $y_{cut}$) for direct comparison to the upper and lower levels. This technique was used predominately at the most fundamental level as is discussed next.

### 4.3.3 Parton level

In Chapter 2 the process $e^+e^- \rightarrow Z^0 \rightarrow q\bar{q} \rightarrow hadrons$ was discussed in detail. The philosophical implications of attempting to study hard QCD processes using the decay remnants of the initial $q\bar{q}g$ configuration was also discussed. Notwithstanding these considerations some attempt at creating pre-string, or parton level, jets had to be made in order to gather purity and efficiency information

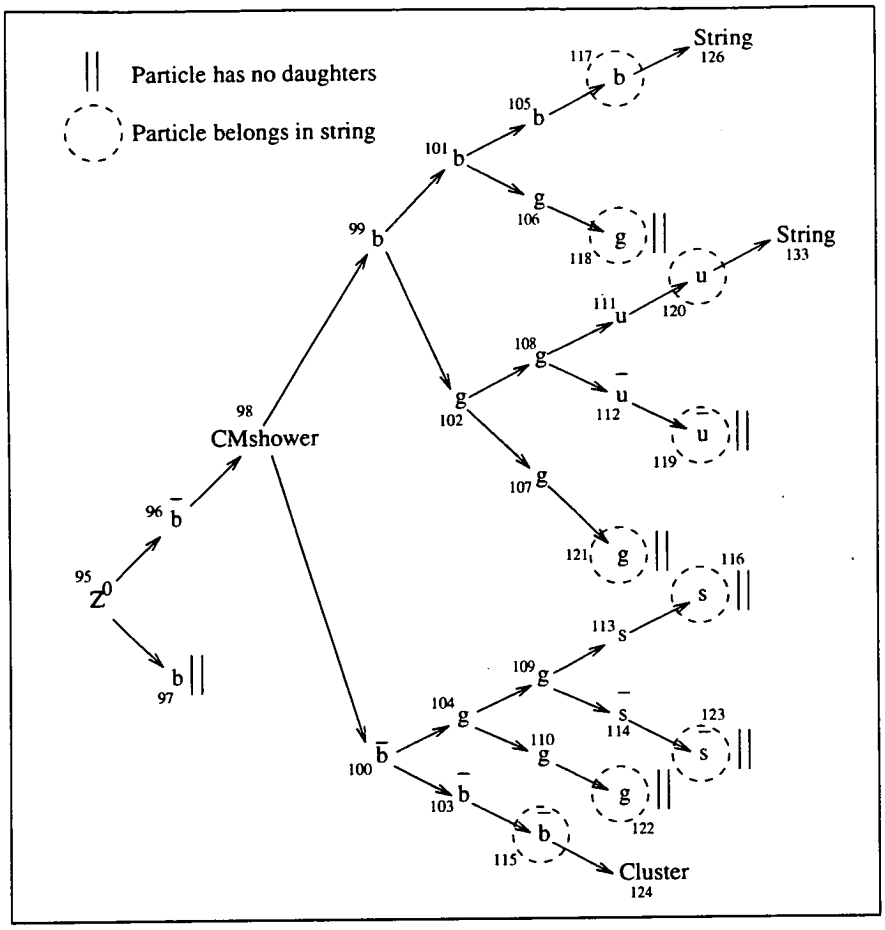


Figure 4.9: Typical JETSET 7.3 shower evolution and string formation

and the procedure adopted is described below. A large number of choices were made whilst arriving at the procedures described. To avoid tedium only major alternatives are given but it should be realised that honing this method took a considerable period of time.

The physics underpinning the two Monte Carlo programs used in this analysis (JETSET 7.3 [53] and HERWIG 5.6 [45]) was described in Chapter 2. Because the two programs generate events differently the structure of their event records are different. Finding those partons existing directly before hadronisation was handled differently for each program.

### JETSET 7.3

Figure 4.9 depicts an actual Monte Carlo $b\bar{b}$ event. It shows the mother to daughter relationships for the parton shower particles from the $Z^0$ particle to

those particles which comprise the string. Beside each particle is its event record index number provided by the ALEPH analysis software. The method used to construct the string proceeds as follows:

- The $Z^0$ is found and hence its two daughter initial state quarks [7].
- Assuming a shower has occurred (occasionally very collinear 2-jet events are generated where neither initial quark radiates any gluons thereby obviating the need for a *CMshower* particle) one of the quarks will have as its daughter a *CMshower* particle.
- The *CMshower* is a "bookkeeping" particle as are the *String* and *Cluster* particles. The two quarks and $Z^0$ before the *CMshower* are now ignored and the mother to daughter relationships are followed from the *CMshower* onwards.
- A branch ends when:
  - a mother has no daughters,
  - the daughter is a *String* particle,
  - or the daughter is a *Cluster* particle.
- All those particles at the end of a branch comprise the string

In most cases only one *String* particle exists in the event record. There are two in this example due to the presence of the *Cluster* particle which splits the string in the event record. Cluster particles are rare (and to my knowledge undocumented).

There is one additional complexity to the algorithm. Very occasionally one of the quarks will have a photon as a daughter (via radiation). These are included in the string for energy conservation purposes. If the photon subsequently decays into a lepton pair (via pair production) the photon is included in the string but not the lepton pair.

[7] When JETSET is used in matrix element mode the parton level event record is as simple as this. The $Z^0$ has two, three or four daughters corresponding to $q\bar{q}$, $q\bar{q}g$, $q\bar{q}q\bar{q}$, and $q\bar{q}gg$ final states. The first and last daughters in the list are identified as the primary quarks

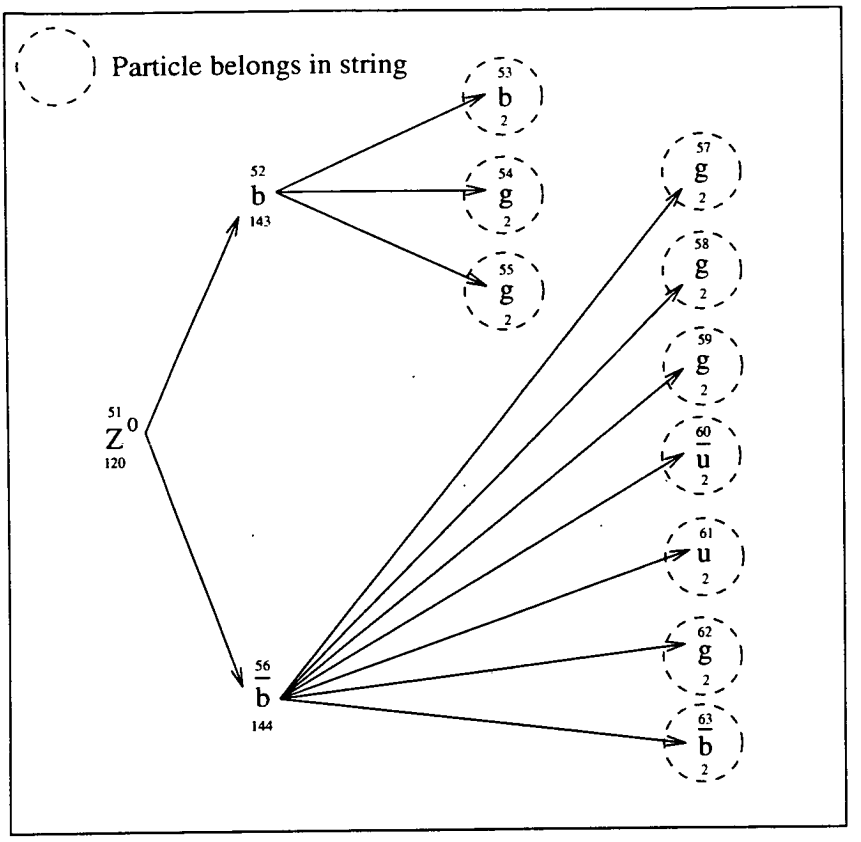


Figure 4.10: HERWIG 5.6 string formation from event record

**HERWIG 5.6**

Not surprisingly, considering the very different philosophies behind JETSET and HERWIG, the event record structure of a HERWIG 5.6 generated event is considerably different from that described above. Therefore, a completely different procedure was designed to find the pre-hadronisation particles. One of the difficulties with HERWIG was deciding which event record partons should comprise the string. As was discussed earlier, HERWIG goes through the following processes before hadronisation: hard subprocess, parton shower, gluon splitting, and cluster formation. Since the "string" of partons produced by the JETSET algorithm is most similar to the partons in the event record after the parton shower and before gluon splitting, this collection of partons was chosen to represent the parton level.

Figure 4.10 depicts an actual Monte Carlo $b\bar{b}$ event generated by HERWIG 5.6. The method chosen relies heavily on the event record status code associated with each parton and this number is given underneath each parton name. The

index number provided by the ALEPH analysis software is on top. The method proceeds as follows:

- The $Z^0$ is found (status code 120) and hence it's two daughter quarks which will have status codes 143 and 144.
- Each of these daughter quarks will have a large number of daughters.
- Only those daughters with status code 2 (corresponding to a "parton before hadronisation") are chosen. All other daughters are discarded.

### Jet formation

Having selected those partons which comprise the pre-hadronisation partons for both Monte Carlos they were then clustered into jets. The clustering method (DURHAM and the E-scheme) was kept the same at each level to allow unbiased comparisons between levels to be made. This however raised the issue of how to compare the jets in one level with those of another if the two levels contained different numbers of jets.

Initially these events, for instance an event which had three jets at the detector level but only two at the parton level, were classified as "ambiguous". Events of this type were found to account for ~17% of all events and since no information on the gluon purity within this sample was available it was decided that this was not an optimum method to compare the different levels.

For the above reason the convention was adopted that the uppermost analysis level (generally the detector level but also the hadron level in non-reconstructed Monte Carlo analysis) defined the number of jets in the event. Lower levels were therefore clustered using exactly the same algorithm as the uppermost level (DURHAM and the E-scheme) but instead of ceasing clustering at a particular $y_{cut}$, the clustering continued until three jets remained. It is possible to level the accusation at this point that the level of interest was the parton level; therefore why did the analysis not try to correct the upper levels back to the parton level? No satisfactory method to proceed in this manner was found; further, the analysis presented here can be thought of as being "data-centric" as opposed

to "parton-centric". Looking at the analysis from the data-centric view point reduces considerably the reliance on believing a particular Monte Carlo picture of the sub-atomic world.

A small number of ambiguous events still remained (see later) which contained only two partons to start with. These were deemed to represent highly collinear 2-jet events. The tagged gluon jet at the uppermost level was therefore deemed to have been incorrectly identified.

### Primary quark identification

The task of deciding whether a clustered parton jet was a quark or a gluon was initially performed as follows:

- Each quark was assigned a value of $P_v = +1$, each anti-quark a value of $P_v = -1$, and each gluon and photon a value of $P_v = 0$.
- The sum of the values assigned to partons in each jet was then computed separately with the result identifying the type of jet.
- $\sum_{partons} P_v = +1 \equiv$ quark jet
- $\sum_{partons} P_v = -1 \equiv$ anti-quark jet
- $\sum_{partons} P_v = 0 \equiv$ gluon

The problem with this method was that it suffered from ambiguities. In the correct case one quark, one gluon, and one anti-quark (a +1,0,-1 pattern) was found. However ~3% of the time the pattern was not as above because one or more of the quarks had been clustered into the wrong jet. This susceptibility to produce erroneous results irrespective of the significance of the errant parton was the reason for searching for a more effective method.

The method finally chosen uses the information stored in the event records produced by the Monte Carlo generators. As described earlier the event records for the different Monte Carlos differ greatly and two separate methods were therefore developed.

If the event was generated using JETSET the primary quark mother to daughter relationships can be followed through the shower (each quark can only have one daughter quark which is itself a quark). Those partons which comprise the string therefore have one parton identified as the primary quark and one parton identified as the primary anti-quark. The jet to which these two partons belong may then be tagged as that type. The remaining jet being the gluon jet. This method was used successfully for the JETSET events. In Figure 4.9 particle 117 would be identified as the primary quark and 115 as the primary anti-quark.

For events generated via HERWIG it is not possible to use the above method as the inital state primary quarks may have several daughters which are also quarks. After correspondence with the HERWIG author (Dr Brian Webber [54]) it was ascertained that the event record is constructed in such a way that the first daughter of the status code 143 parton is always a primary quark or anti-quark as is the last daughter of the status code 144 particle. In Figure 4.10 particle 53 would be identified as the primary quark and particle 63 as the primary anti-quark. The jet identification is the same.

### 4.3.4 Matching between levels

In order to compare one level to another some method whereby the jets could be matched to their corresponding jet in the other level had to be devised. It is in theory possible to match between the detector and hadron levels using information provided by the detector simulation program GALEPH which is made available to the user when reading Monte Carlo events using ALPHA. This method would allow charged tracks at the detector level to be matched precisely with their hadron level counterparts. However, a similar process for neutral objects is not available and the technicalities of making this method work are not trivial. Additionally, applying this method to matching between the hadron and parton level would not be possible as no software link is maintained between pre- and post-hadronisation objects (as would be expected from the theoretical viewpoint).

Instead a method of angularly matching jets in one level to another was

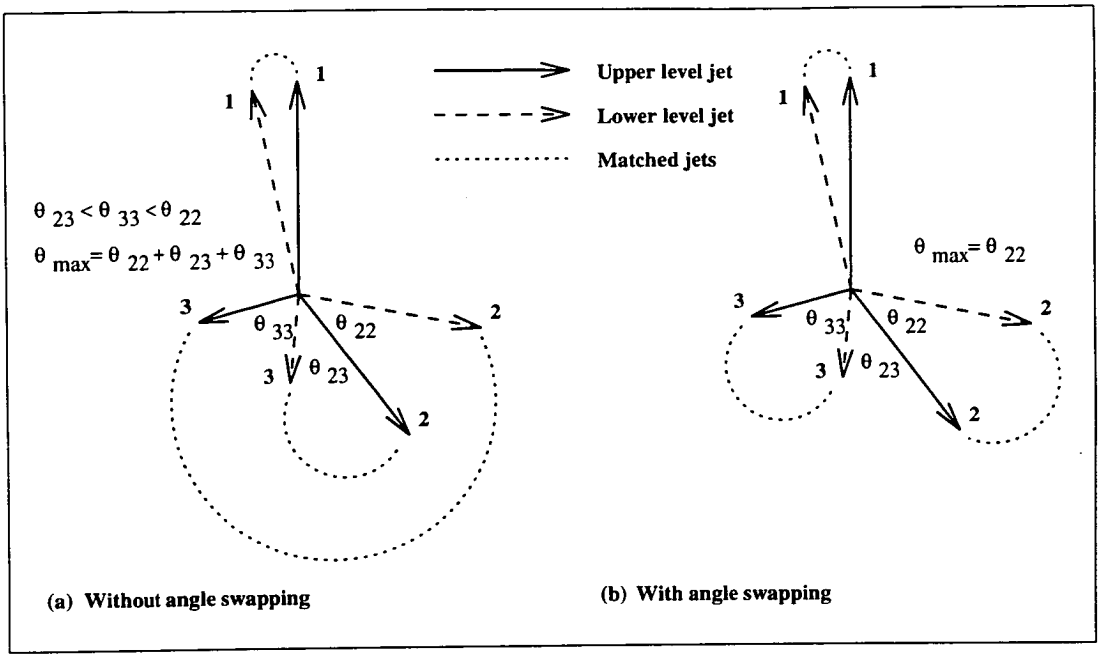


Figure 4.11: (a) Matched jets with no reassociation (b) Matched jets reassociated to minimise $\theta_{max}$

developed. The method chosen is essentially the simplest possible with a small modification[8]:

- The angle between each jet in the upper level and each jet in the lower level is found - a total of nine angles.
- The jet pair from the upper and lower levels with the smallest matching angle are chosen - leaving four angles.

Instead of repeating the above steps for the remaining two pairs of jets a different approach is taken (see Figure 4.11). If matching were to proceed as in the left hand diagram the association would be incorrect. The right hand diagram shows the association using the chosen method. There are two possible pairings of the remaining two jets. Each pairing involves two matching angles. The pairing containing the largest matching angle is rejected. The final maximum matching angle, $\theta_{max}$ is stored for later use.

In the vast majority of cases $\cos(\theta_{max})$ is greater than 0.8 and the jets in the different levels are well matched with no ambiguity. Actual figures for the

[8]This modification was suggested by a fellow ALEPH QCD group collaborator (A. Moutoussi) at a meeting and while eminently sensible has little quantitative effect.

distribution of $\theta_{max}$ vary depending on the study in question and these are given in Chapter 6.

Before results using these methods can be given the technique used to identify quark and gluon jets at the detector level must be described. The following chapter describes in detail how this was performed.

# Chapter 5

# High $P_\perp$ Lepton Tagging of Heavy Quark Events

In the previous chapter a great deal was written about the technicalities of quark and gluon jet identification using Monte Carlo truth information. Conversely, the method of jet "tagging" used with detected data was alluded to but not described in any detail. This chapter redresses the balance by describing the method devised to tag quark jet candidates and hence "anti-tag" the gluon jet in 3-jet events.

The basic theoretical underpinning of the method is first described followed by full details of the ALEPH hadronic event selection. The estimators used to identify the tagging particles (electrons and muons)[1] are then described with the precise method adopted to select them by the ALEPH collaboration. At the outset no collaboration software existed which implemented the selection method correctly. In conjunction with another project (the BTAGDST project [24]) the LEPTAG program was developed to fill this gap. The program design, structure, and functionality is described followed by the output "bank" structure. Finally, the quark jet tagging method devised for this analysis is described.

[1] In this chapter the word *electron* is used to signify the $e^+$ or $e^-$ particle. The word *muon* is used to signify the $\mu^+$ or $\mu^-$ particle.

## 5.1 The Semi-Leptonic Decays of the $B$ and $D$ Mesons

Given the desire to separate the two quark jets from the gluon jet in a 3-jet event, any suitable method must utilise a distinguishing feature of one of the two types of jet. Such a distinguishing feature is provided by the semi-leptonic decay of $B$ and $D$ mesons. In an event where the primary decay is either $Z^0 \rightarrow b\bar{b}g$ or $Z^0 \rightarrow c\bar{c}g$ the probability that the hard radiated gluon will decay into a $b\bar{b}$ or $c\bar{c}$ pair is low because such a process is kinematically disfavoured.

There are several types of $B$ and $D$ mesons, the similarity being that one of the quarks in a $B$ meson is a $b$ quark whilst one of the quarks in a $D$ meson is always a $c$. Full listings are given in [7]. Of the various possible decays of these mesons, those of interest are grouped under the title "semi-leptonic" because they take the form $B$ or $D \rightarrow l^{\pm}\nu_l X$ where $l$ is either an electron or muon, $\nu_l$ is the corresponding electron or muon neutrino, and $X$ is one or more other particles. The commonest forms of the $B$ meson are the $B^+ = u\bar{b}$, $B^0 = d\bar{b}$, and $B^- = \bar{u}b$. Likewise, the most common $D$ mesons are the $D^+ = c\bar{d}$, $D^0 = c\bar{u}$ and $D^- = \bar{c}d$. Decays of these mesons involve the flavour change of the $b$ or $c$ quark and so must proceed via the weak interaction. The GIM mechanism [36] outlaws flavour changing neutral currents, therefore the flavour change must occur via the $W^{\pm}$ boson. Figure 5.1 shows two examples of meson decay both of which demonstrate the spectator model. Other possible decay channels are via $W$ exchange or $W$ annihilation but due to kinematic considerations these are heavily suppressed and the spectator process dominates.

Of the five possible flavours of primary quark produced in $Z^0$ hadronic events, the measured probability of a particular flavour being produced is approximately one fifth. Of the $b\bar{b}$ sample, 20% subsequently decay semi-leptonically, while only 15% of the $c\bar{c}$ sample follow suit. There are few, if any, other processes which can produce a highly energetic lepton in a jet. Searching for such a lepton therefore identifies the event as a heavy quark event. In order to separate the $b\bar{b}$ from the $c\bar{c}$ events a transverse momentum ($P_{\perp}$) cut, measured with respect to the jet axis

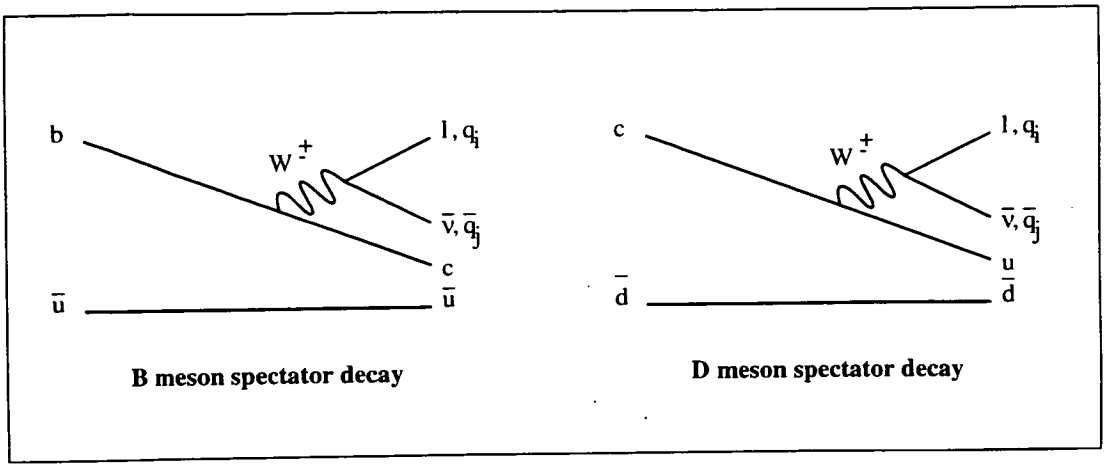


Figure 5.1: Examples of $B$ and $D$ meson decay

containing the lepton, has traditionally been applied [2](Page 284). The rationale behind this being that since the $B$ meson has considerably more mass than the $D$ meson, it's decay products will have higher momentum in the rest frame of the parent meson than those originating from a similar $D$ meson decay. Of course, if the decay products are emitted parallel to the direction of travel (back-to-back in the case of the 2-body semi-leptonic decay) the $P_\perp$ cut removes both $D$ and $B$ meson events. These losses have to be compared with the gain to $b$ event purity provided by the $P_\perp$ cut. It is also the case that the $P_\perp$ cut removes candidate high momentum "leptons" which are in reality badly identified hadrons (these having no particular $P_\perp$ bias).

## 5.2 The Standard ALEPH Hadronic Event Selection

The purpose of the hadronic selection[2], which is used throughout the ALEPH collaboration, is to select $e^+e^- \rightarrow Z^0 \rightarrow q\bar{q}$ events with maximum purity and efficiency. In addition to hadronic events the ALEPH detector captures $e^+e^-$ pairs, $\mu^+\mu^-$ pairs, $\tau^+\tau^-$ pairs, events from two photon processes, beam-gas events (showers of charged particles caused by the incidence of a high energy electron on a remaining gas molecule in the evacuated beam pipe), and cosmic rays. The

[2]This is known within the ALEPH collaboration as a "Class 16" event selection.

chosen selection method has been found to have an efficiency of $(97.4 \pm 0.3)\%$ [4]. The only measurable background remaining in the hadronic sample arises from $e^+e^- \rightarrow Z^0 \rightarrow \tau^+\tau^-$ events and amounts to a contamination of $(0.26 \pm 0.03)\%$.

An event is deemed to be an hadronic event if:

- The event contains at least 5 TPC tracks, each satisfying the following:
  - the track must make an angle of $\theta > 18.2^o$ with respect to the beam pipe (this ensures the track traverses at least 6 pad rows in the TPC).
  - the track must have at least 4 reconstructed TPC coordinates associated with it.
  - The track must have a distance of closest approach to the measured interaction point of not more than $\pm$10cm along the beam direction and 2cm transverse to it.
- Assuming at least 5 good TPC tracks exist in the event, the total energy of these tracks should be more than 10% of the centre-of-mass energy.

Although not part of the standard event selection, it is normal to also check that each event contains no data acquisition error and that the ECAL, HCAL, ITC and TPC high voltages were in their correct state at the time.

## 5.3 Electron and Muon Identification

The technique of high $P_\perp$ lepton tagging has been widely used in the tagging of heavy flavour events therefore a standard lepton selection definition exists within the ALEPH collaboration which is defined in [1] and described in [15], [18], and [19].

As was mentioned earlier, few other processes produce high momentum leptons within hadronic showers. In the ALEPH detector a muon is required to have a momentum of at least 3GeV in order to traverse all the layers of the HCAL and register hits in the muon chambers. Consequently all lepton candidates are required to have $P >$ 3GeV. This also rejects most of the hadronic contamination. In addition, the standard hadronic event selection track cuts are tightened

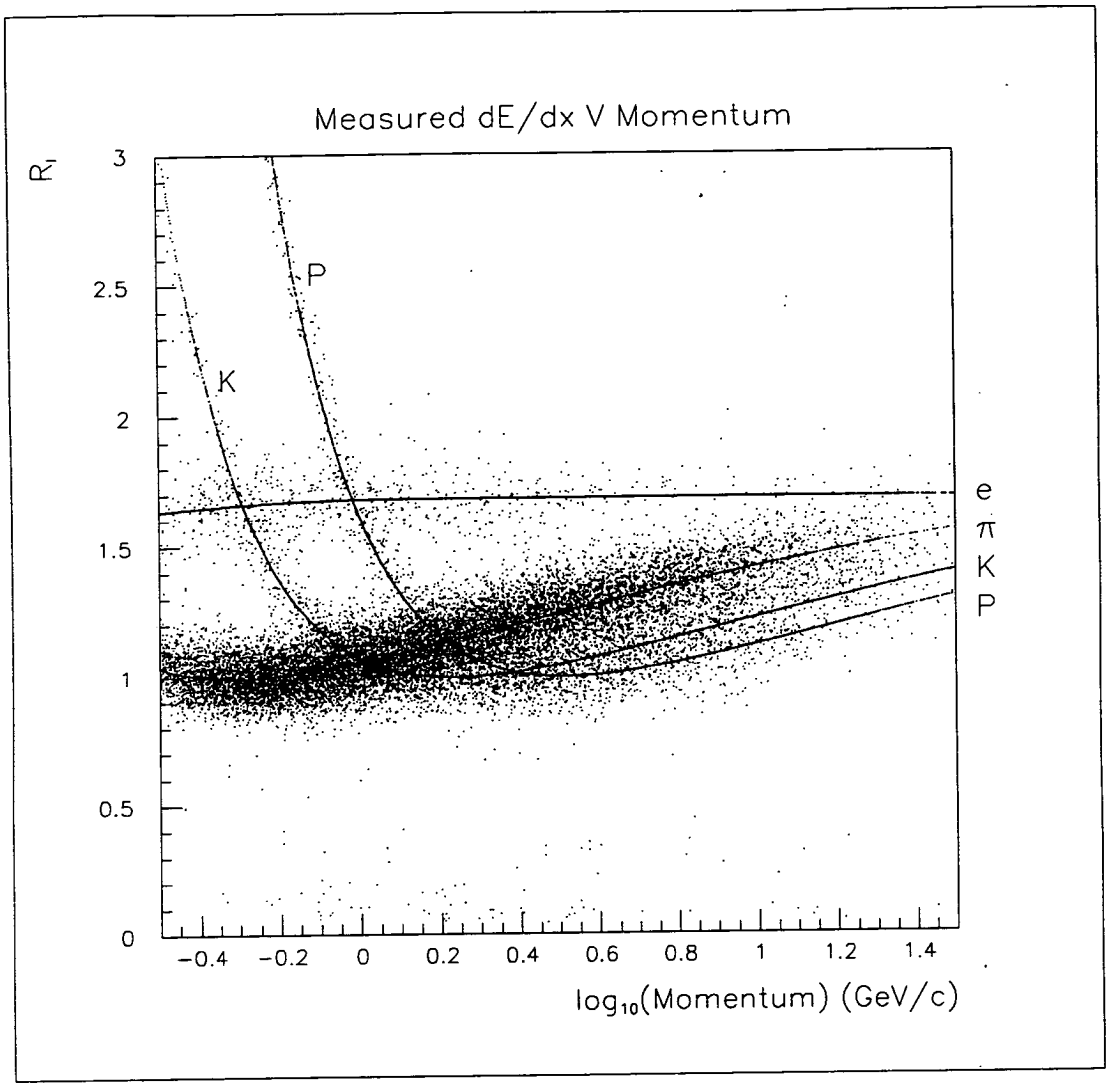


Figure 5.2: Measured and expected $dE/dx$ measurements for electrons, pions, kaons, and protons

by requiring that all candidate tracks have at least 5 good TPC coordinates and that their distance of closest approach transverse to the beam axis is less than 5mm.

### 5.3.1 Electron identification

The electron identification makes use of the TPC $dE/dx$ measurements and the shape of electromagnetic showers in the ECAL. Estimators are constructed from the measurements and cuts applied to select electron candidates. The TPC estimator is more effective at lower momenta while the ECAL estimators are more effective at higher momenta.

For each reconstructed track in the TPC the $dE/dx$ is measured only when more than 50 (of a possible 330) isolated wire hits can be associated with the track. Only the lower 60% of these measurements are used to avoid the large fluctuations of the Landau distribution. The $dE/dx$ response of the sub-detector has been carefully studied using ultra-relativistic Bhabha events to locate the ionisation plateau, whilst muons from $Z^0 \rightarrow \mu^+\mu^-$ and $Z^0 \rightarrow \tau^+\tau^-$ have been used to calibrate the relativistic rise. In addition, tracks from hadronic events (predominately leptons, pions, kaons and protons) have been used to parameterise the low momentum response. Figure 5.2 shows the measured $dE/dx$ versus particle momentum (normalised such that a $dE/dx$ measurement of 1 corresponds to a minimum ionising pion). The overlayed solid lines show the expected $dE/dx$ from the calibration described above. Using the measured and expected $dE/dx$ and the standard error on the expected value, the electron estimator given in Equation 5.1 has been defined.

$$R_I = \frac{dE/dx - < \frac{dE}{dx} >}{\sigma_{\frac{dE}{dx}}} \tag{5.1}$$

Given the hypothesis that the track in question is an electron, $R_I$ is required to be greater than -2.5. Its distribution is nearly gaussian and no upper limit is placed on the estimator as in the momentum regime considered, the electron has the highest value of $dE/dx$.

In addition to the TPC the ECAL is used to measure both the compactness and longitudinal shape of the electromagnetic shower generated by an incident candidate particle. The transverse shower size is measured as follows.

Each candidate track is extrapolated from the outside of the TPC through the ECAL to determine its crossing points between each of the 3 ECAL stacks. The four storeys in each stack closest to the extrapolated track are then found and the sum of the energy ($E_4$) deposited in them is found. The transverse shower estimator is defined as:

$$R_T = \frac{E_4/p - < \frac{E_4}{p} >}{\sigma_{\frac{E_4}{p}}} \tag{5.2}$$

where $E_4/p$ is the sum of the energy divided by the particle momentum as measured in the TPC, $< \frac{E_4}{p} >$ is the expected value of this ratio and $\sigma_{\frac{E_4}{p}}$ is the standard error on the expectation. Electromagnetic showers are considerably more compact than hadronic showers ($< \frac{E_4}{p} > \simeq 0.85$). Ensuring $R_T$ is greater than $-1.6$ maximises the hadron rejection whilst limiting the efficiency loss.

The longitudinal shower size of an electromagnetic shower is described by:

$$f(t) = \frac{1}{E_0}\frac{dE}{dt} = \frac{\beta^\alpha}{\Gamma(\alpha)} t^{\alpha-1} e^{-\beta t} \tag{5.3}$$

where $E_0$ is the particle energy, $t$ is the penetration depth in radiation length units, $\Gamma(\alpha)$ is the Euler function which normalises $f(t)$ and $\alpha$ and $\beta$ are free parameters. By fitting the shape of the electromagnetic shower in the ECAL to Equation 5.3 and hence extracting $\beta$ and $\alpha$ the longitudinal shower estimator $R_L$ can be found.

$$R_L = \frac{\beta/\alpha - < \frac{\beta}{\alpha} >}{\sigma_{\frac{\beta}{\alpha}}} \tag{5.4}$$

The validity of this estimator has been tested extensively with test beam data. Ensuring that $R_L$ is greater than $-1.8$ and less than 3.0 maximises hadron rejection and minimises efficiency loss. For tracks with momentum greater than 3GeV this estimator works well.

Figure 5.3 shows a scatter plot of $R_T$ versus $R_L$ measured from a sample known to have a large high $P_\perp$ lepton content. The well populated upper area is clearly separated from the lower hadronic area. Superimposed on the plot are the $R_T$ and $R_L$ cuts used. Figure 5.4 shows the variation of $R_I$ with momentum after the $R_T$ and $R_L$ cuts. Notice how nearly all the hadrons are already removed from the sample.

In addition to these cuts a further source of contamination arises from $e^+e^-$ pairs produced by pair production. Each candidate electron track is compared with every other charged track of opposite sign. The point in the $x-y$ plane where they are parallel and pass closest to each other is found. This point is known as the materialisation point. Any pair of tracks found to lie closer together than 1cm in the $x-y$ plane and 1cm in the $z$ direction with an invariant mass of less

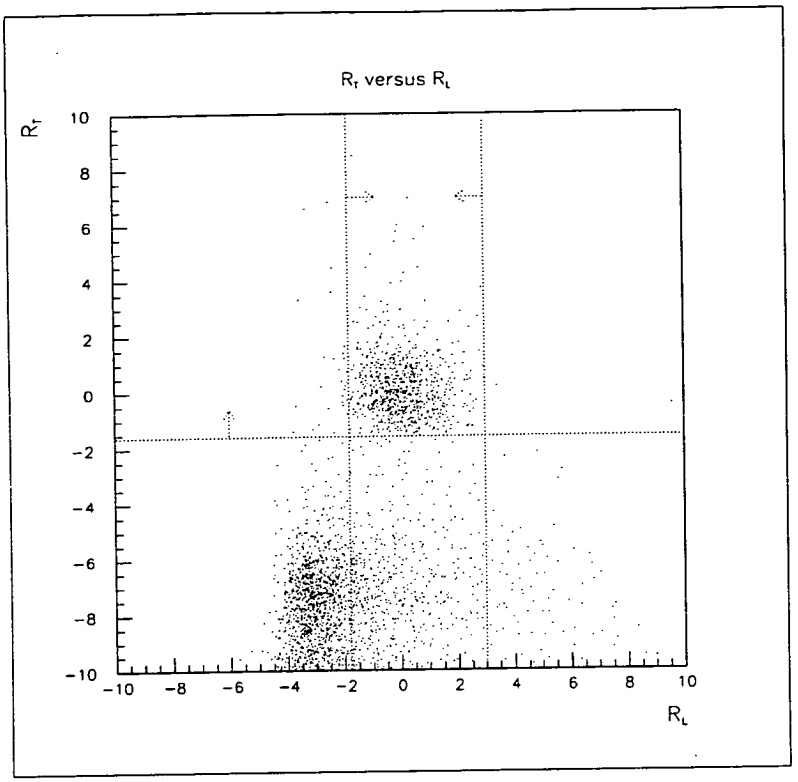


Figure 5.3: Distribution of $R_T$ versus $R_L$ with superimposed cuts

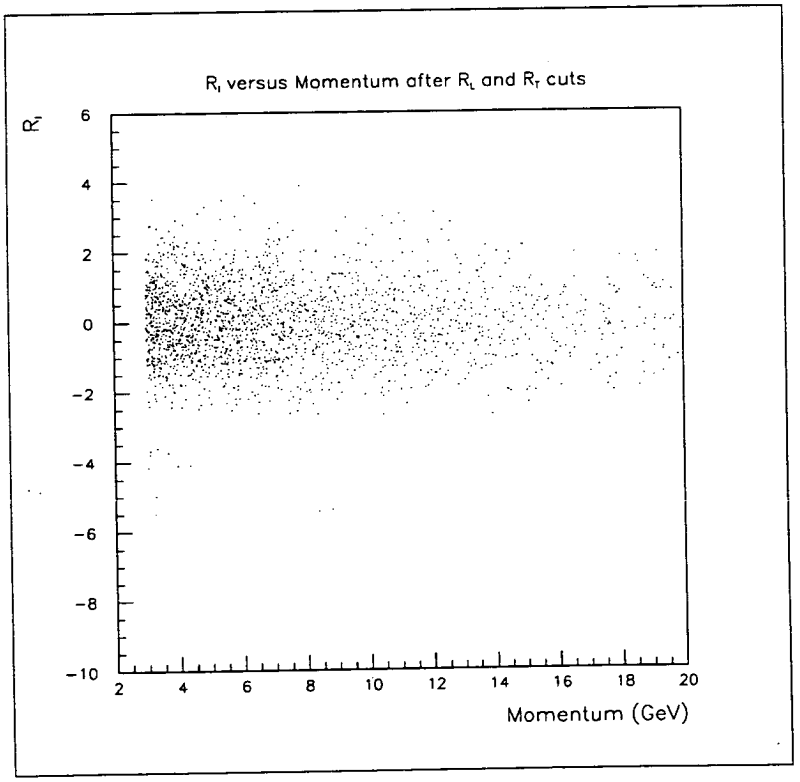


Figure 5.4: Distribution of $R_I$ versus momentum

than 20MeV are classed as originating from photon conversion and are excluded from the search. In practice this only effects ~1.7% of the candidate electrons.

### 5.3.2 Muon identification

The identification of muons relies upon the fact that they are the only detectable particles capable of traversing the iron layers of the HCAL, leaving behind a trail of "hits", and subsequently emerging to be detected by the muon chambers which surround ALEPH.

Each candidate track is extrapolated from the TPC, through the ECAL and coil, to the HCAL. A "road" is opened around the extrapolated track as it passes through the HCAL, the width of which corresponds to three times the standard deviation on the estimated extrapolation due to multiple scattering. An HCAL plane is said to be expected to fire if the extrapolated track intersects it within an active region. A hit is recorded if a streamer tube has fired within the road and no more than three adjacent tubes have also fired.

The cuts used to define a penetrating track which hasn't showered are given below:

- $N_{fir}/N_{exp} \geq 0.4$
- $N_{exp} \geq 10$
- $N_{10} > 4$

where $N_{fir}$ are the number of planes actually firing, $N_{exp}$ are the number of planes expected to fire, and $N_{10}$ are the number of firing planes within the last ten expected planes. In addition, $X_{mult}$ is computed by counting the number of digital hits and dividing by the total number of fired planes. $X_{mult}$ is required to be less than 1.5.

Each candidate track is further extrapolated through the two layers of muon chambers. A four standard deviation road is opened around the track and a muon chamber is defined to contain an associated hit if at least one of the streamer tubes in one of the layers has fired. At least one muon chamber hit is required.

## 5.4 Jet Creation and $P_\perp$ Calculation

Jets are created using the energy flow objects produced by the Janot energy flow algorithm described in Section 4.1. Because the method to find high $P_\perp$ leptons was designed some time before the popularisation of the DURHAM jet finding algorithm the JADE algorithm (see Section 4.2.1) is still used[3]. The value of $y_{cut}$ chosen has been optimised and is defined as

$$y_{cut} = \left(\frac{6.0}{E_{c.m.}}\right)^2 \tag{5.5}$$

which corresponds to a value of $\simeq$0.0044 at the $Z^0$ peak. This choice was made to optimise the purity versus efficiency curve of $b\bar{b}$ event selection.

Further cuts are also applied to the jets. Firstly, all jets must contain at least three energy flow objects. Secondly, the energy of an identified candidate electron or muon must be less than 90% of the total energy of the jet to which it belongs. These cuts reject jets which are basically just a single electron or muon. Finally, two or more good jets are required in an event.

Having identified a lepton and successfully associated it with a jet, its transverse momentum may be calculated. There are two possible methods for doing this which are defined in Equation 5.6 below.

$$\left.\begin{aligned} P_\perp^{inc} &= \frac{|\vec{P_{lept}} \times \vec{P_{jet}}|}{|\vec{P_{jet}}|} \\ P_\perp^{excl} &= \frac{|\vec{P_{lept}} \times (\vec{P_{jet}} - \vec{P_{lept}})|}{|\vec{P_{jet}} - \vec{P_{lept}}|} \end{aligned}\right\} \tag{5.6}$$

$P_\perp^{inc}$ is known as the inclusive $P_\perp$ and corresponds to the lepton $P_\perp$ measured with respect to the jet axis with the lepton included in the jet. Conversely $P_\perp^{excl}$, known as the exclusive $P_\perp$, is measured with respect to its jet with the lepton removed from the jet. There has been considerable debate [44] as to which of the definitions is superior. It is now generally accepted that the $P_\perp^{excl}$ definition

[3]Although the DURHAM algorithm was used for the majority of this analysis, high $P_\perp$ leptons were identified, and their $P_\perp$ calculated , using jets created with the JADE algorithm. These jets were subsequently discarded and took no further part in the analysis.

should be used and this analysis did so throughout.

## 5.5 LEPTAG

The procedures described above were developed over a long period of time by members of the heavy flavour lepton research group. When the lepton and jet definitions [1] were published, no standard collaboration software existed which implemented the procedure correctly. At around the same time (mid-1992) a small group of collaborators formed to produce a compact data set devoted to the study of $b$-quark physics. This data set was known as the btagDST [24] and this author was a primary contributor.

The btagDST project was motivated because at that time the Janot energy flow algorithm could only be executed if DST tapes were being studied. The amount of tape staging and CPU time required to do interesting $b$-physics analysis was proving prohibitive. The result of the project was a reduced size miniDST format data set suitable for heavy flavour analysis. It combined the storage of the energy flow objects with three $b$-tagging methods and the precalculation of general event and truth information. The three $b$-tagging methods were: an impact parameter tag (based on VDET information), an event shape tag, and a high $P_\perp$ lepton based tag. The LEPTAG package [48] , written by Mark Parsons and Ingrid ten Have, was designed to provide the high $P_\perp$ lepton tag information for the btagDST.

The usefulness of the btagDST encouraged many ALEPH collaborators to move their analyses to the miniDST format. Importantly, the Janot algorithm energy flow objects were soon stored on the standard miniDST. The btagDST therefore became obsolete and LEPTAG was modified for use with the miniDST outside the btagDST framework. LEPTAG is now used by many analyses within the collaboration. The package fully conforms to [1] and is designed to operate on a whole event, returning the results in the form of a BOS bank array. This bank is known as the "BMLT" bank. In addition to identifying high $P_\perp$ leptons, LEPTAG also calls the CALPOIDS package which provides lepton source prob-

abilities and Monte Carlo correction weights. The LEPDCY subroutine[4] is used to provide Monte Carlo truth information.

Figure 5.5 shows the program structure of LEPTAG. The subroutines are called from an ALPHA analysis job. At initialisation the counters are zeroed and the associated histograms (which are very useful for consistency checks) are booked. LEPTAG is called once for every event. On the first call the BOS bank format of the BMLT bank is defined. If a new run has just started the year of data taking is recalculated. A standard hadronic event selection is then performed followed by the selection of charged tracks which pass the more stringent track cuts. Any electrons, followed by any muons, passing the selection criteria described above are then identified. If no lepton candidates are found the routine exits.

Any lepton candidates are then associated with the jets to which they belong; the jets having been created before calling LEPTAG by the user. The jet selection cuts are then applied. If any leptons remain at this point they are now written to the BMLT bank, the format of which will be described shortly. During this process the inclusive and exclusive $P_\perp$ is calculated and, if Monte Carlo truth information is available, LEPDCY is called and its information stored. The CALPOIDS package is also called to provide lepton source probabilities and Monte Carlo data correction weights. These quantities being important for sensitive $b$-physics analyses. As they took no part in this analysis, no further comment shall be made. After filling the BMLT bank, the remaining histograms are filled and the routine ends. On program termination comprehensive execution statistics may be written out.

A great deal of effort has been expended to make sure LEPTAG is as robust and easy to use as is possible. Throughout its operation consistency checks are made and error conditions reported to the user (with text comments). It has been used extensively by many analyses within ALEPH and has recently been adopted as the standard lepton tag package for use in conjunction with the ultra-compact

[4]Version 4.x of LEPTAG replaces LEPDCY with calls to the superior FINLEP package. As this analysis was based on LEPTAG Version 3.21 it this version which will be described here.

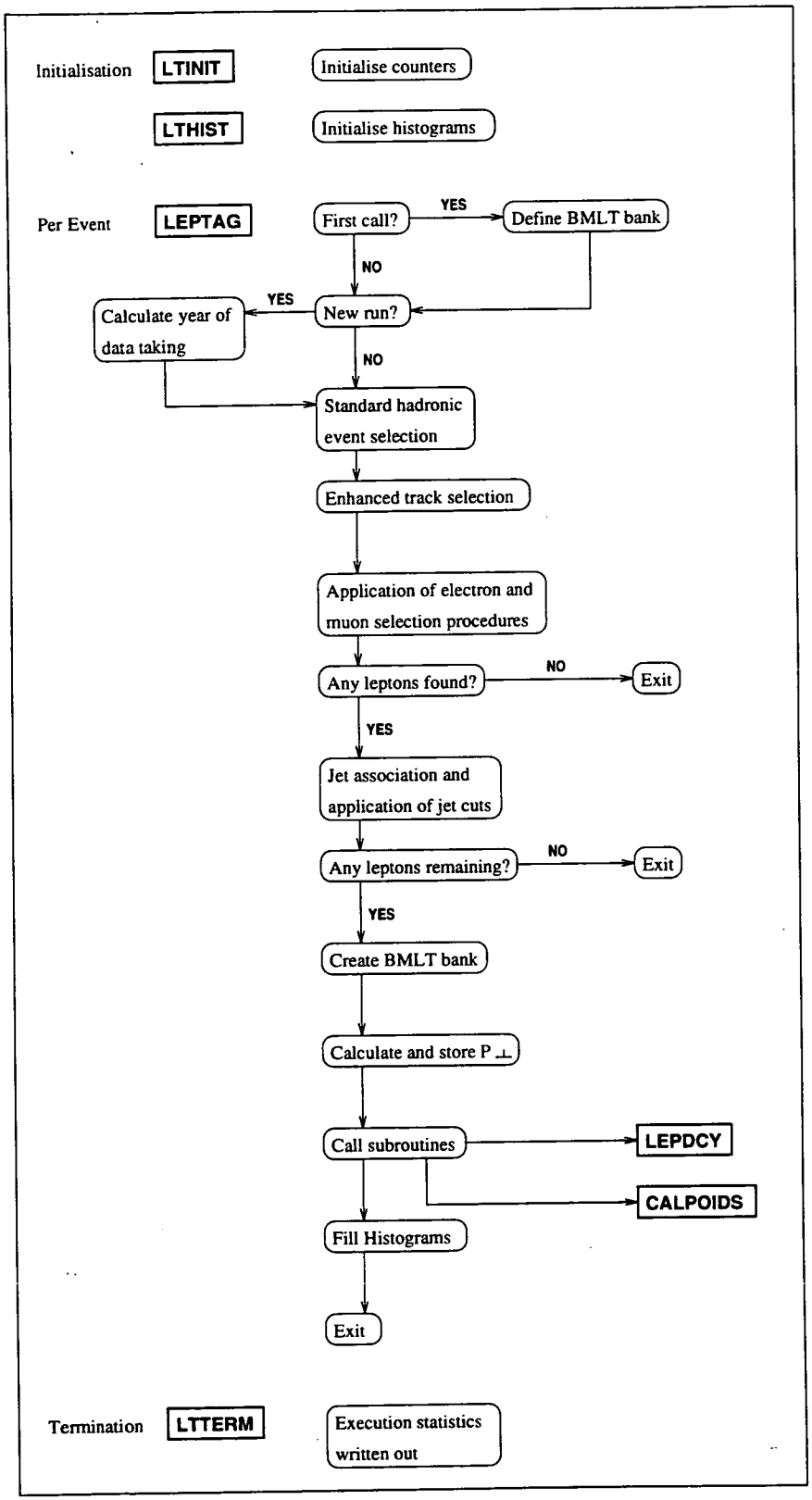


Figure 5.5: Program structure of the LEPTAG package

data format of the nanoDST.

The BMLT bank format is shown in Figure 5.6. Twenty integer words are used to store the information for each lepton. Any real values are multiplied by $10^6$ and integerised before storage to aid data compression (signified by "IF" in the bank format). The contents of the bank are relatively self-explanitory:

- Words 1-7: These words store the track identification, its type, $P_\perp^{inc}$ and $P_\perp^{excl}$, and the jet to which it belongs.
- Word 8: The Monte Carlo efficiency correction weight as returned by CALPOIDS.
- Words 9-16: The lepton source probabilities for 8 hypotheses as returned by CALPOIDS.
- Words 17-19: The Monte Carlo truth information as returned by LEPDCY.
- Word 20: The identification number of the lepton's corresponding energy flow track.

## 5.6 Quark Jet Tagging in 3-Jet Events

As has already been described, the DURHAM jet finding algorithm is used in this analysis to find hadronic events which contain three jets. If an event is found to contain three DURHAM jets a link is made to the BMLT bank. If the bank exists the number of identified electrons and/or muons is ascertained.

The charged track energy flow object corresponding to the charged track of each identified lepton is then found. The jet to which this energy flow object belongs is then identified. If more than one lepton is associated with a jet, the lepton with the highest $P_\perp^{excl}$ is retained. For a lepton to identify the jet as originating from the decay of a heavy quark, its $P_\perp^{excl}$ must be greater than 0.5GeV. The $P_\perp^{excl}$ used is that which was calculated using the JADE jets by LEPTAG and stored in word 5 of the BMLT bank.

Figure 5.7 shows the distribution of $P_\perp^{excl}$ for both identified electrons and muons. The recommended minimum value of $P_\perp^{excl}$ for use in $b$-physics analysis

```
*------*                                                    *------*
| BMLT |                                                    | BMLT |
*------*                                                    *------*
.....................................................................
          1       I    Number of words per lepton (=20)
          2       I    Number of leptons
.....................................................................
          1  TN   I    JULIA track number                      [1,*]
          2  PA   I    Particle type:                          [2,23]
                          2 => e+
                         12 => e+ in crack region
                         22 => e+ in overlap region
                          3 => e-
                         13 => e- in crack region
                         23 => e- in overlap region
                          5 => mu+
                          6 => mu-
          3  JT   I    Pointer to jet in jet section           [1,*]
          4  PI   IF   Transverse momentum                     [0,*]
                          lepton inclusive
          5  PE   IF   Transverse momentum                     [0,*]
                          lepton exclusive
          6  TR   I    IDF/Truth flag                          [1,*]
                          Bit 0: Muon IDF 13
                          Bit 1: Muon IDF 14
                          Bit 2: Genuine electron/
                                 positron
          7  MO   IF   Total momentum                          [0,*]
          8  LW   IF   MC efficiency correction weight         [*,*]
          9  W1   IF   Source weight: b -> l                   [*,*]
         10  W2   IF   Source weight: b -> tau -> l            [*,*]
         11  W3   IF   Source weight: b -> c   -> l            [*,*]
         12  W4   IF   Source weight: b -> W   -> c -> l       [*,*]
         13  W5   IF   Source weight: c -> l                   [*,*]
         14  W6   IF   Source weight: misid -> l (uds)         [*,*]
         15  W7   IF   Source weight: misid -> l (c)           [*,*]
         16  W8   IF   Source weight: misid -> l (b)           [*,*]
         17  DT   I    Decay type from LEPDCY                  [-1,6]
                        -1 => unknown decay type
                         0 => no associated MC track
                         1 => primary b
                         2 => secondary c
                         3 => primary c
                         4 => semileptonic tau decay
                         5 => non-prompt decay
                         6 => misidentified hadron
         18  DC   I    Decay category from LEPDCY              [0,5]
                          If decay type => 2
                            1 => b->c->l
                            2 => b->cbar->l
                          If decay type => 5
                            0 => none of the following
                            1 => gamma conversion
                            2 => b decay
                            3 => c decay
                            4 => tau decay
         19  LP   I    Code of the lepton parent               [0,367]
         20  ET   I    Energy flow object number               [1,*]
.....................................................................
```

Figure 5.6: The BMLT BOS bank format

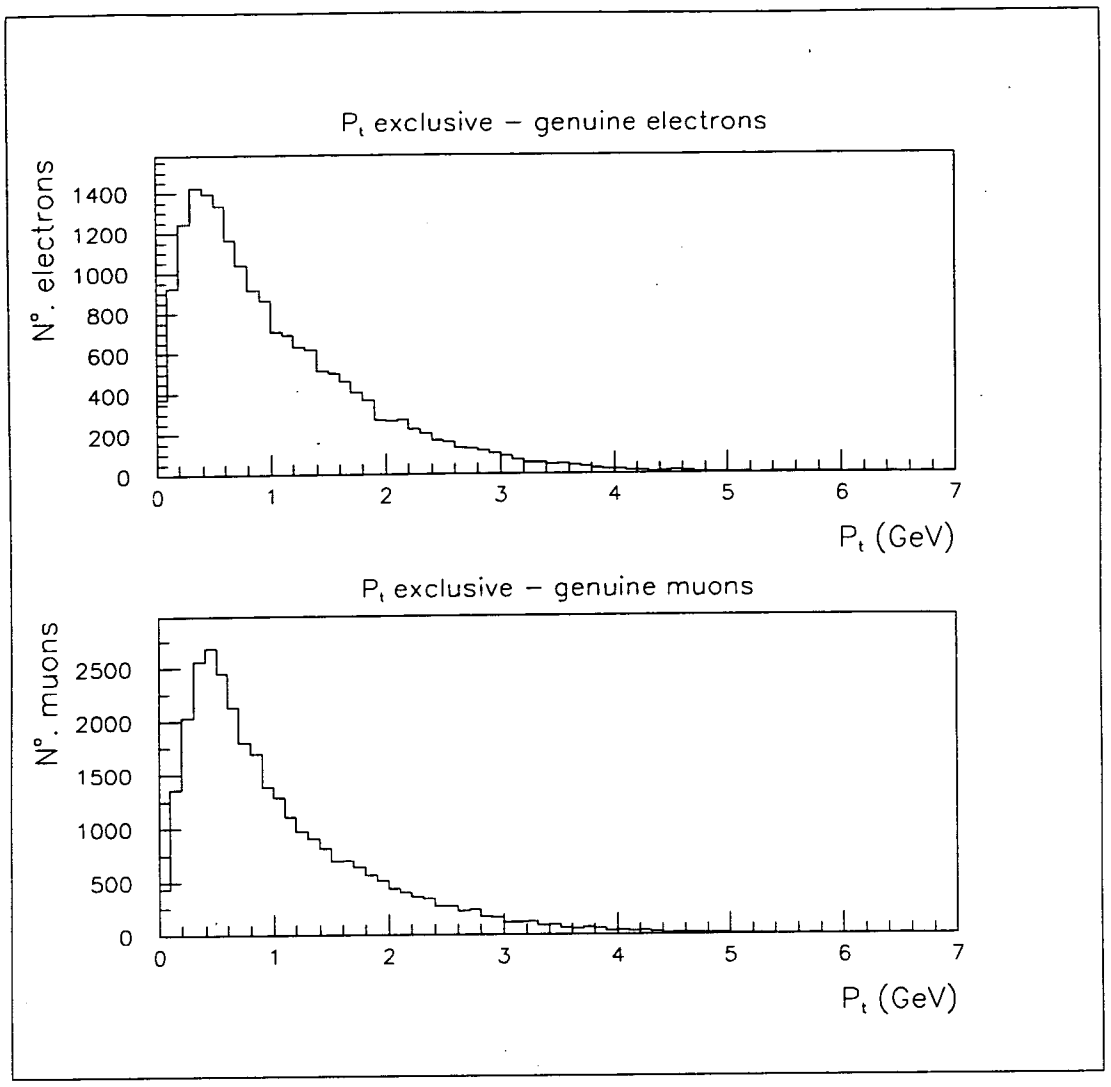


Figure 5.7: The distribution of $P_{\perp}^{excl}$ for identified electrons (upper plot) and identified muons (lower plot)

is $P_{\perp}^{excl} > 1.25$GeV. However, it is obvious that using a value as high as this would lead to low efficiency. As will be shown in the following two chapters, using a minimum value of 0.5GeV is a good choice for this analysis and leads to a good compromise between high $b$-quark jet purity and good efficiency.

# Chapter 6

# The Dalitz plot analysis

## 6.1 Introduction

The basic tools required for the analysis of 3-jet events have now been described and the following two chapters described their application. The general motivation behind the analyses have been discussed in Chapter 2 but the actual details of the measurements have been left until now.

For reasons which will be discussed later this analysis of 3-jet events came to be split into two separate analyses each sharing similar basic cuts but with methods devised specifically for the problems under study. The study described in this chapter investigated the angular distribution of quark jets in 3-jet events (the "Dalitz plot" analysis) by comparing data with Monte Carlo predictions. The second study, described in Chapter 7, analysed quark and gluon jet differences using a symmetric topological configuration in order to remove possible identification method biases.

## 6.2 The Dalitz plot

As was described in Chapter 2 the Born process $e^+e^- \rightarrow q\overline{q}$ is modified in first order QCD by the probability that one of the quarks radiates a hard gluon. Rather conveniently the cross section for this process can be described in terms

of the fractional energies of the two quarks and is given by:

$$\frac{1}{\sigma} \cdot \frac{d^2\sigma}{dx_1 dx_2} = \frac{2\alpha_s}{3\pi} \cdot \frac{x_1^2 + x_2^2}{(1-x_1)(1-x_2)}, \tag{6.1}$$

$$\text{where } x_1 = \frac{2E_q}{\sqrt{s}}, x_2 = \frac{2E_{\overline{q}}}{\sqrt{s}} \text{ and } x_3 = \frac{2E_g}{\sqrt{s}}$$

It therefore follows that $x_1 + x_2 + x_3 = 2$. The expression, written as it is above, is in its most familiar form and assumes massless partons. A corresponding equation exists for partons with non-negligible mass ($b$ and $c$-quarks for instance) but its general form is the same apart for corrections to account for the massive partons.

Any Monte Carlo program must generate a distribution of primary quark and gluon jets which conforms to the equation above. In addition to this, second and higher order effects must also be taken into account. The only reliable method therefore to analyze the Dalitz plot measurement extracted from real data is to compare it directly with the corresponding Monte Carlo generated distribution.

The general idea behind this analysis was to identify the quark jets in 3-jet events using high $P_\perp$ lepton tagging, to calculate $x_1$ and $x_2$, and bin these points in a two-dimensional plot of $x_1$ against $x_2$. The resulting distributions for both data and Monte Carlo could then be compared using some suitable statistical method and a statement made about their compatability.

### 6.2.1 Event selection

Any event selection method must be designed to bias the intended measurement as little as possible, and in as well an understood way as possible. In some respects any biases introduced in this analysis were not too important as the same selection technique was used for Monte Carlo and no corrections back to parton level using Monte Carlo information were attempted. Identical event selections were applied to data and Monte Carlo and are described below.

| | Data | | | | Monte Carlo |
|---|---|---|---|---|---|
| | 1990 | 1991 | 1992 | Total | (1992 geom) |
| Hadronic events | 112209 | 226375 | 659156 | 997740 | 993017 |
| Events with 3 jets | 35317 | 70605 | 205451 | 311373 | 332129 |
| 3-jets + > 1 lepton | 428 | 948 | 2681 | 4057 | 4214 |
| 3-jt + > 1 lpt + $P_\perp$ cut | 295 | 613 | 1721 | 2629 | 2642 |
| % total events | 0.26 | 0.27 | 0.26 | 0.26 | 0.27 |

Table 6.1: Number of events remaining after preselection

**Preselection**

The ALEPH miniDST data format was used as it was the most condensed data format found to contain all of the information required for this analysis including pre-calculated energy flow objects and pre-calculated electron and muon estimators. Whilst the miniDST is a fairly compact data format, one million Monte Carlo hadronic events still require ~42 two hundred megabyte tapes for storage. For this reason, and also for easy subsequent analysis, a preselection job was run which selected a small subset of events likely to be of analysis interest. The cuts applied at this stage were a subset of the cuts applied later on so that no event was excluded at the preselection stage which might later have passed the full set of analysis cuts. The preselection event cuts were as follows:

- The event had to pass the standard ALEPH hadronic event selection described in Section 5.2.
- The event had to contain two or more high $P_\perp$ leptons selected as described in the previous chapter.
- Of these high $P_\perp$ leptons at least two were required to have an exclusive $P_\perp$ of 0.5GeV or more.
- The energy flow objects in the event were required to cluster to three jets using the DURHAM algorithm with the E-scheme and a $y_{cut}$ of 0.01.

Table 6.1 shows how the preselection dramatically reduced the size of the event samples. The initial hadronic event data sets were selected using the ALEPH event database program "SCANBOOK". Stored in this database are

the physical location and type of all the official ALEPH data sets. The selection criteria used to select the real data was that data recorded in 1990, 1991, and 1992 would be analysed and that "on-peak" events would be used. "On-peak" events are those events which were recorded when the centre-of-mass energy of LEP was $91.2 \pm 0.1$GeV (the $Z^0$ peak). The small quantity of data recorded in the initial 1989 data taking period is no longer considered to be good data by the collaboration. This is due to the large number of hardware and software problems associated with the startup of an experiment as complex as ALEPH. The data recorded during 1993 was not used as it has only recently been finally reprocessed into a form suitable for confident analysis. In addition to these selection criteria, four components of the detector were required to have been passed as suitable for "heavy flavour" analysis. These four components being the $dE/dx$, the ECAL, the HCAL, and the muon chambers (in SCANBOOK parlance HD.AND.HE.AND.HH.AND.HM events were selected).

The creation of large quantities of fully reconstructed Monte Carlo is an extremely CPU, storage, and labour intensive operation. For these reasons only one large fully reconstructed Monte Carlo data set is available for analysis within ALEPH, and this is based on the JETSET 7.3 parton shower generator which was described in Chapter 2. The most recent production (based on the 1992 description of the experimental geometry of ALEPH) consists of $\sim$2 million hadronic events. A subset of these events, approximately equal in number to those of the real data sample, were used.

### Full event selection

The data sets produced using the preselection process proved ideal for quick repeated analysis (it was possible to store the data sets on disk rather than tape). During full analysis the above cuts were applied and in addition:

- The axis of each jet in an event was required to be at least $30^o$ from the beam pipe.
- The *measured* energy of each jet was required to be greater than 5GeV.

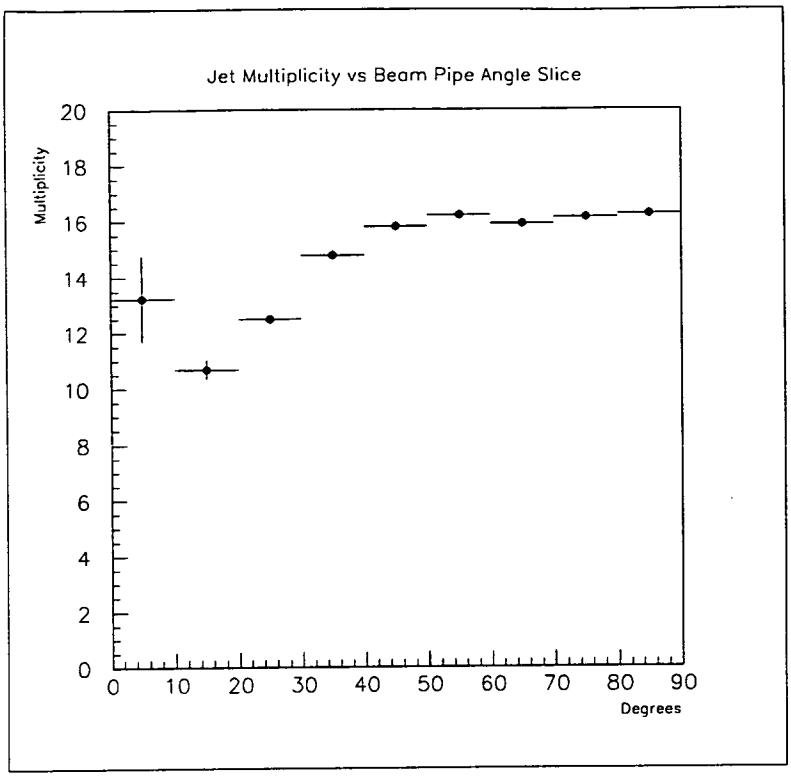


Figure 6.1: Monte Carlo charged and neutral multiplicity per jet as a function of distance from the beam pipe

These cuts require some explanation.

A jet formed using a clustering algorithm such as DURHAM will have a poorly determined jet axis if some of the true constituents of that jet have been lost by passing through the detector's insensitive volume along the direction of the beam pipe. The insensitive volume caused by the presence of the beam pipe covers the region $0.95 \leq |\cos(\theta)| \leq 1.0$. In addition to the possibility of a poor directional determination, a jet formed in this way is of little use if its constituents are to be studied (since many of them may not have been detected). The 30° beam pipe cut was chosen to remove as much of this effect as was practicable whilst retaining a large enough fraction of the events for analysis. Figure 6.1 shows the results of the Monte Carlo analysis of the problem. All final state Monte Carlo truth information was used except for those particles with $|\cos\theta| \geq 0.95$. Jets were formed and the multiplicity of each jet in an event was measured. These measurements were binned as a function of the angle which the jet axis made with the beam pipe. The chosen cut is shown to remove the majority of the

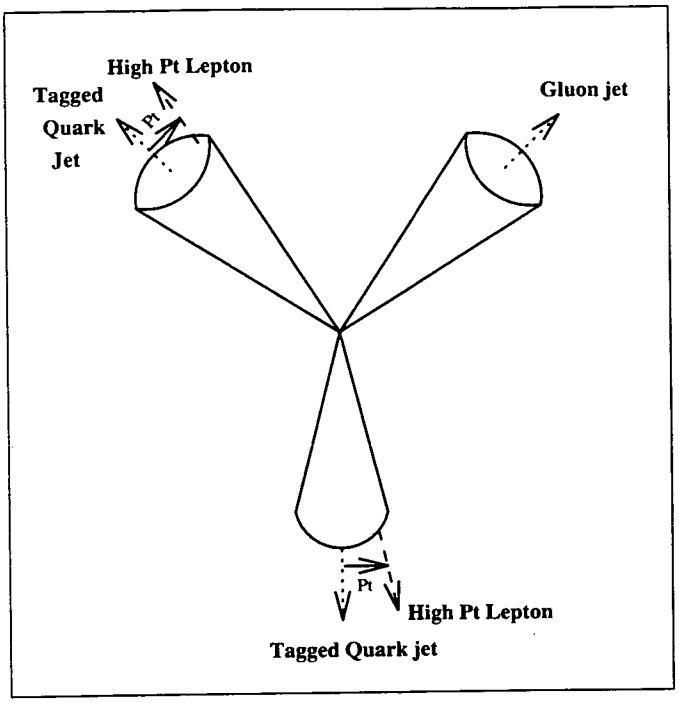


Figure 6.2: Schematic representation of the method used to tag the quark jets in 3-jet events

effect.

The second cut was included because it was felt that any jet with measured energy of less than 5GeV was likely to be poorly formed and of little interest to the analysis. The number of events this cut removed was very small and therefore no large study was made of it.

The numbers of events remaining after these cuts is given in the next section.

### 6.2.2 Event tagging and purity calculation

The quark jet candidates in each 3-jet event were identified as shown in Figure 6.2. Subsequent to jet clustering the high $P_\perp$ leptons in the event were each associated with the jet to which their corresponding energy flow object had been assigned. Only those high $P_\perp$ leptons with $P_\perp > 0.5$GeV were considered. For an event to have been correctly tagged, two of the three jets were required to contain associated high $P_\perp$ leptons whilst the third jet was required not to contain a high $P_\perp$ lepton. The two jets containing the high $P_\perp$ leptons were identified as quark jets whilst the third jet was identified as a gluon jet by default. Figure 6.3

| | Data 1990+1991+1992 | | Monte Carlo 1992 geometry | |
|---|---|---|---|---|
| | Failed | Total | Failed | Total |
| Preselected events | - | 2629 | - | 2642 |
| Beam pipe cut | 631 | 1998 | 697 | 1945 |
| Tagged | 563 | 1435 | 523 | 1422 |
| Measured energy cut | 5 | 1430 | 1 | 1421 |
| Failed event plane | 4 | 1426 | 3 | 1418 |
| Total selected events | - | 1426 | - | 1418 |

Table 6.2: Final numbers of events suitable for study

shows an example of a 3-jet event tagged in this way. Two of the three well defined jets are identified as quark jets by the presence in each of a high $P_\perp$ muon. The muons are clearly visible as they are the only particles passing through the hadron calorimeter, leaving behind a trail of hits, and registering signals in both layers of the muon chambers.

The reduction in number of events from the preselected samples is as shown in Table 6.2. Note how the beam pipe cut and tagging requirements remove a fairly large number of events as expected, whilst the cut on minimum measured energy proves insignificant. For technical reasons related to the calculation of the event plane, a small number of events were not studied because it was not possible to calculate the energy of their jets. These events are classed as "failed event plane" in the table.

The requirement that each event contain two high $P_\perp$ leptons results in a flavour composition for the tagged Monte Carlo sample as detailed in Table 6.3. The flavour composition was determined directly from the Monte Carlo truth information for all events in the selected sample. As would be expected the sample consists predominately of $b\bar{b}$ events with the bulk of the remainder being $c\bar{c}$.

The purpose of the tagging method is to select as purely as possible the two quark jets in the 3-jet events. To assess the purity the methods described in Chapter 4 were used. On tagging a 3-jet Monte Carlo event at the detector level, the pre-hadronisation particles at the parton level were clustered to 3-jets as described previously. The parton jets corresponding to the primary quark,

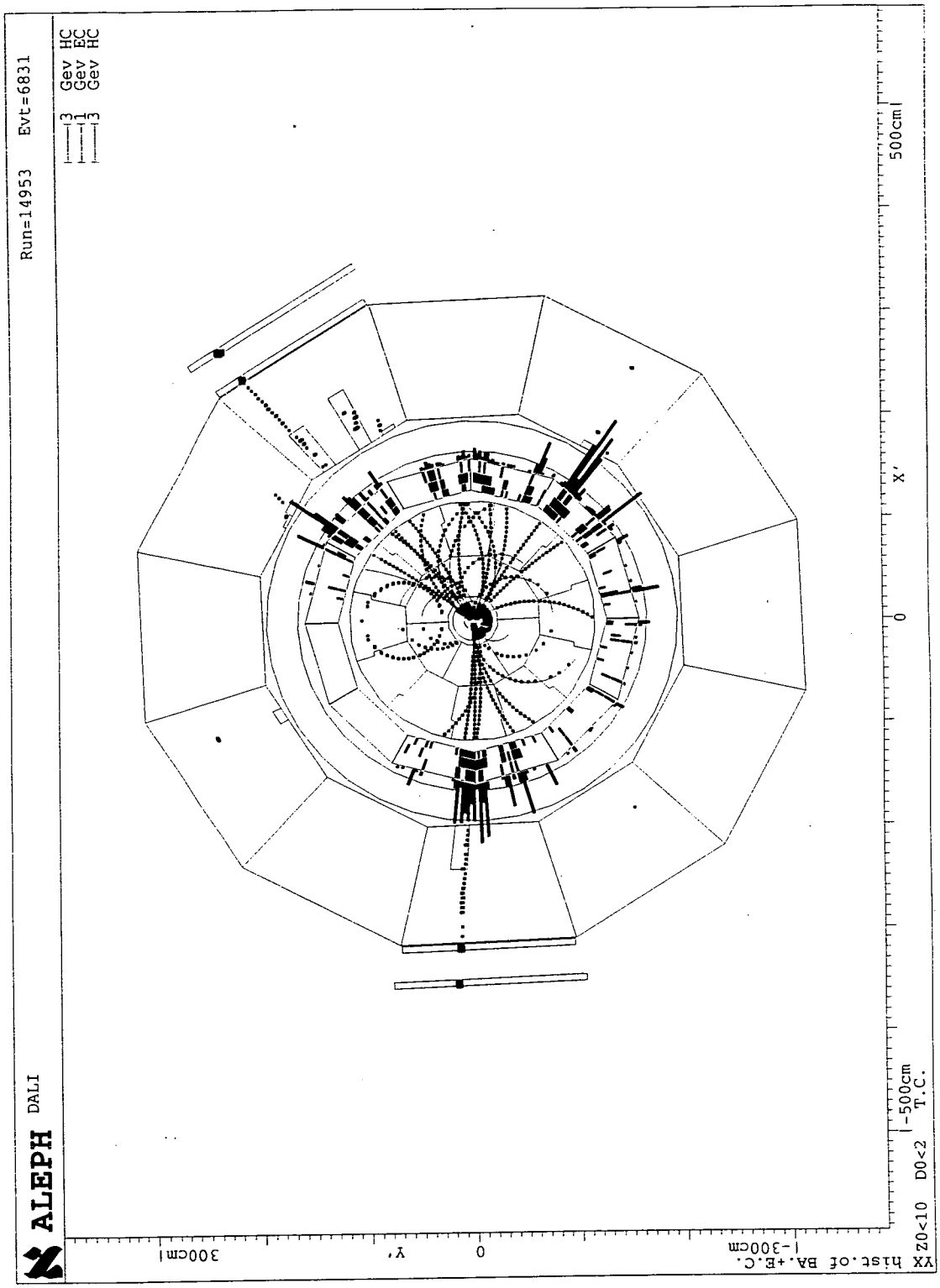


Figure 6.3: A 3-jet event with both quark jets identified using high $P_\perp$ muons the remaining jet is identified as the gluon jet

| Flavour | Events | % |
|---|---|---|
| $u\bar{u}$ | 7 | 0.5 |
| $d\bar{d}$ | 11 | 0.8 |
| $s\bar{s}$ | 4 | 0.3 |
| $c\bar{c}$ | 144 | 10.2 |
| $b\bar{b}$ | 1252 | 88.3 |

Table 6.3: Flavour composition of the selected sample

anti-quark, and gluon were identified. Using angular matching the detector level jets were then matched to the parton level. If the detector level jets to which the quark jets were matched each contained a high $P_\perp$ lepton then the event was classed as having been tagged correctly. If one of the parton level quark jets was matched to the detector level gluon jet then the event was classed as incorrectly tagged.

Two cases of ambiguity arise:

1. It is occasionally the case that during the identification stage of the parton jet creation both primary quarks are contained in one jet. An event of this type is obviously ambiguous.

2. After matching to another level (in this case the detector level) the maximum matching angle $\theta_{max}$ discussed in Section 4.3.4 can be large in a small number of cases. An arbitrary cut-off of $40^o$ is applied to the value of $\theta_{max}$. Any matched event with $\theta_{max}$ greater than this value is classed as ambiguous.

Figure 6.4 shows the distribution of $\theta_{max}$. Note that the vertical scale is logarithmic and that the vast majority of events are found well below $\theta_{max} = 40^o$. If an event was classed as ambiguous no attempt was made to calculate whether or not the detector level jets were correctly identified. The purity of the event sample was calculated using:

$$Purity = \frac{C + (A/2)}{C + W + A} \tag{6.2}$$

where $C$ is the number of events tagged correctly, W is the number of events tagged incorrectly, and A is the number of ambiguous events with no purity

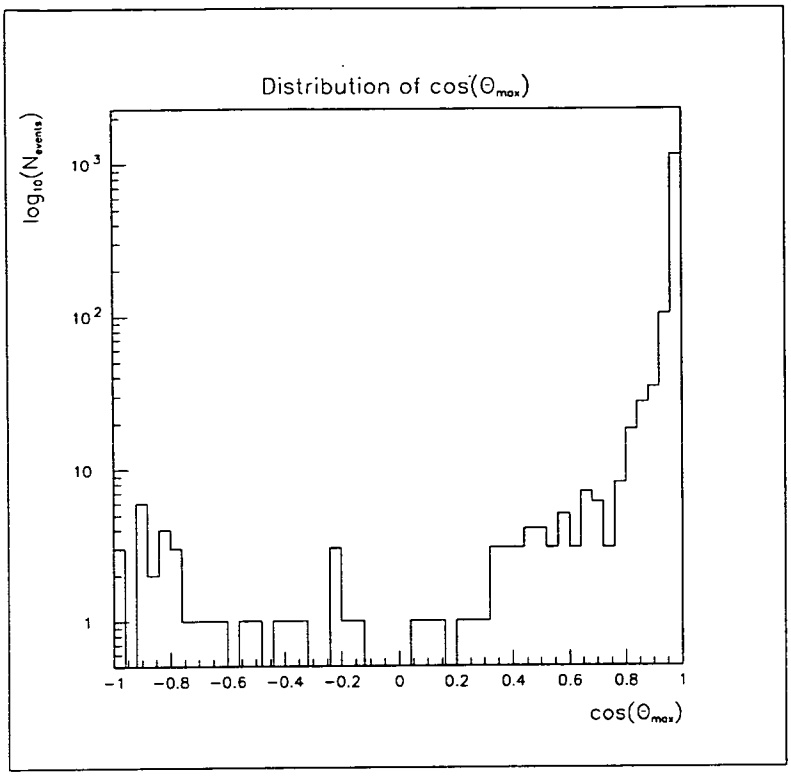


Figure 6.4: The distribution of $\theta_{max}$ for all selected events

information (and is small). The $(A/2)$ term has been the subject of some debate. If it is believed that all of the ambiguous events are in fact correctly tagged then the numerator of equation 6.2 should be $C + A$. Conversely, if it is believed that all of the ambiguous events are incorrectly tagged then the numerator should just be $C$. As no information is available to measure the purity of the ambiguous sample the measured value is quoted with a systematic error found by repeating the purity calculation first with the numerator set to $C + A$ and then to $C$. Since the purity is a binomial distribution (an event is either correctly or incorrectly tagged) the statistical error is given by:

$$\delta P_{stat} = \sqrt{\frac{Purity \times (1 - Purity)}{N_{events}}} \tag{6.3}$$

The values used to calculate the purity are given in Table 6.4. Note how the percentage of ambiguous events due to badly formed parton level jets is low, with the main ambiguity arising from the $\theta_{max}$ cut. Also included in the table are the number of events for which the two lower jet pairs were swapped as described in

| | N°. affected | N°. remaining |
|---|---|---|
| Selected | - | 1418 |
| Bad parton jets | 2 | 1416 |
| Jet match swapped | 1 | 1416 |
| $\theta_{max} > 40^o$ | 82 | 1334 |
| | Event composition | |
| Correct tag | | 1171 |
| Wrong tag | 1334-1171 = | 163 |
| Ambiguous tag | 2+82 = | 84 |

Table 6.4: Numbers used in the purity calculation

Section 4.3.4. This number is small as previously mentioned. The final purity determination is therefore:

$$\left.\begin{aligned} Purity &= \frac{1171 + 84/2}{1418} &&= 0.86 \\ \delta P_{stat} &= \sqrt{\frac{0.86 \times (1 - 0.86)}{1334}} &&= 0.01 \\ \delta P_{syst} &= +(P_{max} - P), -(P - P_{min}) &&= \\ & \quad +(0.89 - 0.86), -(0.86 - 0.83) &&= \pm 0.03 \\ \text{and finally } Purity &= (86 \pm 1 \pm 3)\% \end{aligned}\right\} \quad (6.4)$$

At first glance the value arrived at for the purity measurement may seem somewhat disappointing. However, considering the difficulty of the problem under study a final impurity of ~14% in the tagged sample is remarkably good. There are many sources for this impurity.

Of those events found to be tagged correctly, 90% of the leptons originated from either primary $b$, or primary or secondary $c$ decay. Of the remaining 10%, 60% of these were mis-identified hadrons. However, only 44% of the badly tagged events contained leptons originating from primary $b$, or primary or secondary $c$. Most of the remaining 56% were found to be mis-identified hadrons. Applying a harder $P_\perp$ cut would have increased the $b$ purity of the event sample but would not have reduced the number of mis-identified hadrons by any larger amount. It would also have had the effect of greatly reducing statistics which was viewed as much more detrimental to the study than some gluon jet impurity.

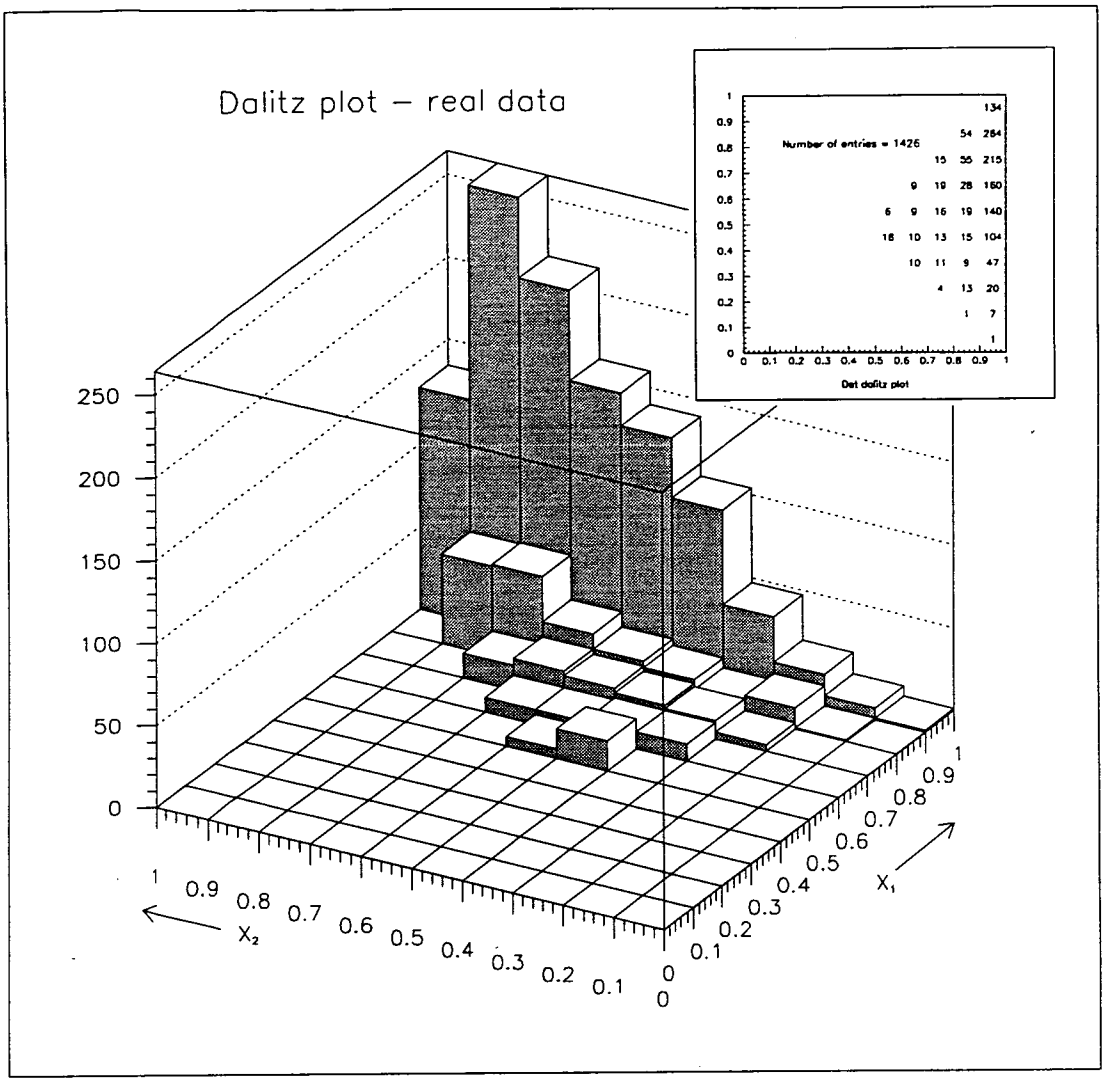


Figure 6.5: Dalitz plot distribution for the real data sample

The purpose of this study was to check that the Monte Carlo correctly modelled the data; therefore, no correction for impurity was attempted in order to avoid biasing the measured data towards the Monte Carlo. In any case it is not obvious how such a correction would be applied.

### 6.2.3 Dalitz plot comparison

The Dalitz plot distributions for real data and Monte Carlo are shown in Figures 6.5 and 6.6. Because no information is available to unambiguously identify which jet is the quark and which the anti-quark the values of $x_1$ and $x_2$ are always ordered in such a way that $x_1 \geq x_2$. Although the number of populated

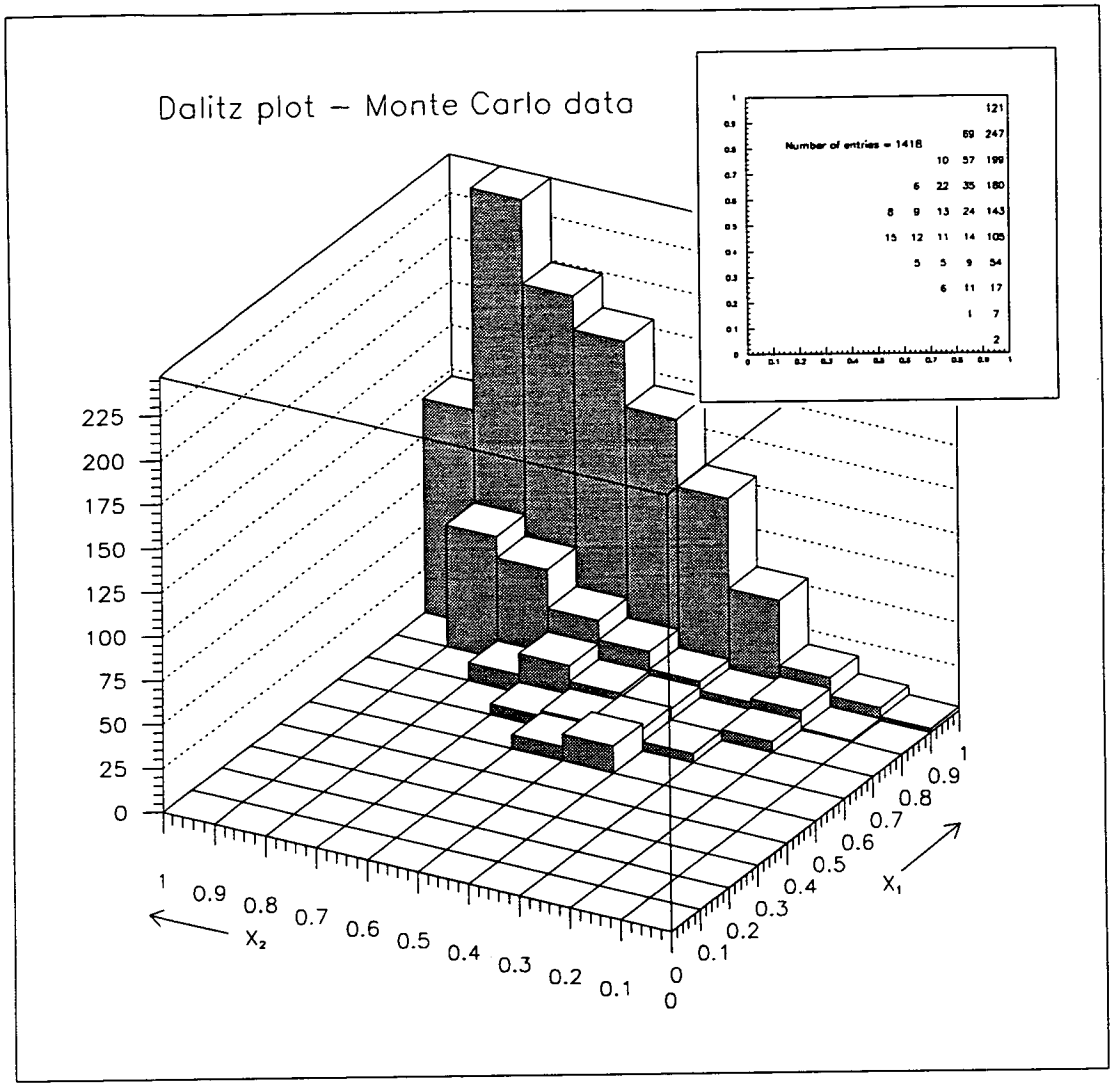


Figure 6.6: Dalitz plot distribution for the Monte Carlo data sample

bins is halved because of this, no information is lost from the distribution and any biases due to the analysis software always selecting a certain type of jet first are removed. The calculated energy of the jets was used to determine $x_1$ and $x_2$. It is immediately obvious that the distributions are very similar and to evaluate this statistically a custom designed statistical test was used. This test was designed such that equivalent bins from the two histograms could be compared with each other to see if their contents (given the total number of entries in each histogram) were compatible within statistical error. By summing the compatibility measurements, a measure of the overall compatibility of the two histograms was derived.

A suitable choice for such a test is not immediately obvious. A $\chi^2$ based test

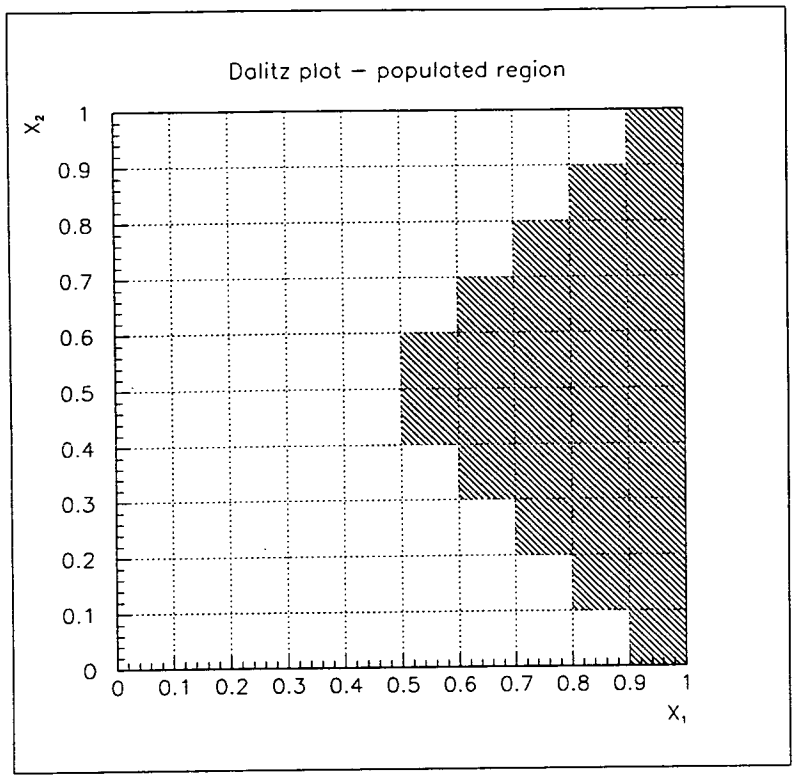


Figure 6.7: Hatched area indicating region of the Dalitz plot which was studied

was not suitable as, for the result to be meaningful, neither distribution may have poorly populated bins.

A log-likelihood test was finally chosen and its derivation[1] is given in Appendix A. From a theoretical standpoint the use of the log-likelihood method is far superior to the $\chi^2$ method as it is not affected by poorly populated bins and can be used to compare two distributions with roughly the same number of entries. The test is shown below in the same notation as is used in Appendix A.

$$\ln L_0 - \ln L_1 = \sum_{i=1}^{N} \left[ d_i \ln \frac{d_i(D+M)}{(d_i+m_i)D} + m_i \ln \frac{m_i(D+M)}{(d_i+m_i)M} \right] \qquad (6.5)$$

$d_i$ and $m_i$ are the number of entries in the $i^{th}$ bin of the real and Monte Carlo distributions respectively, $D = \sum_{i=1}^{N} d_i$ and $M = \sum_{i=1}^{N} m_i$.

It was obviously only interesting to study those bins which were populated and Figure 6.7 shows the actual area on the Dalitz plot which was studied. This area corresponds to 30 histogram bins and is the area expected to be filled

[1]The author thanks Dr D. Candlin for this derivation.

kinematically. Of course some of the bins may not contain any entries and the equation as written is undefined. However it is easily shown that if one of the bins contains zero entries then the undefined term may be set to zero.

In order to understand the result returned by applying the test to the two distributions a study was made of the test. It proceeded as follows:

- The distribution measured from real data was used to generate random numbers according to its shape. Specifically, the HISRAN package [39] was used to generate random numbers according to the cumulative probability distribution constructed from the initial histogram.

- Two randomly generated histograms containing 30 bins with the same general shape as the real data distribution were then populated with the same number of entries as the real and Monte Carlo histograms (1426 and 1418 respectively).

- The two generated histograms were then compared using the log-likelihood test and the result entered into a histogram.

- The previous two steps were then repeated 10000 times until the histogram shown in Figure 6.8 was filled as shown.

As is discussed in Appendix A, in the case where $D = M$, $d_i \gg 0$ and $m_i \gg 0$ then the test approximates to a "$\chi^2$"/2 test which implies the distribution mean should be equal to half the number of bins. This is indeed true with the exact value being $14.95 \pm 0.04$.

Having found how the log-likelihood test behaved, the resulting histogram shown in Figure 6.8 was used to state a confidence level that the two distributions for which $\ln L_0 - \ln L_1$ had been calculated agreed with each other to within a statistical error of the order of $1\sigma$. By summing the number of entries in the histogram from the measurement to infinity and dividing the result by the total number of entries, the confidence level was obtained. This is expressed in Equation 6.6 where $N$ is the total number of entries, $n_i$ is the number of entries

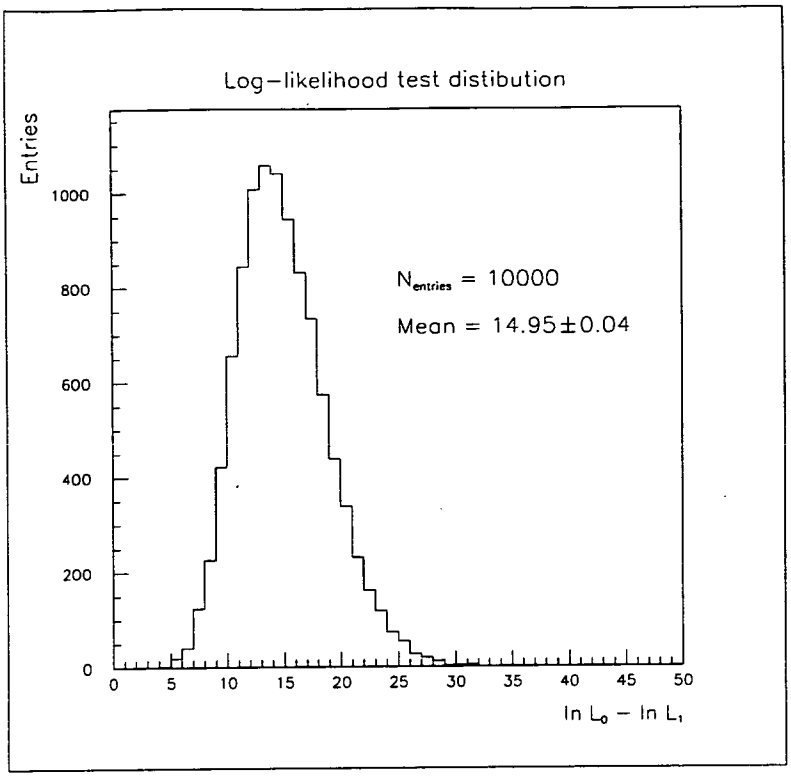


Figure 6.8: Distribution resulting from the application of the log-likelihood test on pairs of randomly generated distributions

in the $i^{th}$ bin and $L$ is the measured log-likelihood value of $\ln L_0 - \ln L_1$.

$$\text{Confidence level} = \frac{\sum_{i=L}^{\infty} n_i}{N} \tag{6.6}$$

Applying the log-likelihood test to the real data and Monte Carlo data distributions the result below is obtained:

$$\ln L_0 - \ln L_1 = 7.5 \tag{6.7}$$

The result indicates that the two distributions are extremely compatible with each other. Indeed, if the confidence level that the two distributions agree with each to within statistical error is calculated, a value of

$$C.L. = 97\% \tag{6.8}$$

is found. It should be noted that, while a confidence level as high as is quoted

above is an extremely encouraging result, had the measured point been found at the peak of Figure 6.8 then a confidence level of only ~50% would have resulted. However, this result would have been equally as welcome as the actual measured result. Only if the measured log-likelihood value was obviously to the right of the peak of Figure 6.8 would it have been possible to make any strong statement about the lack of compatibility of the two distributions.

### Monte Carlo model predictions

To try and understand what possible theoretical descriptions of the fundamental interactions involved in generating the Dalitz plot distribution would be disfavoured, given a positive agreement between real data and the JETSET parton shower Monte Carlo, a study was made of some alternative Monte Carlo models.

The generation of large amounts of fully reconstructed Monte Carlo data was not practicable. As the standard ALEPH JETSET 7.3 parton shower Monte Carlo had been shown to agree well with data, a quantity of generator events (events not subject to the detector simulation program) were produced as a benchmark sample for comparison with the other models. Since the real data consisted predominately of $b\overline{b}$ events it was decided to configure the models to generate $b$ flavour events exclusively.

Generating 10000 events for each model data set was found to result in ~2000 3-jet events which is of the same order as the number of real data events. The Dalitz plot distribution for each model data set was constructed as follows:

- 10000 Monte Carlo generator level events were produced.
- All the hadron level particles were clustered using the DURHAM algorithm with the E-scheme and a $y_{cut}$ of 0.01.
- If the event was found to contain three jets at the hadron level, three parton level jets were constructed and their type identified as was described in Section 4.3.3.
- The hadron level jets were matched using angular matching to the parton level jets. The jet classification of the parton level jet was used to identify

the type of hadron level jet (the event sample was by default 100% pure).

- The two "tagged" quark jets at the hadron level were then used to find $x_1$ and $x_2$ (when binned in the histogram $x_1$ and $x_2$ were then ordered such that $x_1 \geq x_2$) before being entered into the Dalitz plot.

Having found the Dalitz plots for each model these were then compared, using the log-likelihood test, to the benchmark sample. The actual models used are given in Table 6.5 along with all the relevant parameters which were tuned to ALEPH data. These parameters were obtained from three sources [17], [25], and [26].

The properties of each model were chosen in the hope that one or more of the models would generate a 3-jet distribution of significant difference to that of the benchmark sample and confirm that the method used to compare the real data with Monte Carlo would have shown this difference had it existed. The results for each model plus a description of that model are given below:

- **Parton shower incoherent:** In this model the angular ordering of the radiated gluons in the shower has been turned off. It was hoped that this might induce differences in the angular distribution of the jets; however, the measured value of $\ln L_0 - \ln L_1 = 13.7$ implies any differences have cancelled overall or are unimportant and the main analysis would have been an insensitive test of this difference.

- **$2^{nd}$ order matrix element:** As has been explained in Chapter 2 the parton shower model is not the only valid approach to modelling perturbative QCD. At lower energies merely calculating the $1^{st}$ and $2^{nd}$ order matrix elements and fragmenting the resulting configurations using a well tuned fragmentation function provided a good description of the final events. At higher energies higher order hard QCD emission becomes increasingly important and no matter how well the fragmentation function is tuned the resulting events will not describe reality as well as expected. Unfortunately this is not apparent from the result of $\ln L_0 - \ln L_1 = 18.9$.

| Base MC | Model | Parameters |
|---|---|---|
| JETSET 7.3 | Parton shower benchmark | Standard ALEPH HVFL03 tune |
| JETSET 7.3 | Parton shower incoherent | Standard ALEPH HVFL03 tune except<br>MSTJ(42) = 1 (no angular ordering)<br>MSTJ(44) = 1 (running $Q^2 = m^2/4$)<br>PARJ(81) = 0.38 ($\Lambda$)<br>PARJ(82) = 1.59 ($M_{min}$)<br>PARJ(21) = 0.414 ($\sigma_{P_\perp}$)<br>PARJ(41) = 0.5 (fragmentation function 'a')<br>PARJ(42) = 1.23 (fragmentation function 'B') |
| JETSET 7.3 | Matrix element $2^{nd} order$ | Standard ALEPH HVFL03 tune except<br>MSTJ(101) = 2 ($2^{nd}$ order QCD ME)<br>MSTJ(108) = 2 ($2^{nd}$ order calc of $\alpha_s$)<br>MSTJ(110) = 2 (ERT matrix elements)<br>MSTJ(111) = 1 (optimised scale)<br>PARJ(122) = 0.140 ($\Lambda_{\overline{MS}}$)<br>PARJ(129) = 0.00136 (scale parameter f)<br>PARJ(125) = 0.01 ($y_{min}$)<br>PARJ(21) = 0.44 ($\sigma_{P_\perp}$)<br>PARJ(41) = 1.0 (fragmentation function 'a')<br>PARJ(42) = 0.496 (fragmentation function 'B') |
| JETSET 7.3 | Matrix element scalar gluon | Standard ALEPH HVFL03 tune except<br>MSTJ(109) = 1 (scalar gluon switch)<br>MSTJ(101) = 1 ($1^{st}$ order matrix elements)<br>MSTJ(108) = 0 (fixed value of $\alpha_s$)<br>PARU(111) = 1.7 ($\alpha_s$)<br>PARJ(21) = 0.44 ($\sigma_{P_\perp}$)<br>PARJ(41) = 1.0 (fragmentation function 'a')<br>PARJ(42) = 0.496 (fragmentation function 'B') |
| JETSET 7.3 | Matrix element abelian gluon | Standard ALEPH HVFL03 tune except<br>MSTJ(109) = 2 (abelian vector gluon switch)<br>MSTJ(101) = 3 (qq+qqg+qqgg+qqqq only)<br>MSTJ(108) = 1 (1st order $\alpha_s$)<br>PARJ(121) = 1.5 ($\Lambda$)<br>MSTJ(110) = 1 (GKS matrix elements)<br>MSTJ(111) = 0 (non-optimised scale)<br>PARJ(21) = 0.44 ($\sigma_{P_\perp}$)<br>PARJ(41) = 1.0 (fragmentation function 'a')<br>PARJ(42) = 0.496 (fragmentation function 'B') |
| HERWIG 5.6 | Parton shower | Standard ALEPH HRWG07 tune |

Table 6.5: Monte Carlo model descriptions and parameter values

- **Scalar gluon matrix element:** This is a "toy model" provided by the JETSET program where the gluon is spin 0 as opposed to spin 1. The three jet cross-section is therefore given by

$$\frac{1}{\sigma_0}\frac{d\sigma}{dx_1 dx_2} \propto \frac{x_3^2}{(1-x_1)(1-x_2)} \tag{6.9}$$

where the variable definitions are the same as before. The Dalitz plot should therefore look somewhat different and this is born out by the measured value of $\ln L_0 - \ln L_1 = 435.3$. It is quite obvious that the benchmark parton shower distribution is radically different from the scalar gluon distribution. It can therefore be stated that, given that real data and the JETSET 7.3 parton shower distributions agree perfectly, the scalar gluon model is excluded.

- **Abelian vector gluon model:** The second "toy model" implements a gluon with spin 1 but no colour which makes QCD behave more like QED. In other words, while the $q \rightarrow qg$ transition is permitted the $g \rightarrow gg$ transition is not. However, note that the $g \rightarrow gg$ transition only plays a role in defining the shapes of four or more jet events and therefore it would not be expected to see any disagreement with the benchmark sample. The value of $\ln L_0 - \ln L_1 = 9.0$ bears this out.

- **HERWIG parton shower:** This is the main alternative to JETSET and its differences were discussed in Chapter 2. As would be expected the value of $\ln L_0 - \ln L_1 = 11.0$ shows good agreement with JETSET.

The six distributions are shown in Figure 6.9. Figure 6.10 shows where each measurement fell on the log-likelihood test distribution.

### 6.2.4 Quark and gluon jet properties

Having spent a large amount of time carefully selecting and tagging the 3-jet events used in the preceding analysis an attempt was made to measure certain jet properties such as multiplicity, rapidity, energy ratios etc. It was quickly

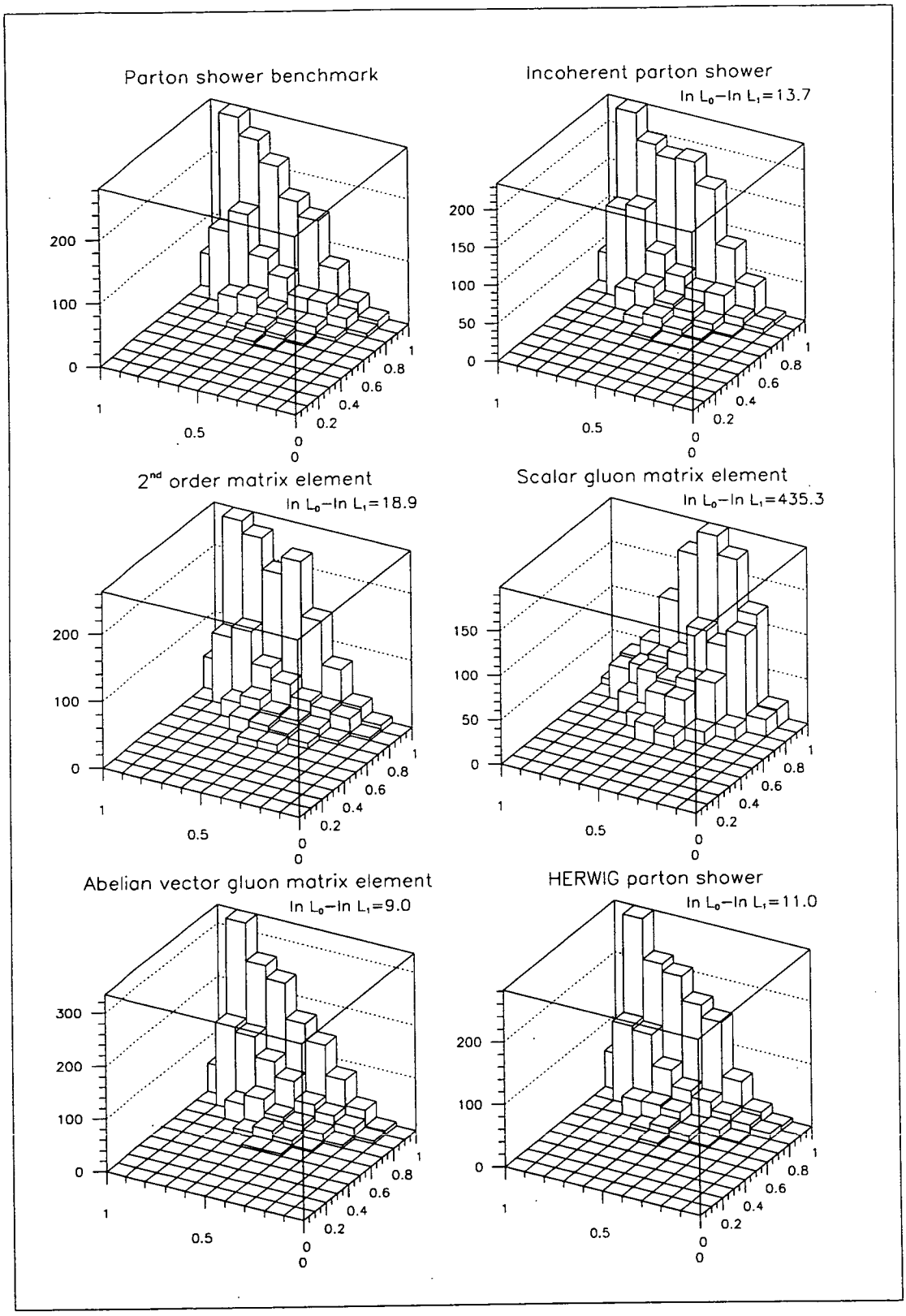


Figure 6.9: The six Monte Carlo distributions with their $\ln L_0 - \ln L_1$ measurements

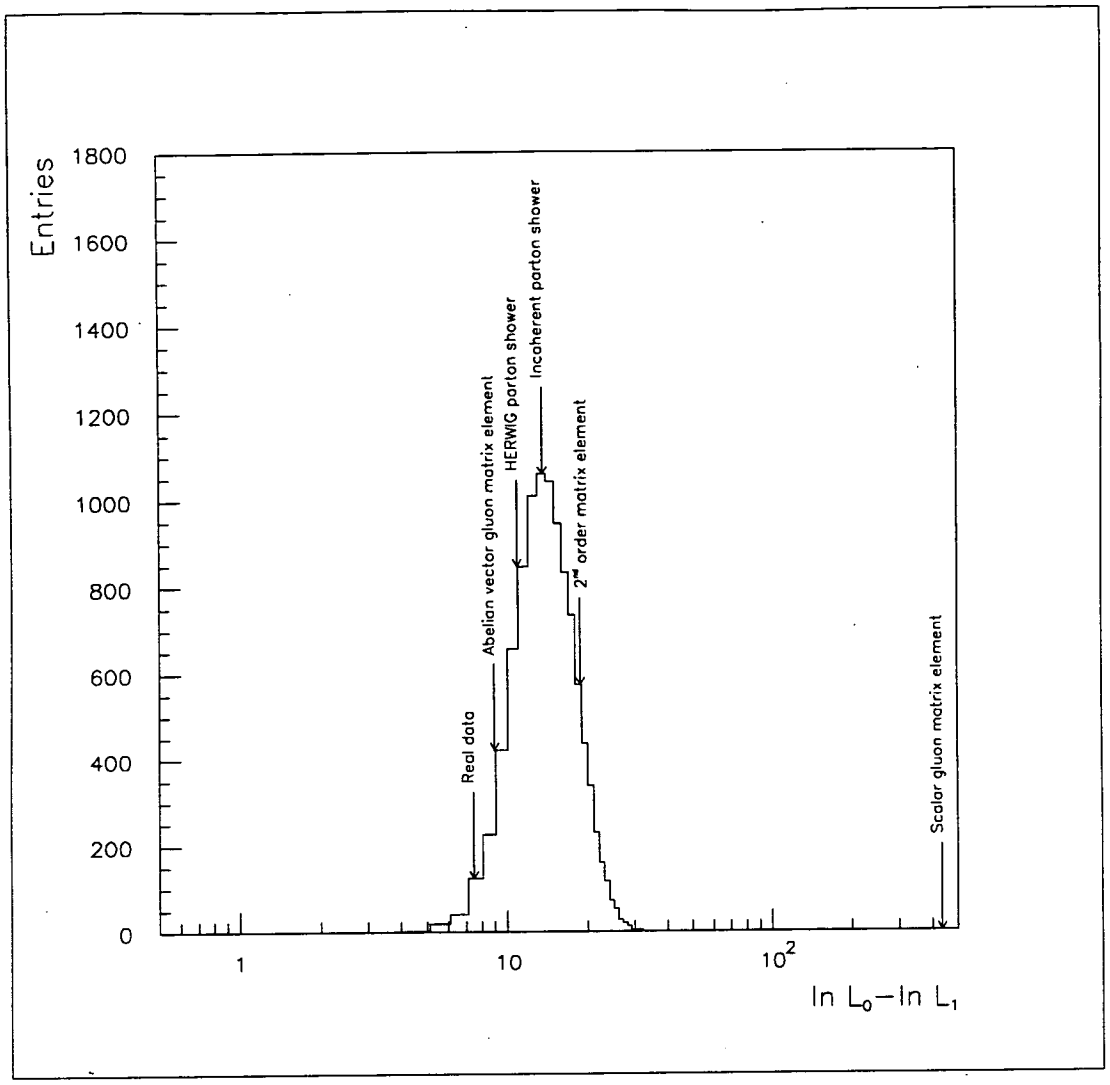


Figure 6.10: Summary of $\ln L_0 - \ln L_1$ results for each Monte Carlo model

realised that measuring any of the quark jet properties would be difficult due to the large bias introduced by the presence of the high $P_\perp$ lepton. One of the main purposes of measuring any properties of quark and gluon jets is obviously to compare differences between them. As the vast majority of gluon jets have low energy, whilst the opposite is true for quark jets, any comparisons need to take this into account or the energy difference of the two jets will mask any real effects.

Many methods to correct for these biases were attempted. Of particular importance were the following:

- All measurements were binned in terms of energy. This helped to reduce the energy bias but because the number of events is quite small the bins

had to be quite wide (10GeV) and therefore some residual bias remained.

- To try to counter the residual energy bias, each measurement was analysed twice. On the first pass the energy distribution of both the quark and gluon jets in each bin was measured. Weights were then calculated so that each individual measurement when binned had a weight applied to it such that the mean energy of the events in each bin was at the centre of the bin.

- A complicated method was devised to try and compensate for the presence of the high $P_\perp$ lepton in each quark jet. Compensations were calculated using Monte Carlo information.

Unfortunately, such large statistical and systematic errors were introduced by all of these corrections that little confidence was held in the final result.

For these reasons a bias free method, similar to that used by the OPAL Collaboration in [23] was devised. It is this method, and the measurements arising from it, which is described in the next chapter.

# Chapter 7

# Quark and Gluon Jet Differences

## 7.1 The Symmetric Event Study

The overriding concern of this study was to reduce the biases described above to a minimum, hence allowing the properties of the selected quark and gluon jets to be measured and contrasted with each other.

To minimise bias due to the differing energy profiles of the quark and gluon jets a symmetric event configuration was chosen (see Figure 7.1). To extract unbiased measurements from the data an unfolding method which involved scanning the data twice was employed. On the first scan a ~50:50 mix of unidentified quark and gluon jets was studied. On the second scan a lepton tag was used to anti-tag the gluon jet (resulting in a ~20:80 mix of quark and gluon jets). By unfolding these measurements using simple simultaneous equations the properties of ~100% pure quark and gluon jets were found. A symmetric 3-jet topology identical to that described by the OPAL collaboration in [23] was used for two reasons. Firstly, this allowed certain results to be compared directly with those of the OPAL collaboration and secondly, because the number of symmetric events is maximised. The OPAL analysis differed in one important respect however. Instead of a high $P_\perp$ lepton tag a vertex detector tag was used to anti-tag the gluon jet[1].

[1] A similar analysis, using a vertex tag, is currently in progress within the ALEPH collaboration. Whilst the vertex tag analysis has been undertaken completely independently, comparison

The following measurements will be presented for both quark and gluon jets:

- Charged track, and charged track and neutral object, multiplicity.
- Charged track rapidity.
- $X_E$ (the fraction of the jet energy carried by each particle in the jet) for both charged tracks and charged tracks and neutral objects.
- $P_\perp$ of each particle in the jet for charged tracks, and charged tracks and neutral objects.
- The ratio of charged to neutral energy in the jet.
- The charged track multiplicity measured in a series of cones aligned around the jet axis.
- The fraction of the total energy in the jet contained in a series of cones centered around the jet axis.

## 7.2 Selecting and analysing symmetric events

Figure 7.1 shows the three different tag configurations employed throughout the analysis. These require some explanation.

In each case exactly the same symmetric topology was used. Energy flow objects were clustered using the DURHAM algorithm, the E-scheme, and a $y_{cut}$ of 0.01 into jets. For any event containing three jets its event plane was then found as described in Section 4.3.1 and the jets projected onto it. Their energies were then calculated. The jet with the maximum energy was then required to be $150 \pm 10^o$ from each of the lower energy jets (this angle being measured in the event plane). The implication of this was that the two lower energy jets were on average $60^o$ from each other and, by virtue of the symmetric topology, of similar energy. The purpose of the three different tagging configurations was as follows:

of results with those of this study has proved very useful (particularly in identifying software bugs etc).

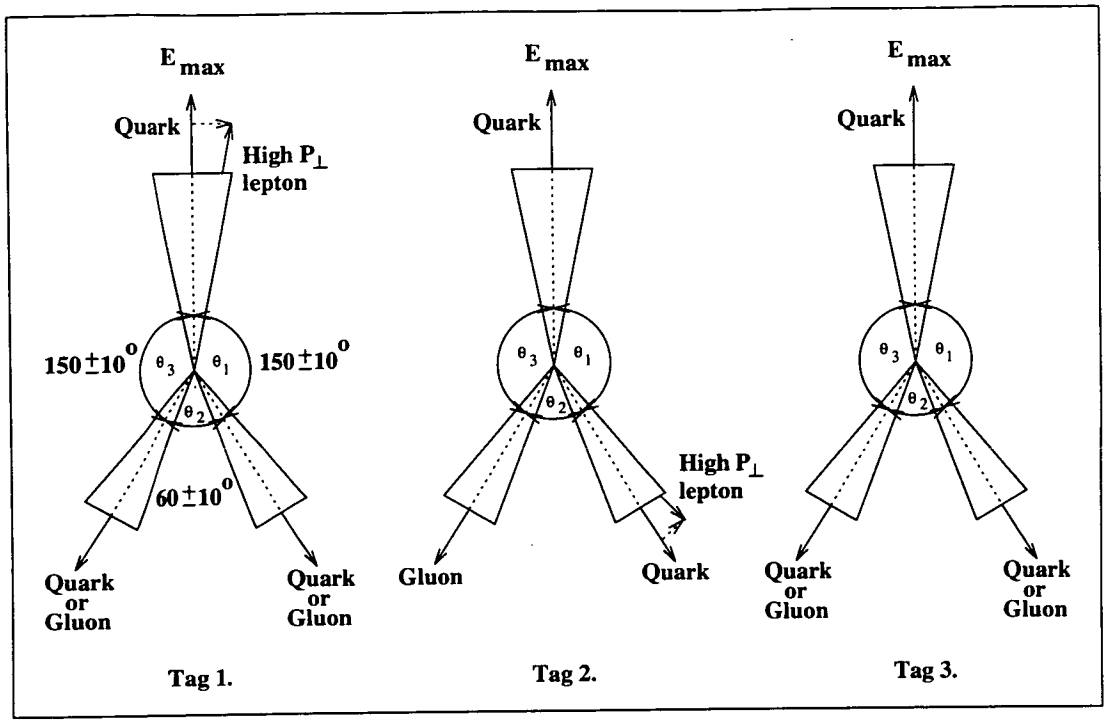


Figure 7.1: The three different tag configurations used in the symmetric event analysis

- **Tag 1:** A high $P_\perp$ lepton ($P_\perp$ >0.5GeV) was required to exist in the highest energy jet. This ensured a very high probability that the maximum energy jet was a quark jet. No attempt was made to categorise the lower energy jets as to do so would have introduced a possible bias. Instead, the measurements taken from this sample consisted of a ~50:50 mix of quark and gluon jets. Note that the effect of the lepton tag was to make this sample predominately $b$-quark flavour.

- **Tag 2:** In this sample, a high $P_\perp$ lepton ($P_\perp$ >0.5GeV) was required to exist in one of the two lower energy jets thereby tagging that jet as a quark jet. It is the case that the highest energy jet in a 3-jet event is almost always a quark jet (precise purity figures will be given later for this symmetric configuration), therefore the lower energy jet which did not contain a $P_\perp$ lepton was anti-tagged with high purity as a gluon jet by default and its properties measured. Again the lepton tag ensured the predominance of b-flavour events in the sample. Figure 7.2 shows an example of a Tag 2 symmetric event. The lower left hand jet is identified as the lower energy

quark jet by the presence of a high $P_\perp$ muon.

- **Tag 3:** For reasons which will become apparent later in this Chapter, it proved useful to study a sample of symmetric events which contained no high $P_\perp$ lepton tag. There is a very high probability that the highest energy jet will be a quark jet. The two lower energy jets therefore provided a ~50:50 mix of quark and gluon jets as in the Tag 1 sample. However the flavour composition of this sample was a mixture of u, d, s, c, and b quark events.

Analysing the measurements made using the above tags and extracting 100% pure quark and gluon jet distributions was accomplished by solving the pair of simultaneous equations given in Equation 7.1. Where $P_{q1}$ and $P_{g1}$ are the quark and gluon purities in the Tag 1 sample and $P_{q2}$ and $P_{g2}$ are the same but for the Tag 2 sample. $N_q$ and $N_g$ are the pure quark and gluon observables required while $N_{qg1}$ and $N_{qg2}$ are the measured values for the Tag 1 and Tag 2 samples respectively. Note that for simplicity as Tag 1 is identical to Tag 3 in terms of unfolding the results, the following text assumes the quark gluon mix from the Tag 1 sample is being used with the gluon sample from Tag 2. When extracting results using the the Tag 3 sample the same method was used except the Tag 3 information was used instead of that of Tag 1.

$$\left.\begin{aligned} P_{q1}N_q + P_{g1}N_g &= N_{qg1} \\ P_{q2}N_q + P_{g2}N_g &= n_{qg2} \end{aligned}\right\} \tag{7.1}$$

Since $P_{q1}$, $P_{q2}$, $P_{g1}$, and $P_{g2}$ were measured using Monte Carlo information, and $N_{qg1}$ and $N_{qg2}$ are known, solving for $N_q$ and $N_g$ is straightforward and uses the constraint that $P_{qi} + P_{gi} = 1$ where $i = 1, 2, 3$.

$$N_q = \frac{P_{g2}N_{qg1} - P_{g1}N_{qg2}}{P_{g2} - P_{g1}} \tag{7.2}$$

$$N_g = \frac{P_{q2}N_{qg1} - P_{q1}N_{qg2}}{P_{q2} - P_{q1}} \tag{7.3}$$

Each of the quantities on the right-hand side of the equation has an associated

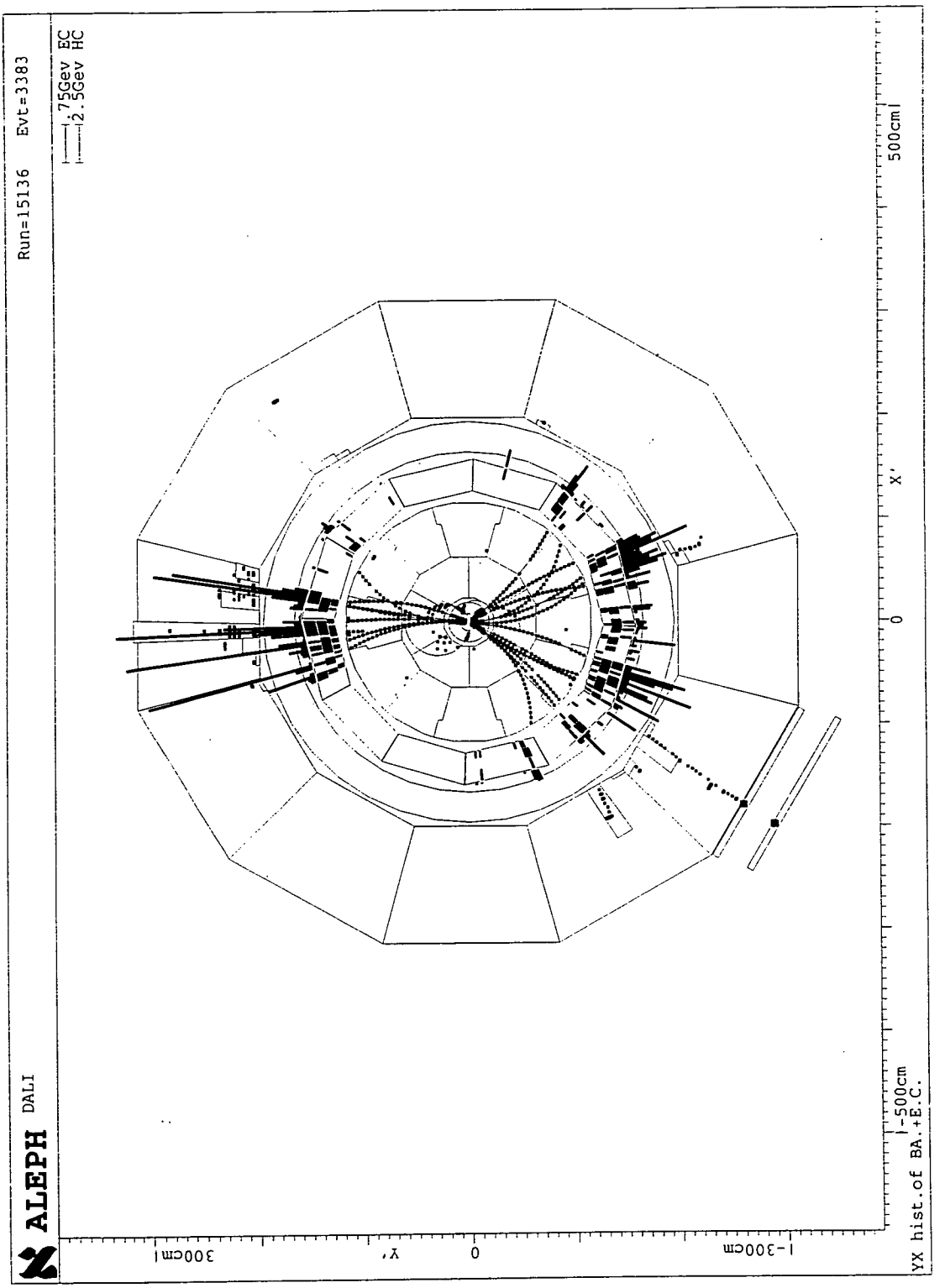


Figure 7.2: An example of a Tag 2 symmetric three jet event

statistical error and therefore the statistical errors on $N_q$ and $N_g$ were found as follows. In this notation $\delta P_{g1}$ is the statistical error on $P_{g1}$ and so forth.

$$\begin{aligned}\delta N_q^2 &= \left(\frac{\partial N_q}{\partial P_{g1}}\right)^2 \delta P_{g1}^2 + \left(\frac{\partial N_q}{\partial N_{qg1}}\right)^2 \delta N_{qg1}^2 + \\ &\left(\frac{\partial N_q}{\partial P_{g2}}\right)^2 \delta P_{g2}^2 + \left(\frac{\partial N_q}{\partial N_{qg2}}\right)^2 \delta N_{qg2}^2 \end{aligned} \tag{7.4}$$

$$\begin{aligned}\delta N_g^2 &= \left(\frac{\partial N_g}{\partial P_{q1}}\right)^2 \delta P_{q1}^2 + \left(\frac{\partial N_g}{\partial N_{qg1}}\right)^2 \delta N_{qg1}^2 + \\ &\left(\frac{\partial N_g}{\partial P_{q2}}\right)^2 \delta P_{q2}^2 + \left(\frac{\partial N_g}{\partial N_{qg2}}\right)^2 \delta N_{qg2}^2 \end{aligned} \tag{7.5}$$

$$\begin{aligned}\Rightarrow \delta N_q &= \left(\frac{\delta N_{qg1}^2 P_{g2}^2}{(P_{g2}-P_{g1})^2} + \frac{\delta N_{qg2}^2 P_{g1}^2}{(P_{g2}-P_{g1})^2} + \right. \\ &\delta P_{g2}^2 \left\{\frac{N_{qg1}}{(P_{g2}-P_{g1})} - \frac{P_{g2}N_{qg1} - P_{g1}N_{qg2}}{(P_{g2}-P_{g1})^2}\right\}^2 + \\ &\left.\delta P_{g1}^2 \left\{\frac{P_{g2}N_{qg1} - P_{g1}N_{qg2}}{(P_{g2}-P_{g1})^2} - \frac{N_{qg2}}{(P_{g2}-P_{g1})}\right\}^2\right)^{\frac{1}{2}} \end{aligned} \tag{7.6}$$

$$\begin{aligned}\Rightarrow \delta N_g &= \left(\frac{\delta N_{qg1}^2 P_{q2}^2}{(P_{q2}-P_{q1})^2} + \frac{\delta N_{qg2}^2 P_{q1}^2}{(P_{q2}-P_{q1})^2} + \right. \\ &\delta P_{q2}^2 \left\{\frac{N_{qg1}}{(P_{q2}-P_{q1})} - \frac{P_{q2}N_{qg1} - P_{q1}N_{qg2}}{(P_{q2}-P_{q1})^2}\right\}^2 + \\ &\left.\delta P_{q1}^2 \left\{\frac{P_{q2}N_{qg1} - P_{q1}N_{qg2}}{(P_{q2}-P_{q1})^2} - \frac{N_{qg2}}{(P_{q2}-P_{q1})}\right\}^2\right)^{\frac{1}{2}} \end{aligned} \tag{7.7}$$

It was sometimes useful to express the difference between a quark and gluon measurement as the ratio $N_g/N_q$. Using the definitions above for $N_g$ and $N_q$ the expression given in Equation 7.8 results. It is purposely expressed in this form to avoid having to calculate an error covariance matrix.

$$\mathcal{R} = \frac{N_g}{N_q} = \frac{N_{qg2} - N_{qg1}}{P_{g2}N_{qg1} - P_{g1}N_{qg2}} + 1 \tag{7.8}$$

The statistical error on $N_g/N_q$ was found by solving:

$$\delta\mathcal{R}^2 = \left(\frac{\partial\mathcal{R}}{\partial P_{g1}}\right)^2 \delta N_{g1}^2 + \left(\frac{\partial\mathcal{R}}{\partial N_{qg1}}\right)^2 \delta N_{qg1}^2 + \left(\frac{\partial\mathcal{R}}{\partial P_{g2}}\right)^2 \delta N_{g2}^2 + \left(\frac{\partial\mathcal{R}}{\partial N_{qg2}}\right)^2 \delta N_{qg2}^2 \quad (7.9)$$

$$\Rightarrow \delta\mathcal{R} = \left(\frac{\delta P_{g1}^2 B^2 N_{qg2}^2}{A^4} + \frac{\delta P_{g2}^2 B^2 N_{qg1}^2}{A^4} + \delta N_{qg1}^2 \left\{-\frac{1}{A} - P_{g2}\frac{B}{A^2}\right\}^2 + \delta N_{qg2}^2 \left\{\frac{1}{A} + P_{g1}\frac{B}{A^2}\right\}^2\right)^{\frac{1}{2}} \quad (7.10)$$

Where $A = (P_{g2}N_{qg1} - P_{g1}N_{qg2})$ and $B = (N_{qg2} - N_{qg1})$.

The method used to measure the purity is very similar to that used in the Dalitz analysis and is described shortly. Prior to this, the following section describes the preselection and full selection of the different event samples and gives precise details of their size.

## 7.3 Event selection

It proved extremely useful to make a preselection of events which were stored on disk for further analysis. The preselection procedure was not applicable to Tag 3 events (due to the high event rate) and therefore the analysis code was fully developed before the complete ALEPH miniDST data sets were processed with Tag 3[2].

### 7.3.1 Preselection

The cuts applied at this stage were designed to greatly reduce the data set size while not losing any events which might be of interest to Tag 1 or 2. To be preselected an event was required to:

- Pass the standard ALEPH hadronic event selection described in Section 5.2.

[2]Processing 650000 Monte Carlo events takes approximately 5 days. Multiple processings were therefore not desirable.

| Applied cuts | Real data | | | | Monte Carlo |
|---|---|---|---|---|---|
| | 1990 | 1991 | 1992 | Total | 1992 geom. |
| Total hadronic | 111799 | 225777 | 658714 | 996290 | 992878 |
| Three jet events | 35189 | 70428 | 205361 | 310978 | 332125 |
| Beam pipe cut | 23505 | 47161 | 137166 | 207832 | 217180 |
| Event plane ok | 23423 | 47063 | 136874 | 207360 | 216830 |
| Symmetric event | 1728 | 3389 | 10274 | 15391 | 16520 |
| $\geq 1$ high $P_\perp$ lepton | 143 | 333 | 1016 | 1492 | 1461 |
| Total preselected | 143 | 333 | 1016 | 1492 | 1461 |

Table 7.1: The preselection process and its effect on event rates

- Contain, after clustering of energy flow objects with the DURHAM algorithm, E-scheme and a $y_{cut}$ of 0.01, three jets.
- Pass the same jet beam pipe cut of $\theta_{jet} \geq 30^o$ as was described in Section 6.2.1.
- Have a well defined (ie. calculable) event plane into which the three jets could be projected.
- Have the angular topology as shown in Figure 7.1 of $\theta_{1\rightarrow 2,3} = 150 \pm 10^o$.
- Contain at least 1 high $P_\perp$ lepton with $P_\perp > 0.5$GeV.

These requirements significantly reduced the data set size. The number of selected events is given in Table 7.1. Data from 1990, 1991, and 1992 was studied and was selected using SCANBOOK with the same criteria as given in Section 6.2.1. The Monte Carlo data comprised a subsample of the fully reconstructed standard ALEPH JETSET 7.3 Monte Carlo based on the 1992 ALEPH geometry as has been described previously. The number of Monte Carlo events was chosen to be approximately the same as the real data. In all aspects of event selection the Monte Carlo was treated the same as the real data.

### 7.3.2 Full event selection

The comprehensive nature of the preselection meant that the full event selection for Tags 1 and 2 consisted of reapplying the same criteria as for the preselection plus applying the particular tag required. Table 7.2 shows the final number of

| | 1990+1991+1992 Data | Monte Carlo |
|---|---|---|
| Preselected events | 1492 | 1461 |
| Total Tag 1 events | 762 | 806 |
| Total Tag 2 events | 818 | 745 |

Table 7.2: Events remaining after application of Tags 1 and 2

events selected for Tags 1 and 2. Complete event selection information for Tag 3 is given in Table 7.3[3]. Due to the high event rate, and the fact that any result extracted from the data set was constrained by the statistical error on the purity measurement of the Tag 2 sample, only 1992 real data events were used. The Monte Carlo data was chosen from the same data set as used above.

## 7.4 Event purity and flavour composition

As before, purity was calculated by angularly matching the detector jets with parton level jets created as described in Section 4.3.3. Fortunately, the number of ambiguous events was much reduced due to the well defined topology of the events. The statistical error on the purity was again calculated using Equation 6.3. As in the Dalitz analysis the only systematic error considered was associated with the purity calculation and the ambiguous events. The actual measurement of the purity and its corresponding systematic error is described for each tag below.

[3]The alert reader will notice that there is 2% descrepancy between the three jet rates for data and Monte Carlo. This is due to a Monte Carlo tuning problem and is under investigation

| Applied cuts | Real data 1992 | Monte Carlo 1992 geom. |
|---|---|---|
| Total hadronic | 658713 | 649912 |
| Three jet events | 205361 | 217349 |
| Beam pipe cut | 137166 | 142095 |
| Event plane ok | 136874 | 141862 |
| Symmetric event | 10274 | 10695 |
| Total Tag 3 events | 10274 | 10695 |

Table 7.3: Event selection process for Tag 3

| Flavour | N°. events | |
|---|---|---|
| u | 27 | 3.3% |
| d | 35 | 4.3% |
| s | 43 | 5.5% |
| c | 165 | 20.5% |
| b | 536 | 66.5% |

Table 7.4: The flavour composition of the Tag 1 event sample

### 7.4.1 Tag 1

Because this tag contained a high $P_\perp$ lepton tag in the maximum energy jet its flavour composition was expected to be rich in $c$ and $b$ quark events. This is confirmed in Table 7.4. The observant reader will notice that the $b$ purity is much reduced compared with Table 6.3. This is because two high $P_\perp$ leptons were required in the previous analysis. A higher $b$ purity is easily attainable by increasing the $P_\perp$ cut but this would have had the unacceptable side of effect of reducing the tagged event sample size considerably.

Ideally a 50 : 50 mix of quark and gluon jets was expected using this tag. However, in a small number of cases the gluon jet was found to be the most energetic jet therefore the properties of two quark jets as opposed to the expected quark-gluon pair were measured. In addition to badly tagged events there was also a small number for which the purity information was not available due to either badly formed parton jets or a maximum matching angle, $\theta_{max}$, greater than 40°. This information is summarised in Table 7.5.

The actual value for the purity was calculated using the number of jets rather than events. The reason for this is rather subtle and arises because one quark

| | N°. affected | N°. remaining |
|---|---|---|
| Selected | - | 806 |
| Bad parton jets | 6 | 800 |
| $\theta_{max} > 40°$ | 7 | 793 |
| | Event composition | |
| Correct tag | | 782 |
| Wrong tag | 793 - 782 = | 11 |
| Ambiguous tag | 6 + 7 = | 13 |

Table 7.5: Tag 1 - event sample purity composition

jet was always present in the pair of measurements gained from each event. Therefore Equation 6.2 did not apply and Equation 7.11 was used in its place.

$$P_{q1} = 1 - P_{g1} = \frac{C + \frac{3}{4}A}{2 \times \text{Number of events}} \tag{7.11}$$

$$\begin{aligned}
\text{where } C &= \text{Number of quark jets in the correct events} + \\
&\quad \text{the number of quark jets in the wrong events} \\
\Rightarrow C &= 782 + 2 \times 11, \\
\text{and } A &= \text{Number of ambiguous jets} \\
\Rightarrow A &= 2 \times 13.
\end{aligned}$$

The $\frac{3}{4}A$ term assumes that of the ambiguous jets half will always be quark jets, and of the remaining half, half of these will be gluon jets. In other words that half of the events will be tagged correctly and half will not. The systematic error was found by using $C + A$ as the numerator (implying all unknown jets were gluon jets) and then $C + \frac{1}{2}A$ (implying all unknown jets were quark jets). The calculated value with statistical and systematic errors was therefore found to be:

$$\begin{aligned}
P_{q1} &= \frac{782 + 22 + \frac{3}{4} \times 26}{1612} = 0.511 \pm 0.012 \\
P_{q1}^{max} &= \frac{782 + 22 + 26}{1612} = 0.515 \pm 0.012 \\
P_{q1}^{min} &= \frac{782 + 22 + 13}{1612} = 0.507 \pm 0.012
\end{aligned}$$

$$\begin{aligned}
\Rightarrow P_{q1} &= P_{q1} \pm \delta P_{q1}^{stat} \pm \delta P_{q1}^{syst} = 0.511 \pm 0.012 \pm 0.004 \\
\Rightarrow P_{g1} &= 1 - P_{q1} = 0.489 \pm 0.012 \pm 0.004
\end{aligned}$$

### 7.4.2 Tag 2

Table 7.6 shows the flavour composition of the tagged events. Again $c$ and $b$ quark events are prominent due to the presence of a high $P_\perp$ lepton in one of the lower energy jets.

The calculation of the gluon jet purity is considerably more straightforward

| Flavour | N°. events | |
|---|---|---|
| u | 45 | 6.0% |
| d | 46 | 6.2% |
| s | 74 | 9.9% |
| c | 131 | 17.6% |
| b | 449 | 60.3% |

Table 7.6: Flavour composition of the Tag 2 event sample

in this case and is essentially the same as used in Section 6.2.2. The breakdown of events is given in Table 7.7.

The gluon and quark purity was found to be as follows:

$$
\begin{aligned}
P_{g2} &= \frac{C + \frac{A}{2}}{C + W + A} = \frac{607 + \frac{4}{2}}{745} = 0.817 \pm 0.014 \\
P_{g2}^{max} &= \frac{C + A}{C + W + A} = \frac{607 + 4}{745} = 0.820 \pm 0.014 \\
P_{g2}^{min} &= \frac{C}{C + W + A} = \frac{607}{745} = 0.815 \pm 0.014
\end{aligned}
$$

$$
\begin{aligned}
\Rightarrow P_{g2} &= P_{g2} \pm \delta P_{g2}^{stat} \pm \delta P_{g2}^{syst} = 0.817 \pm 0.014 \pm 0.003 \\
\Rightarrow P_{q2} &= 1 - P_{g2} = 0.183 \pm 0.014 \pm 0.003
\end{aligned}
$$

### 7.4.3 Tag 3

The purity calculation of the Tag 3 sample was treated identically to that of the Tag 1 sample. The major difference between the two samples being in the flavour composition due to the lack of a high $P_\perp$ lepton in either of the three jets of this sample. As would be expected an essentially equal flavour mix results which is shown in Table 7.8.

| | N°. affected | N°. remaining |
|---|---|---|
| Selected | - | 745 |
| Bad parton jets | 2 | 743 |
| $\theta_{max} > 40^o$ | 2 | 741 |
| | Event composition | |
| Correct tag | | 607 |
| Wrong tag | 741 - 607 = | 134 |
| Ambiguous tag | 2 + 2 = | 4 |

Table 7.7: Tag 2 - event sample purity composition

| Flavour | N°. events | |
|---|---|---|
| u | 1912 | 17.9% |
| d | 2324 | 21.7% |
| s | 2413 | 22.6% |
| c | 1862 | 17.4% |
| b | 2184 | 20.4% |

Table 7.8: Flavour composition of the Tag 3 event sample

The events were studied in exactly the same way as above and Table 7.9 summarises the results.

The quark and gluon purity was found using the same equations as for Tag 1 and is given below.

$$P_{q3} = \frac{C + \frac{3}{4}A}{C + W + A} = \frac{10778 + \frac{3}{4} \times 332}{2 \times 10695} = 0.516 \pm 0.003$$

$$P_{q3}^{max} = \frac{C + A}{C + W + A} = \frac{10778 + 332}{2 \times 10695} = 0.519 \pm 0.003$$

$$P_{q3}^{min} = \frac{C + \frac{1}{2}A}{C + W + A} = \frac{10778 + \frac{1}{2} \times 332}{2 \times 10695} = 0.512 \pm 0.003$$

$$\Rightarrow P_{q3} = P_{q3} \pm \delta P_{q3}^{stat} \pm \delta P_{q3}^{syst} = 0.516 \pm 0.003 \pm 0.004$$

$$\Rightarrow P_{g3} = 1 - P_{q3} = 0.484 \pm 0.003 \pm 0.004$$

The purity values calculated above were used to extract the pure quark and gluon distributions from the following measurements which were designed to highlight any differences between quark and gluon jets.

| | N°. affected | N°. remaining |
|---|---|---|
| Selected | - | 10695 |
| Bad parton jets | 106 | 10589 |
| $\theta_{max} > 40^o$ | 60 | 10529 |
| | Event composition | |
| Correct tag | | 10280 |
| Wrong tag | 10529 - 10280 = | 249 |
| Ambiguous tag | 106 + 60 = | 166 |

Table 7.9: Tag 3 - event sample purity composition

## 7.5 Quark and gluon jet measurements

Both real data and Monte Carlo data measurements are shown for comparison and in all cases the pure quark and gluon distributions shown were extracted using the pair of equations given by Equation 7.2. Error bars, calculated using Equations 7.6 and 7.7, are shown on the distributions. A discussion of the relative contributions of the statistical and systematic errors is included in the multiplicity section.

### 7.5.1 Multiplicity

Separate measurements of the charged track and charged track and neutral object multiplicity were made. As discussed in Chapter 2 the expected result of this measurement was that the gluon jets would have a higher multiplicity than the quark jets. Taking the charged track measurements first, the distributions of which are shown in Figures 7.3 and 7.4 several general comments pertaining to the layout of the histograms may be made.

In all of the following histograms the quark jet distributions are displayed using an open triangle whilst the gluons are shown using a solid circle. In all cases the upper histogram shows the pure quark and gluon distributions obtained from the Tag 1 and Tag 2 data samples, with the lower histogram displaying the same measurement but for the Tag 3 and Tag 2 data samples. The upper histogram quark distribution is therefore "b-rich" whilst the lower histogram quark distribution is of mixed flavour. All distributions are normalised either to the number of jets in the sample or the total number of particles (in this case the normalisation is to the number of jets). For a given measurement the real data distribution will be given followed by the Monte Carlo distribution on the next page. The data type is clearly labeled. All distributions have been extracted using Equations 7.2, 7.6, and 7.7.

The multiplicity was found for each distribution simply by counting the number of charged particles contained in the jet in question. The numerical values of measured mean multiplicity (plus associated statistical error) are given in

| Tag | | Multiplicity | |
|---|---|---|---|
| | | Data | Monte Carlo |
| 1 | $N_{qg1}$ | $7.995 \pm 0.085$ | $7.991 \pm 0.077$ |
| 2 | $N_{qg2}$ | $8.002 \pm 0.108$ | $8.185 \pm 0.109$ |
| 3 | $N_{qg3}$ | $7.621 \pm 0.023$ | $7.576 \pm 0.021$ |

Table 7.10: The measured charged multiplicity for real and Monte Carlo data

Table 7.10.

Using the values of purity calculated earlier the pure results given in Table 7.11 were extracted. Solving the pair of equations given by Equation 7.2 with the maximum and minimum values of quark and gluon purity resulted in a change to the quark and gluon measurements of $\pm 1$ in the second decimal place. The systematic error on the purity was therefore deemed to be of little consequence although the statistical and systematic errors on the purity were added together in quadrature for consistency. The measurements are dominated by the statistical errors.

Commenting first on the results for real data it should be immediately obvious why the Tag 3 sample was introduced into the analysis - without this data sample the expected difference between quark and gluon jets doesn't appear to exist. The b-jet multiplicity is essentially the same as the gluon jet multiplicity.

This result was initially extremely surprising as it was expected that, since the B or D meson contains a significant fraction of the total energy of the jet, the number of particles produced would be reduced. This phenomenon is discussed

| Tags 1&2 | Multiplicity | |
|---|---|---|
| | Data | Monte Carlo |
| $n_g$ | $8.01 \pm 0.17$ | $8.29 \pm 0.18$ |
| $n_q$ | $7.98 \pm 0.27$ | $7.70 \pm 0.25$ |
| $n_g/n_q$ | $1.003 \pm 0.053$ | $1.077 \pm 0.055$ |
| **Tags 3&2** | **Multiplicity** | |
| | Data | Monte Carlo |
| $n_g$ | $8.21 \pm 0.17$ | $8.52 \pm 0.17$ |
| $n_q$ | $7.07 \pm 0.17$ | $6.69 \pm 0.17$ |
| $n_g/n_q$ | $1.162 \pm 0.051$ | $1.273 \pm 0.058$ |

Table 7.11: Extracted charged multiplicity measurements for real and Monte Carlo data

in [21] and [41] where the distinction is drawn between leading and non-leading fragmentation products. The leading products include the undecayed B or D meson and the multiplicity would, as expected, be considerably less than a gluon jet of the same energy. However, after decay of the meson (referred to as non-leading fragmentation) in [21] the multiplicity increases. In this study, what is obvious is that the extra fragmentation due to the meson decay is obscuring the higher multiplicity of the gluon jet. This is a theme which is present throughout the following series of measurements.

The Monte Carlo simulations correctly model the enhanced multiplicity of the b-jet sample when compared with the mixed flavour jets but, and again this is a theme evident throughout these measurements, they over estimate the quark and gluon jet differences.

The OPAL Collaboration has published a similar measurement in [23] which used a vertex tag for jet identification. Apart from the difference in tagging method the two analyses were identical. OPAL found for real data:

$$\begin{aligned} n_g &= 9.10 \pm 0.10 \\ n_q &= 6.86 \pm 0.09 \\ n_g/n_q &= 1.326 \pm 0.091 \end{aligned}$$

Whilst the quark measurements (corresponding to the Tag 3 sample) are approximately the same to within statistical error, the OPAL gluon measurements are considerably higher than those measured in this analysis. An ALEPH analysis (as yet unpublished) which uses a vertex tag in a similar way to OPAL agrees with the present analysis to within statistical error rather than with the OPAL result. Despite considerable efforts no explanation for this discrepancy has been found.

Multiplicity measurements were also made using both charged tracks and neutral objects. The measured results for each tag are summarised in Table 7.12.

The pure quark and gluon results are given in Table 7.13 and show that for

| Tag | Multiplicity | |
|---|---|---|
| | Data | Monte Carlo |
| 1 | $15.40 \pm 0.128$ | $15.07 \pm 0.116$ |
| 2 | $15.14 \pm 0.162$ | $15.39 \pm 0.167$ |
| 3 | $14.78 \pm 0.035$ | $14.55 \pm 0.033$ |

Table 7.12: The measured charged and neutral multiplicity for real and Monte Carlo data

real data the b-jet multiplicity is greater than the gluon jet multiplicity. The difference between the mixed flavour and gluon jet measurements is considerably reduced (as demonstrated by the low $n_g/n_q$ ratio). One suggestion as to why this may be the case lies not with physics but with the granularity of the energy flow algorithm. The size of a neutral object relies as much on the definition of a calorimeter cluster as on its direct relation to a single neutral particle. This therefore leads to smearing of any small but measurable quark/gluon differences. Other measurements with energy flow neutral objects are included but this problem should be borne in mind. Direct comparison with the OPAL charged and neutral measurements was not possible due to the large differences between the energy flow algorithms used. Again the Monte Carlo measurements over estimate the jet differences.

| Tags 1&2 | Multiplicity | |
|---|---|---|
| | Data | Monte Carlo |
| $n_g$ | $14.99 \pm 0.26$ | $15.57 \pm 0.27$ |
| $n_q$ | $15.78 \pm 0.40$ | $14.59 \pm 0.38$ |
| $n_g/n_q$ | $0.950 \pm 0.039$ | $1.067 \pm 0.044$ |
| **Tags 3&2** | **Multiplicity** | |
| | Data | Monte Carlo |
| $n_g$ | $15.34 \pm 0.25$ | $15.85 \pm 0.27$ |
| $n_q$ | $14.26 \pm 0.25$ | $13.32 \pm 0.26$ |
| $n_g/n_q$ | $1.076 \pm 0.036$ | $1.189 \pm 0.043$ |

Table 7.13: Extracted charged and neutral multiplicity measurements for real and Monte Carlo data

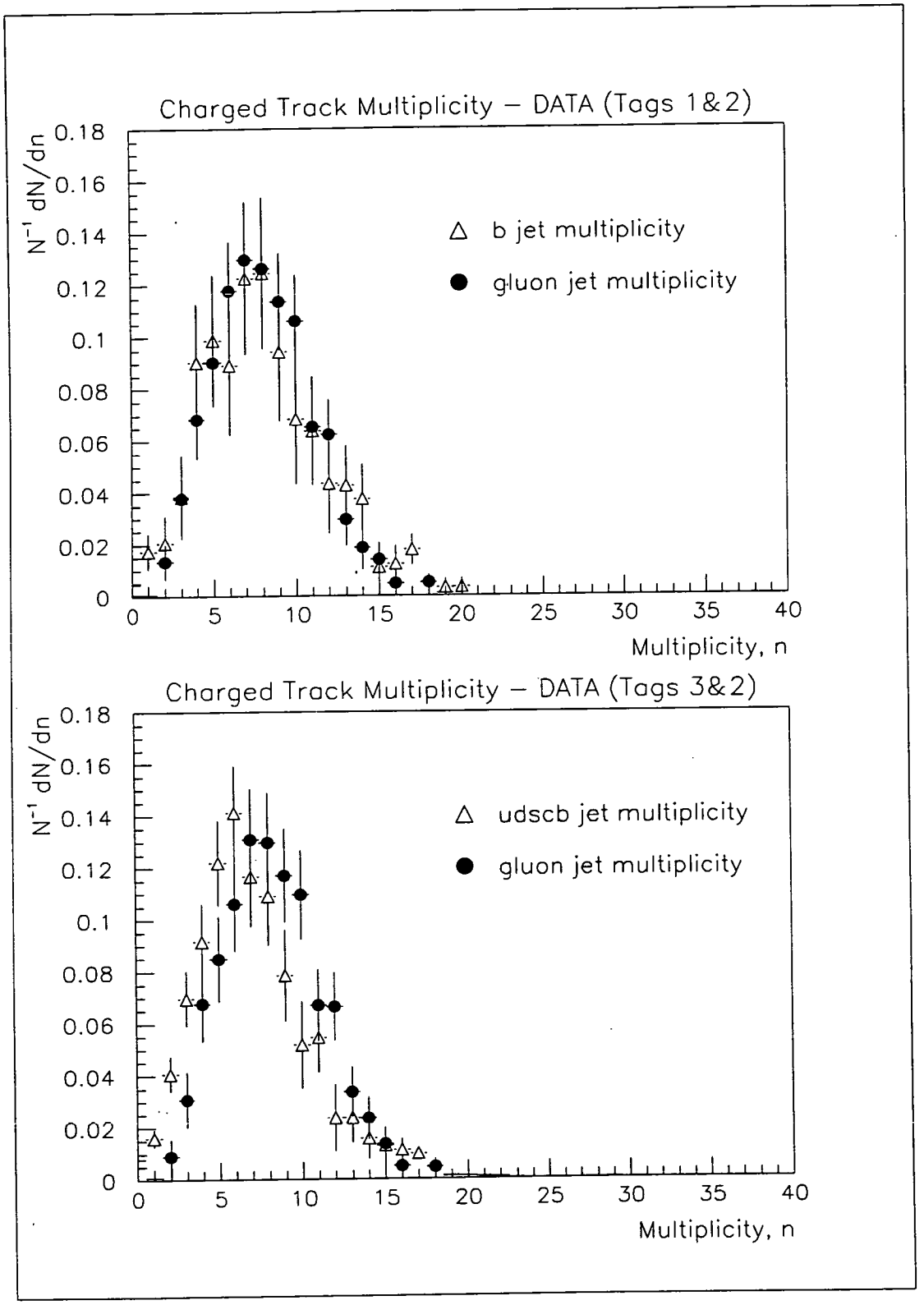


Figure 7.3: Charged track multiplicity - real data

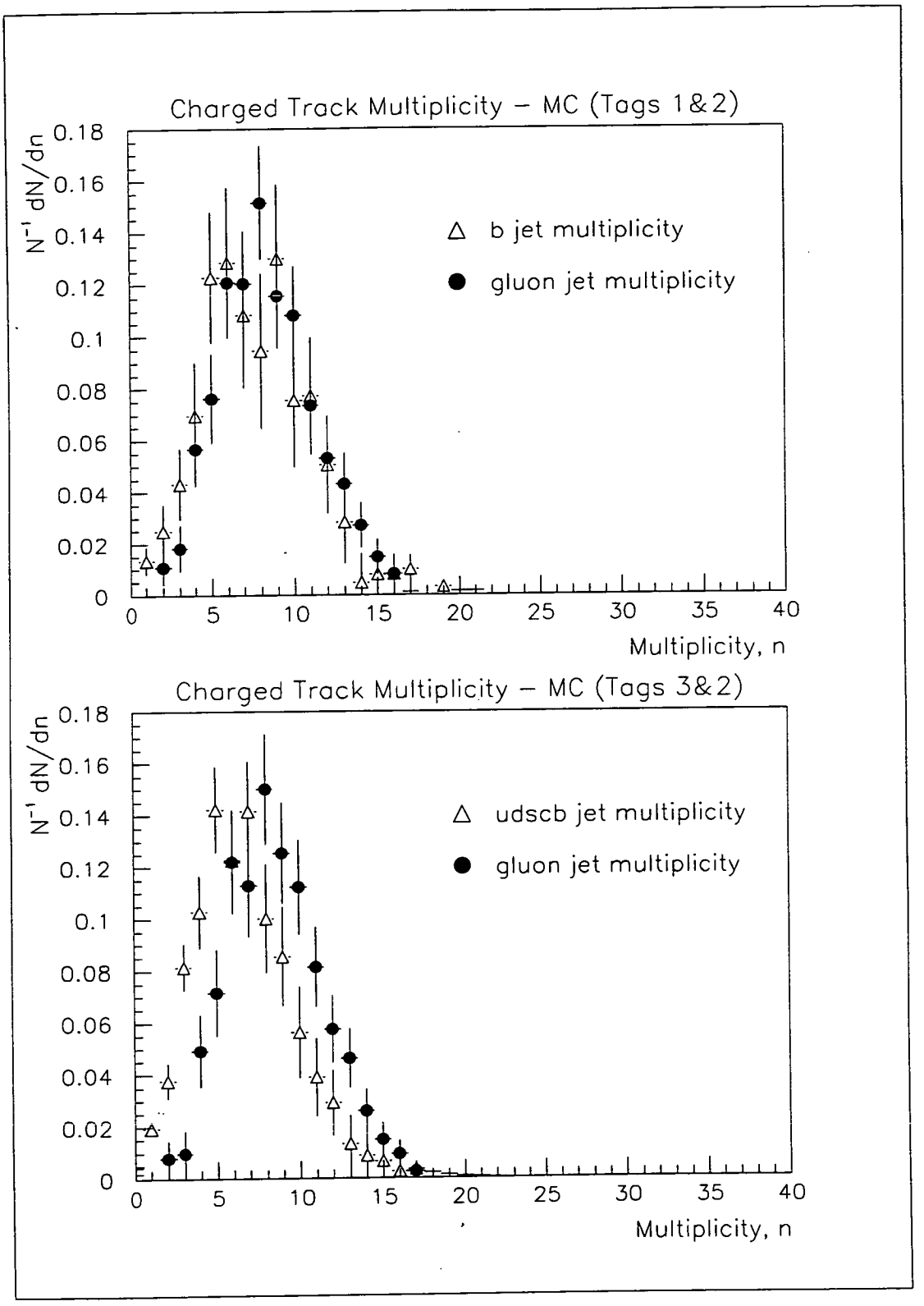


Figure 7.4: Charged track multiplicity - Monte Carlo data

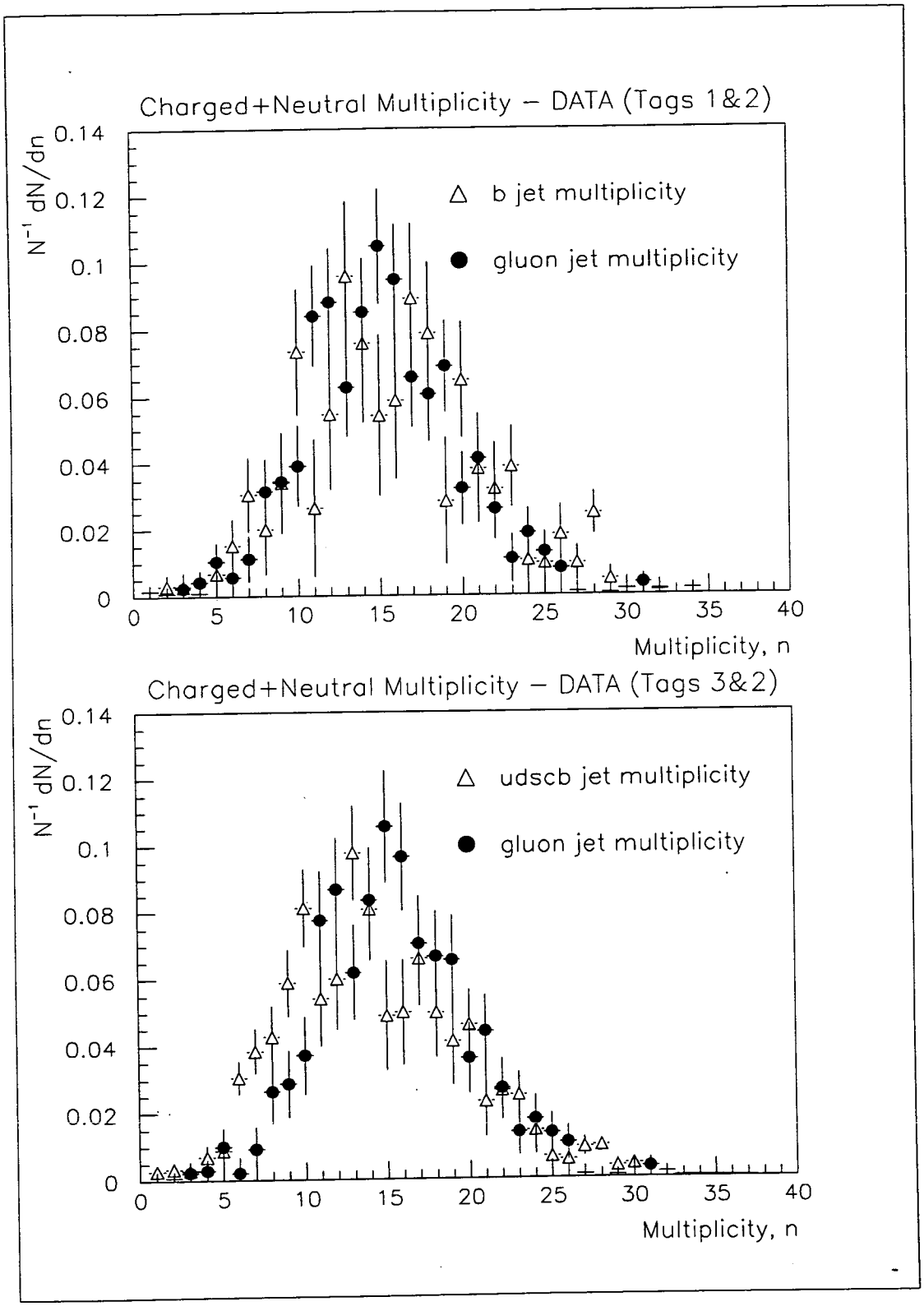


Figure 7.5: Charged track and neutral object multiplicity - real data

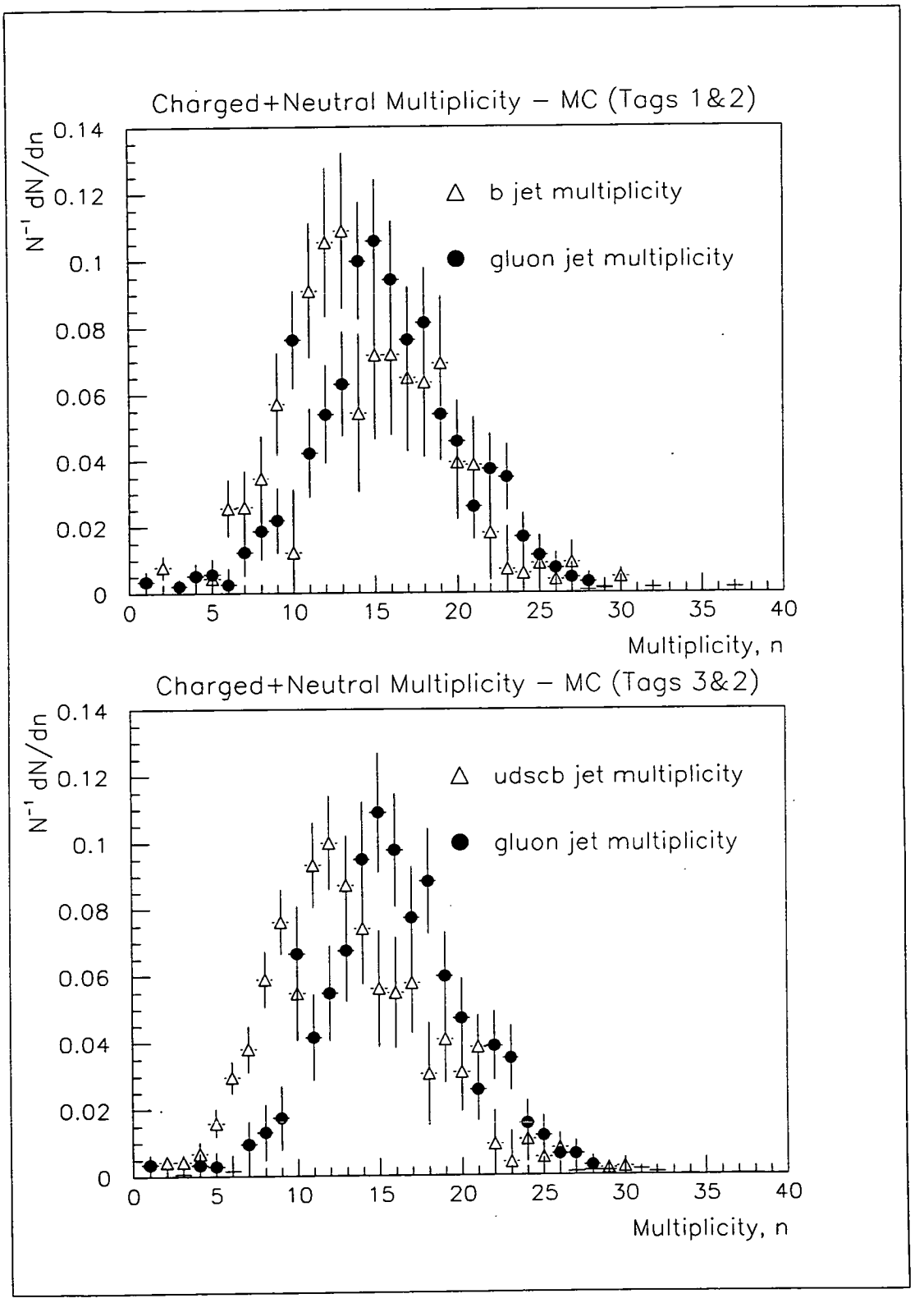


Figure 7.6: Charged track and neutral object multiplicity - Monte Carlo data

### 7.5.2 Rapidity

The rapidity, $\eta$, of a particle was defined in Chapter 2 as

$$\eta = \frac{1}{2} \ln \left( \frac{E + P_{||}}{E - P_{||}} \right) \tag{7.12}$$

where $E$ is the energy of the particle and $P_{||}$ is in this case defined as the longitudinal momentum of the particle with respect to the axis of the jet to which it belongs (the pion mass is assumed). As was discussed in Chapter 2 and illustrated in Figure 2.3 the predicted shapes of rapidity distributions for quark and gluon jets are considerably different. The prediction is that quark jets should contain fewer particles than a gluon jet of the same energy and that more of these particles should be collinear with the jet axis. In other words gluon jets of the same energy should contain more particles of lower energy (because the same total energy is being shared between them) and they will be wider. This leads to the predicted "perfect" distributions.

The shape of these distributions obviously relies partly on a measurable difference in multiplicity between the quark and gluon jets. As was discussed in the previous measurement this is not the case and therefore the distributions shown in Figures 7.7 and 7.8 result. Only charged tracks have been studied as, due to the same reasons given in the previous section, most of the noticeable differences were obscured if charged tracks and neutral objects were considered together. The distributions were normalised to the number of jets in their respective samples.

Although there is admittedly some evidence that the b-jets are more collinear, overall they show little difference. However, the mixed flavour jet sample shows noticeable differences between the quark and gluon jets. Although not nearly as impressive as might be expected the lower plot does go some way to confirming the predictions discussed previously.

The general shape of the Monte Carlo data distributions is the same as that of the real data but again seems to overestimate somewhat the quark and gluon jet differences.

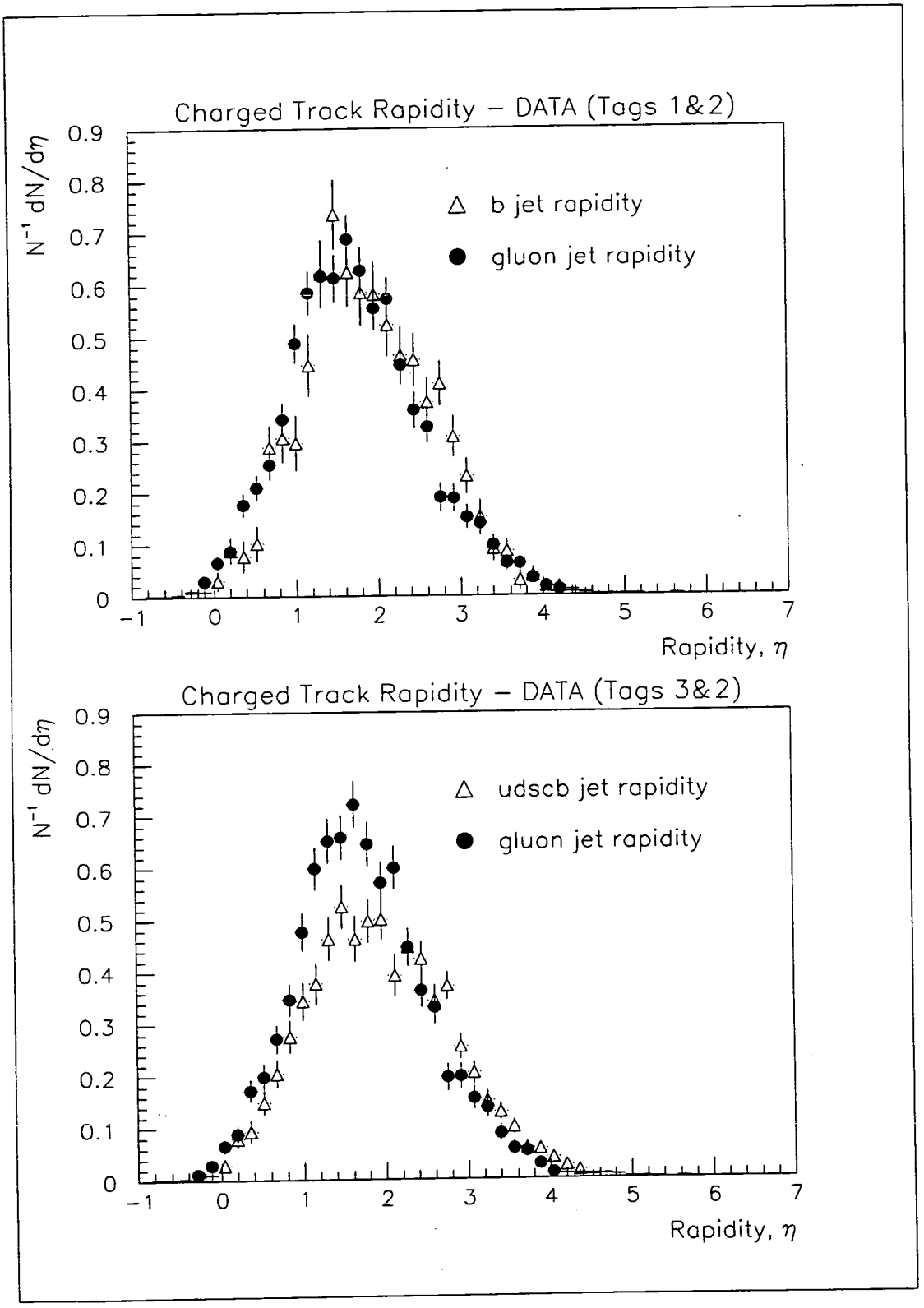


Figure 7.7: Charged track rapidity - real data

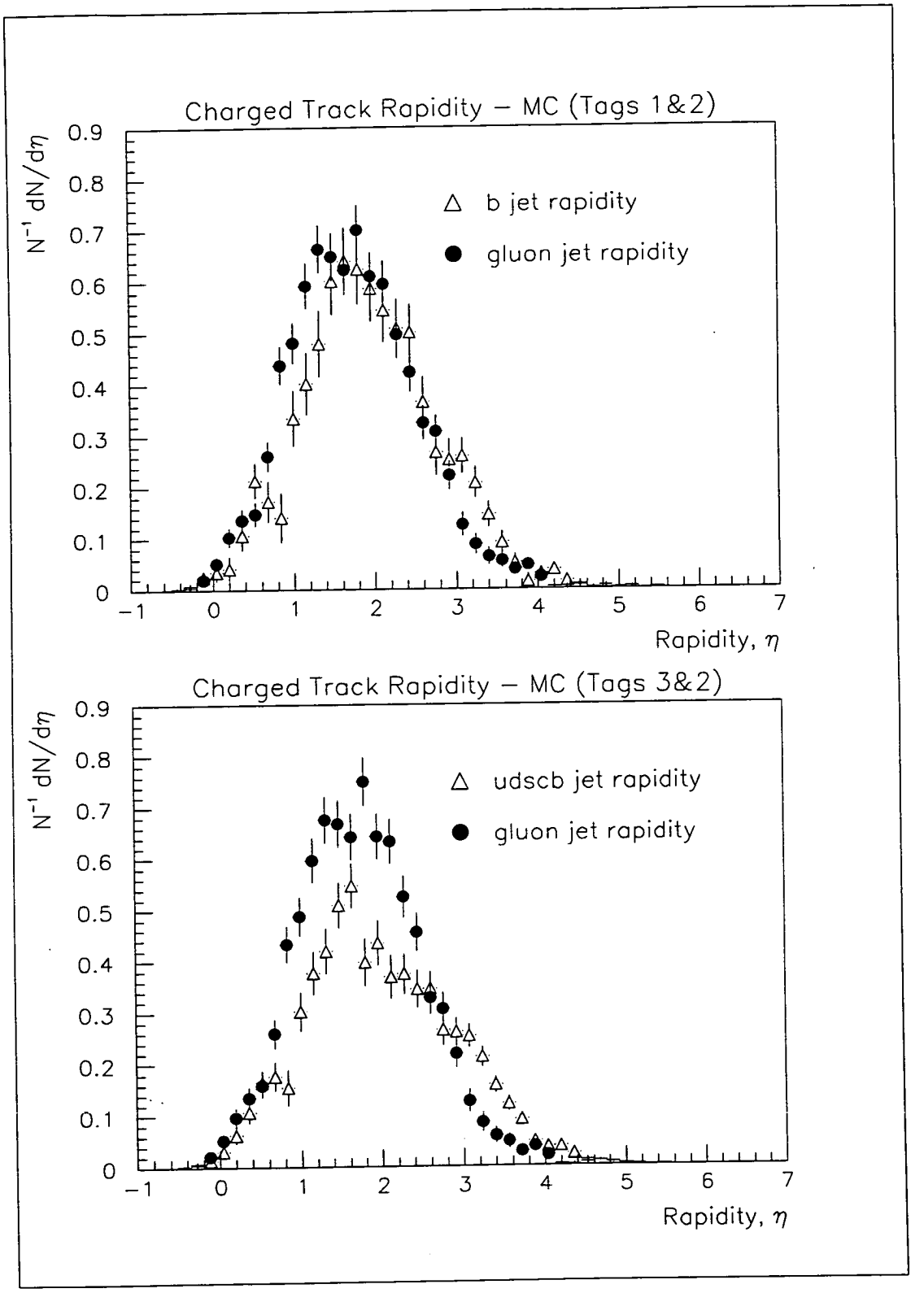


Figure 7.8: Charged track rapidity - Monte Carlo data

### 7.5.3 The fragmentation variable, $X_E$

The definition of the $X_E$ variable is straightforward. In this analysis it is defined as the ratio of a particle's energy to the energy of the jet to which it belongs:

$$X_E = \frac{E_{particle}}{E_{jet}} \tag{7.13}$$

The resulting distribution for a particular process is often referred to as the fragmentation function for that process although the proper definition of this is given by:

$$z = \frac{(E + P_{\|})_{hadron}}{(E + P_{\|})_{quark}} \tag{7.14}$$

Obviously, no experiment can measure the exact energy of the quark from whence the hadron originated therefore either the beam energy or, as in this case, the jet energy, is used. Since this measurement was concerned with the ratio of a particle's energy to that of its jet, the measured energy of the jet was used as opposed to the calculated energy. Therefore $\sum X_E = 1$.

Figures 7.9 and 7.10 show the distributions for real and Monte Carlo data whilst Figures 7.11 and 7.12 show the distributions for charged tracks and neutral objects. Note that the vertical axis is logarithmic in all cases. Taking the charged track Tag 1 and Tag 2 distributions first, there is a definite indication that the gluon fragmentation is "softer". This effect is enhanced further in the mixed flavour sample.

It is interesting to note that the Monte Carlo distributions, generated using the Peterson fragmentation function, get the quark distributions approximately correct whilst overestimating the "softness" of the gluon distribution. The energy flow algorithm again obscures any obvious jet differences in the real data. Having started from a position of over-estimation the Monte Carlo retains some of the difference.

Note that all distributions were normalised to the total number of particles in each data sample.

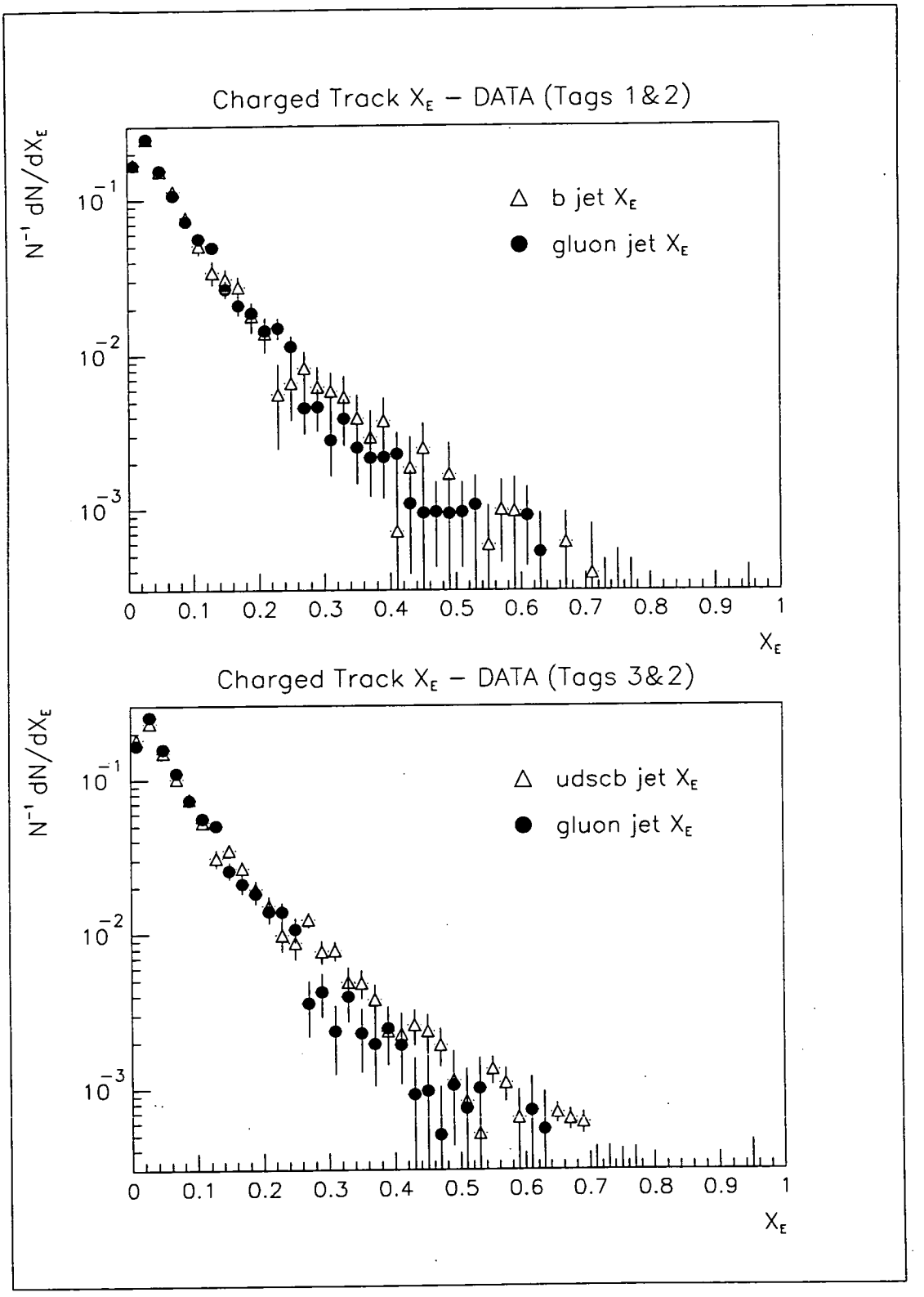


Figure 7.9: Charged track $X_E$ - real data

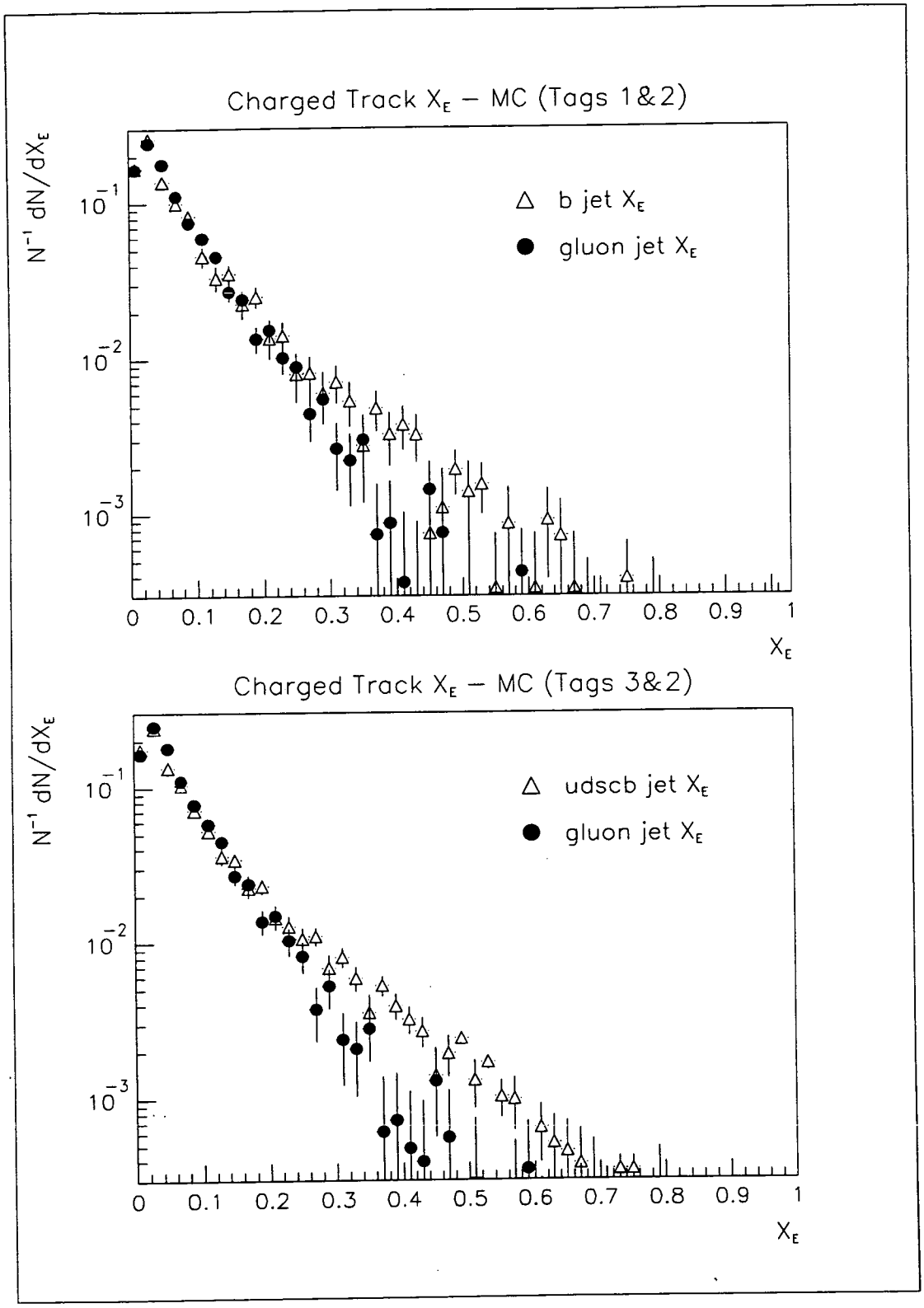


Figure 7.10: Charged track $X_E$ - Monte Carlo data

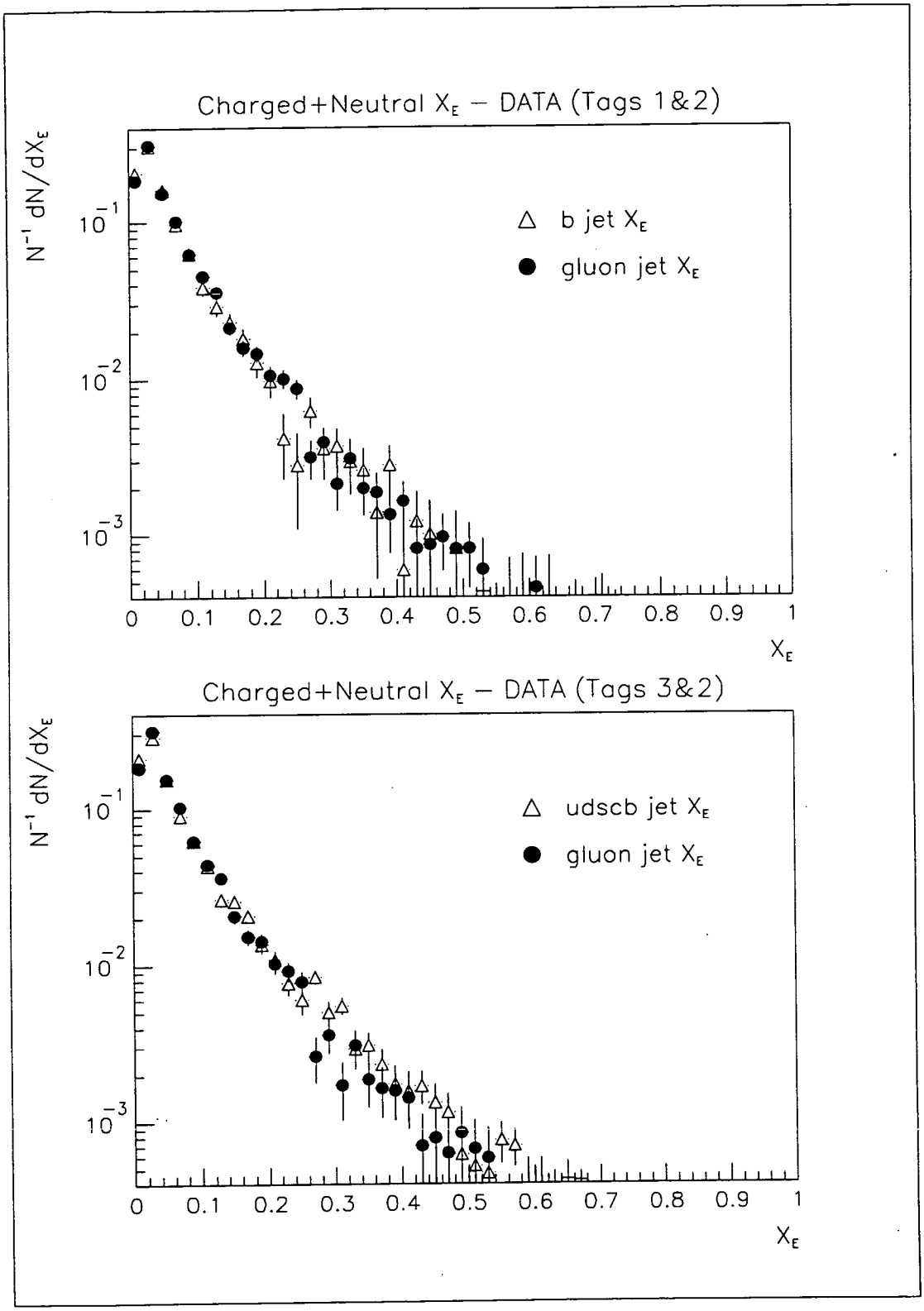


Figure 7.11: Charged track and neutral object $X_E$ - real data

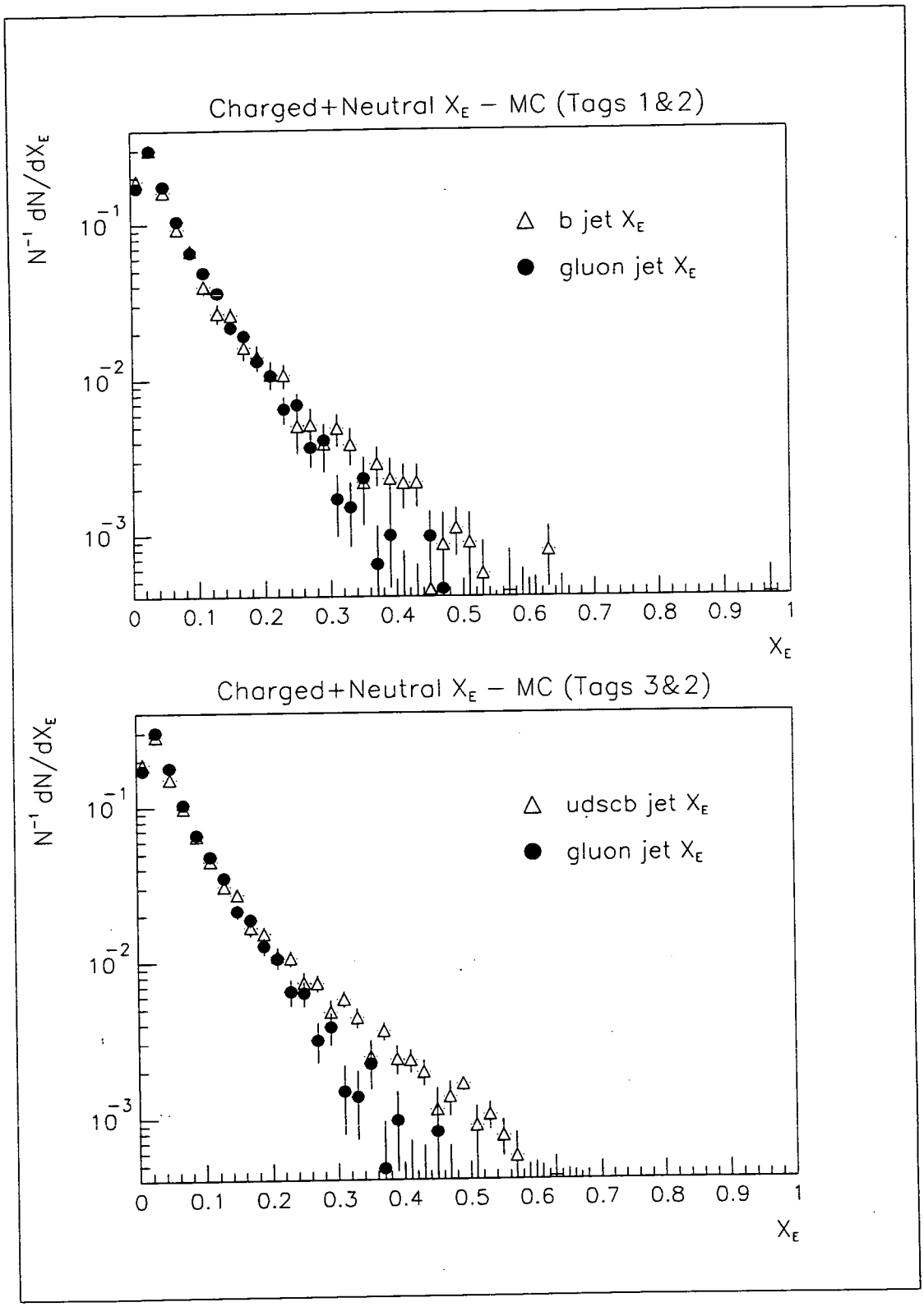


Figure 7.12: Charged track and neutral object $X_E$ - Monte Carlo data

### 7.5.4 $P_\perp$ in the jet

The preceding measurements have studied the longitudinal and fractional energy distributions of the jets. It was naturally interesting to look at the transverse momentum of the particles comprising each jet with respect to the jet axis. The prediction that quark jets should be "narrower" would suggest more particles with lower $P_\perp$ than the "wider" gluon jets.

It is not obvious from the real data distributions shown in Figure 7.13 that this is indeed the case. Although there is some indication that the number of particles with low $P_\perp$ is greater in the b-jet sample. This is not so apparent in the mixed flavour sample. Again the Monte Carlo distributions shown in Figure 7.14 over-estimate the possible differences between the quark and gluon samples.

The same distributions but using charged tracks and neutral objects give essentially the same results. All distributions were normalised to the total number of particles studied in each sample.

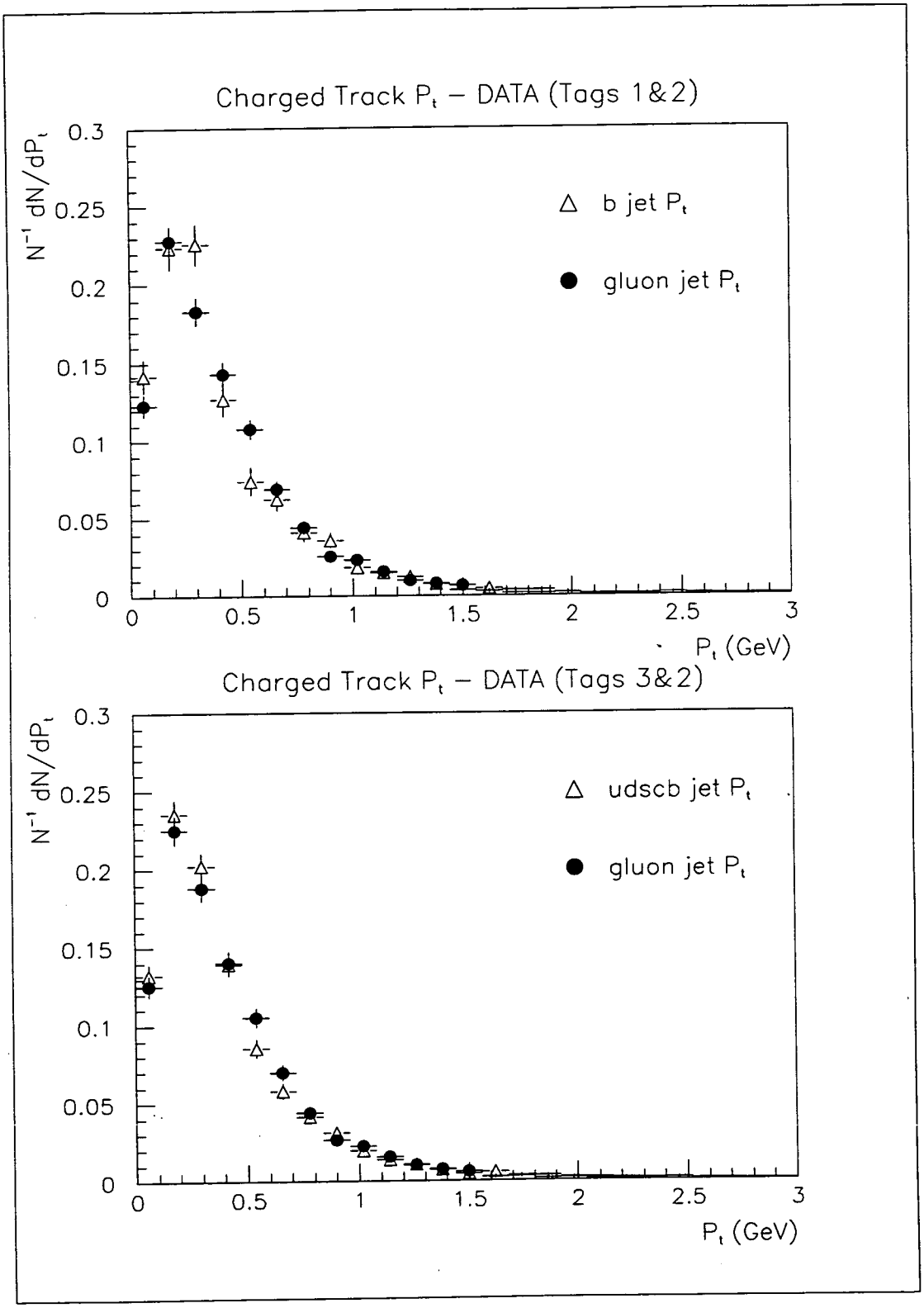


Figure 7.13: Charged track $P_\perp$ in the jet - real data

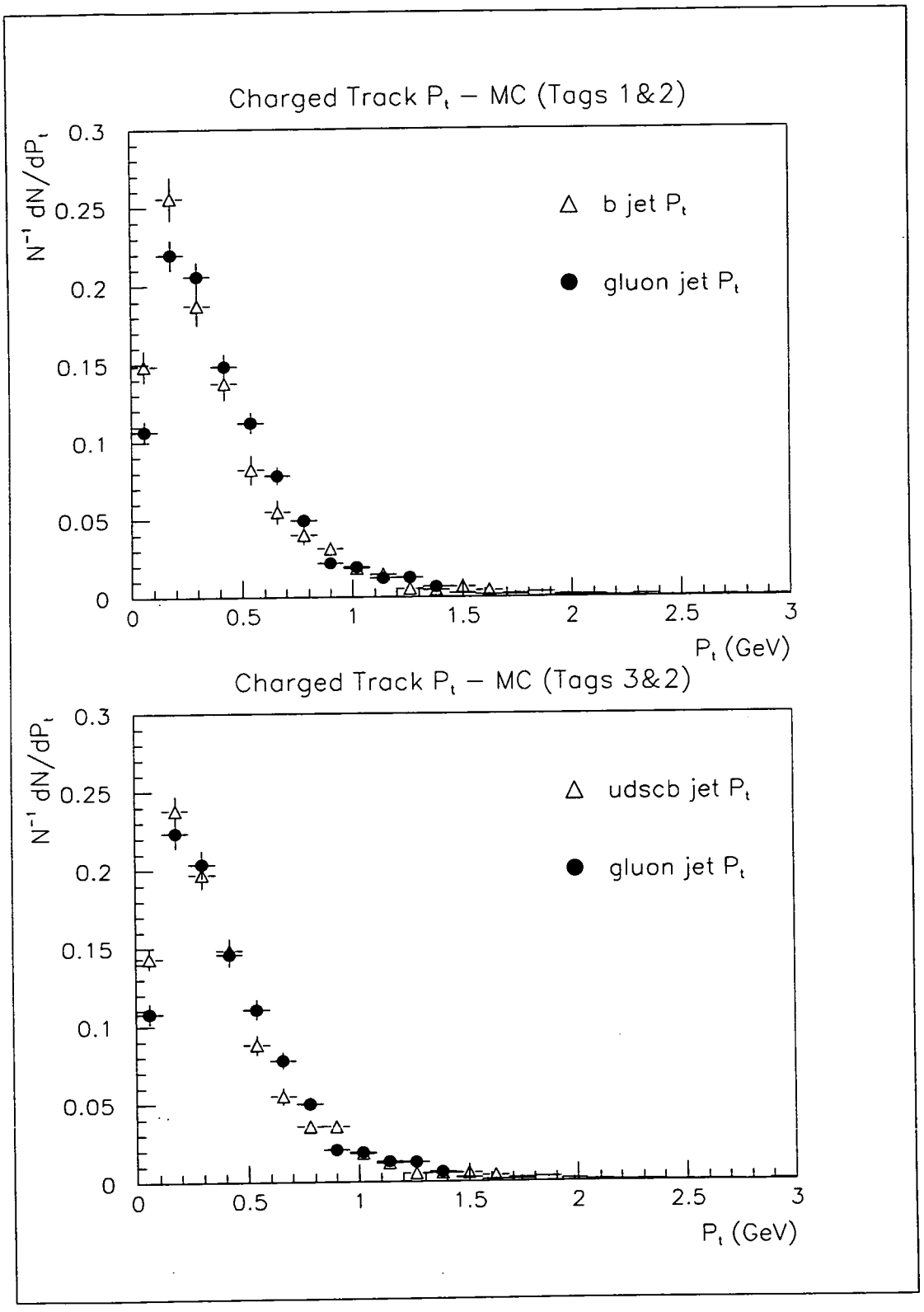


Figure 7.14: Charged track $P_\perp$ in the jet - Monte Carlo data

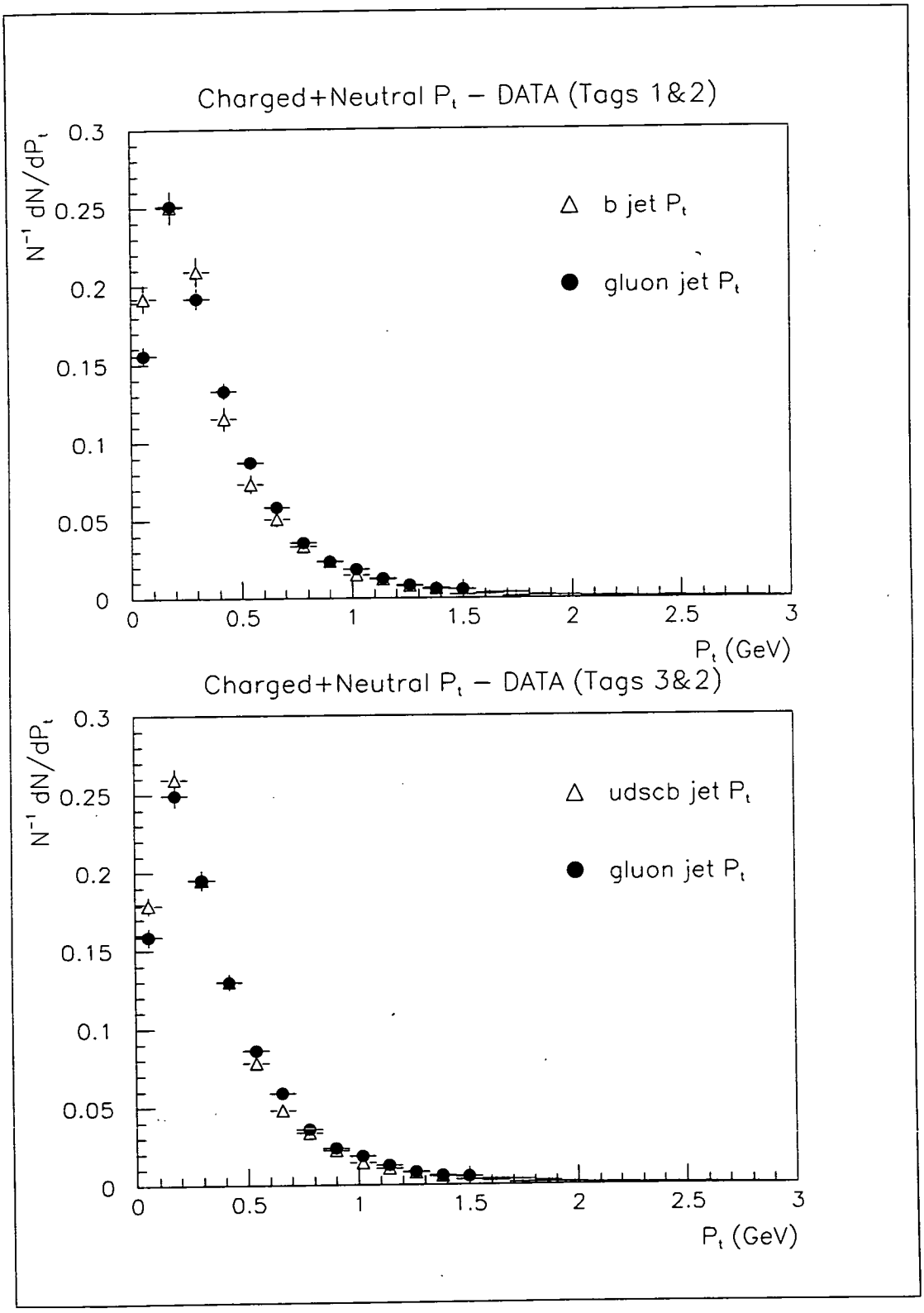


Figure 7.15: Charged track and neutral object $P_\perp$ in the jet - real data

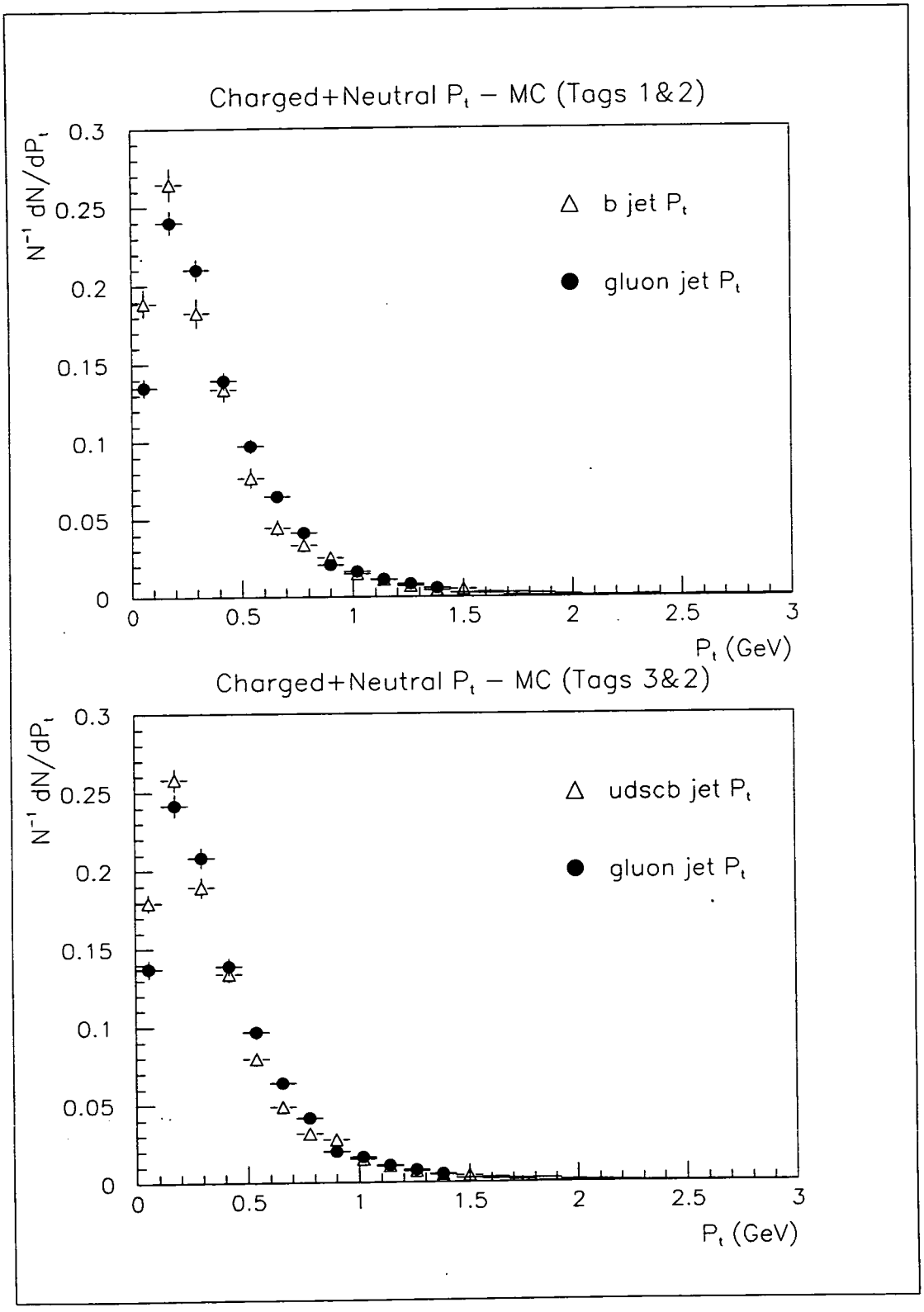


Figure 7.16: Charged track and neutral object $P_\perp$ in the jet - Monte Carlo data

### 7.5.5 Ratio of charged to neutral energy

The ratio of charged to neutral energy in quark and gluon jets was a measurement for which the only prediction was that there was no obvious reason why they should differ. It was nevertheless of interest to test this assumption.

The ratios were calculated by dividing the measured charged track energy in the jet by the measured neutral energy. As expected the real data distributions, shown in Figure 7.17 agree to within statistical error. However, there are certainly some points in the Monte Carlo distributions, particularly at low values of the ratio, which give cause for concern. Unfortunately no follow-up studies were possible.

Each distribution was normalised to the total number of jets in each data sample.

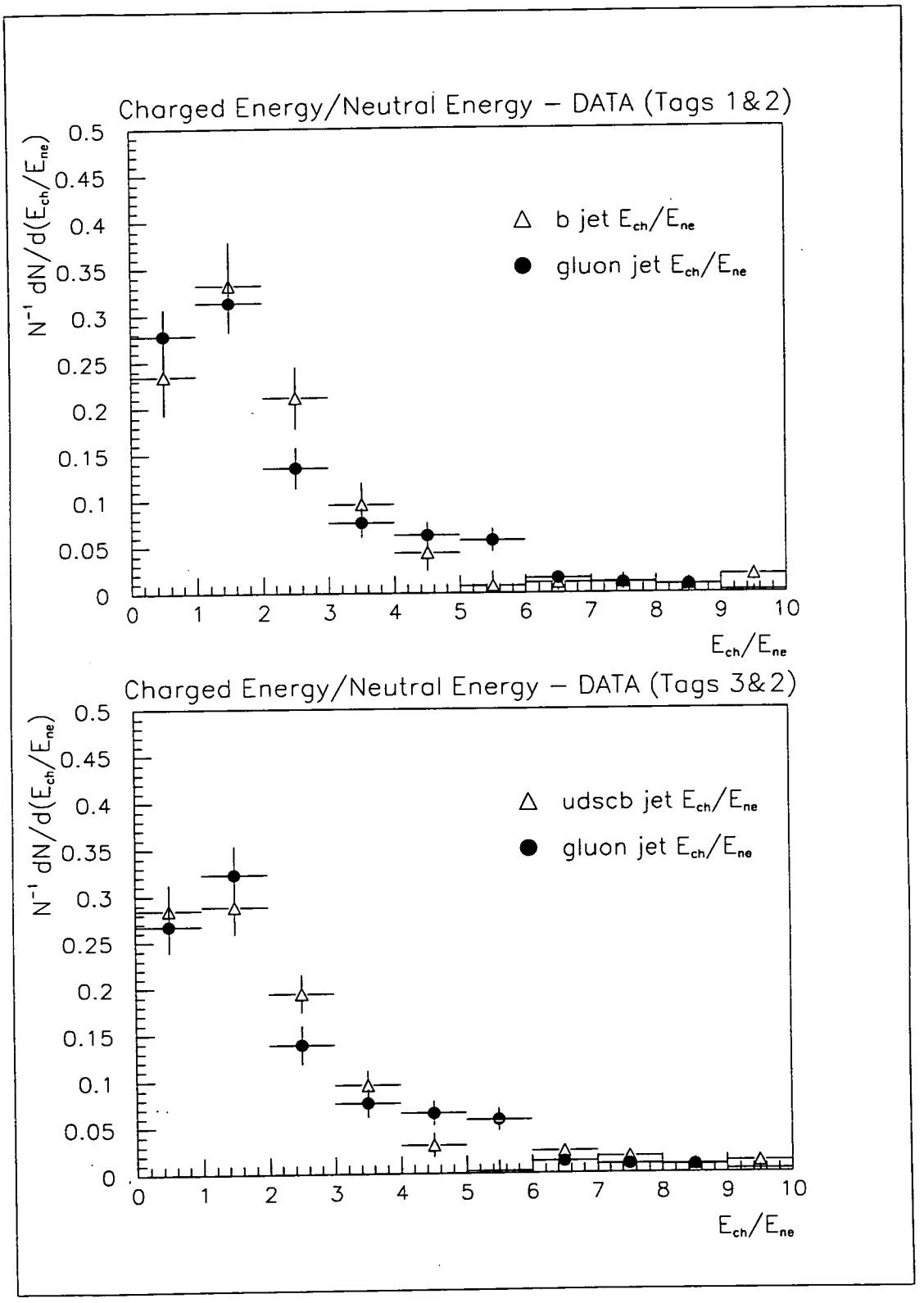


Figure 7.17: Ratio of charged energy to neutral energy - real data

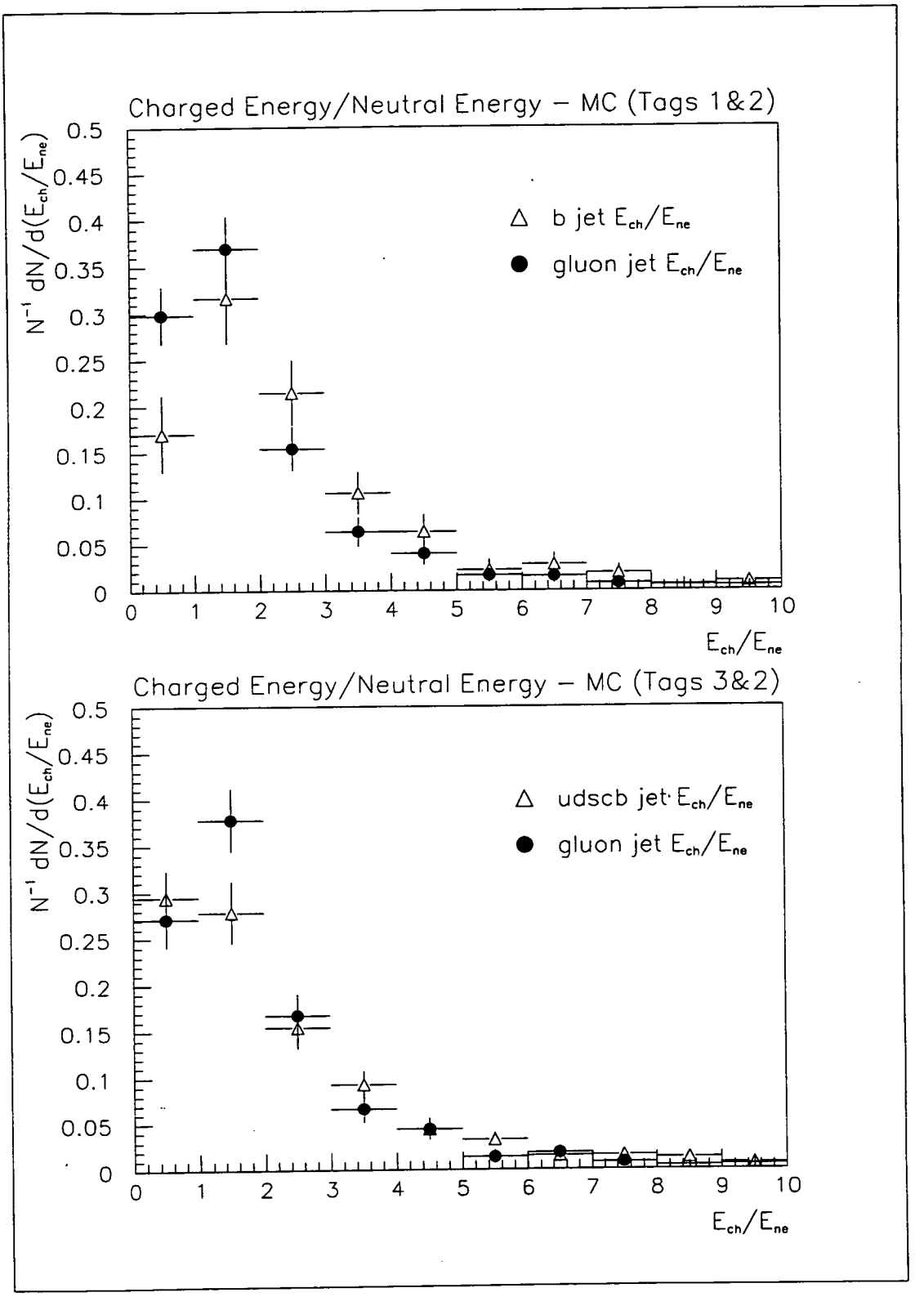


Figure 7.18: Ratio of charged energy to neutral energy - Monte Carlo data

### 7.5.6 Jet cone multiplicity

Only global properties of the selected quark and gluon jets have so far been described. A study was also made of the angular distribution of the particles within their jets.

To do this the number of charged tracks contained in a cone aligned along the jet axis and measured from $\theta$ to $\theta + 10^o$, where $\theta$ ranged from $0^o$ to $80^o$, were counted. The results for each angular section were then divided by the total number of charged tracks contained in the jet. These measurements were binned as shown in Figures 7.19 and 7.20 after global normalisation to the total number of jets in the sample.

The resulting histograms for real and Monte Carlo data are remarkably similar (in fact so similar that it is likely the Monte Carlo has been "tuned" to accurately reproduce the real data distributions). The b-jet and gluon distribution shows how the gluon jets are certainly wider than the quark jets. This effect is even more pronounced in the mixed flavour and gluon jet comparison.

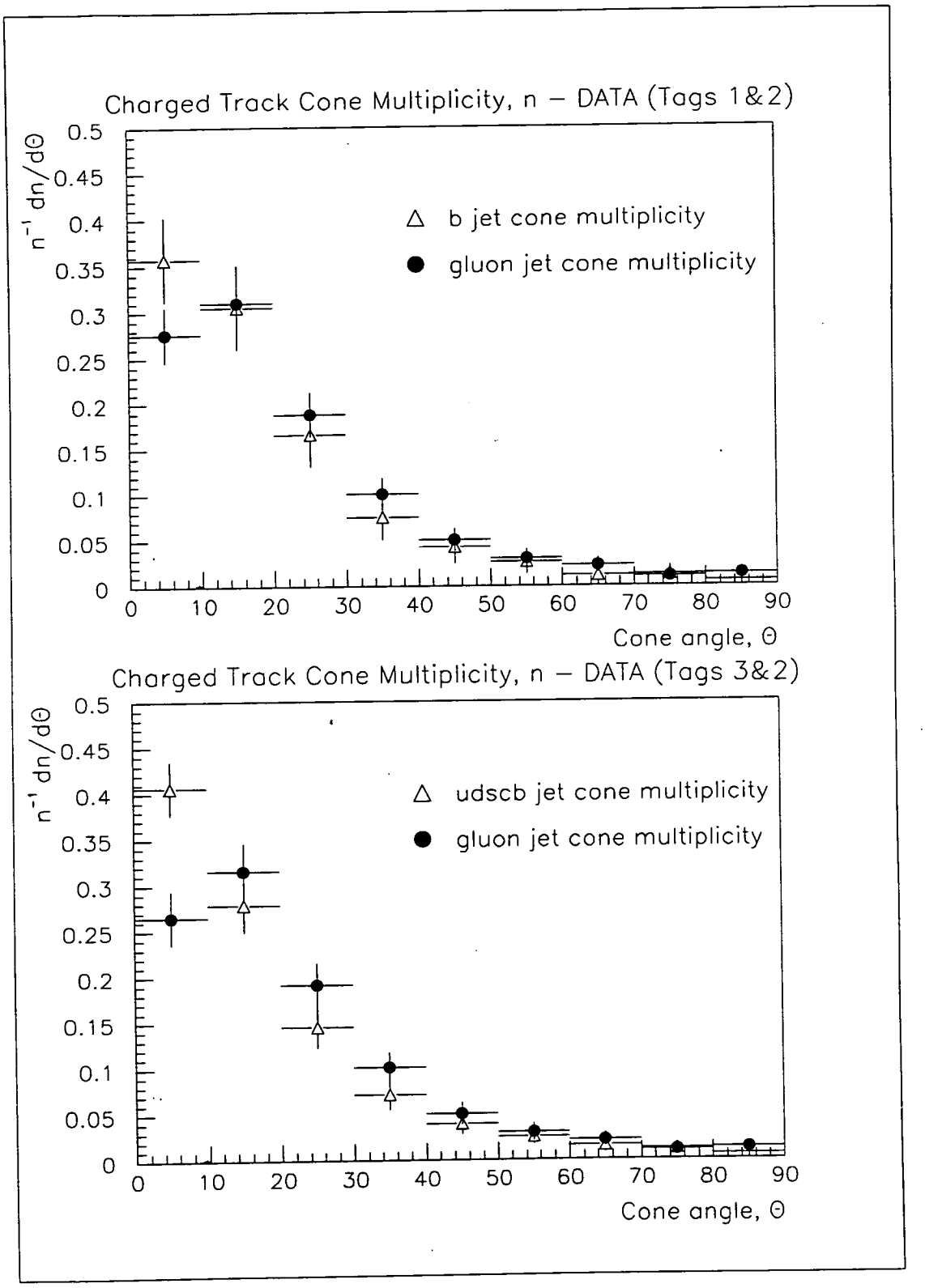


Figure 7.19: Jet cone charged track multiplicity - real data

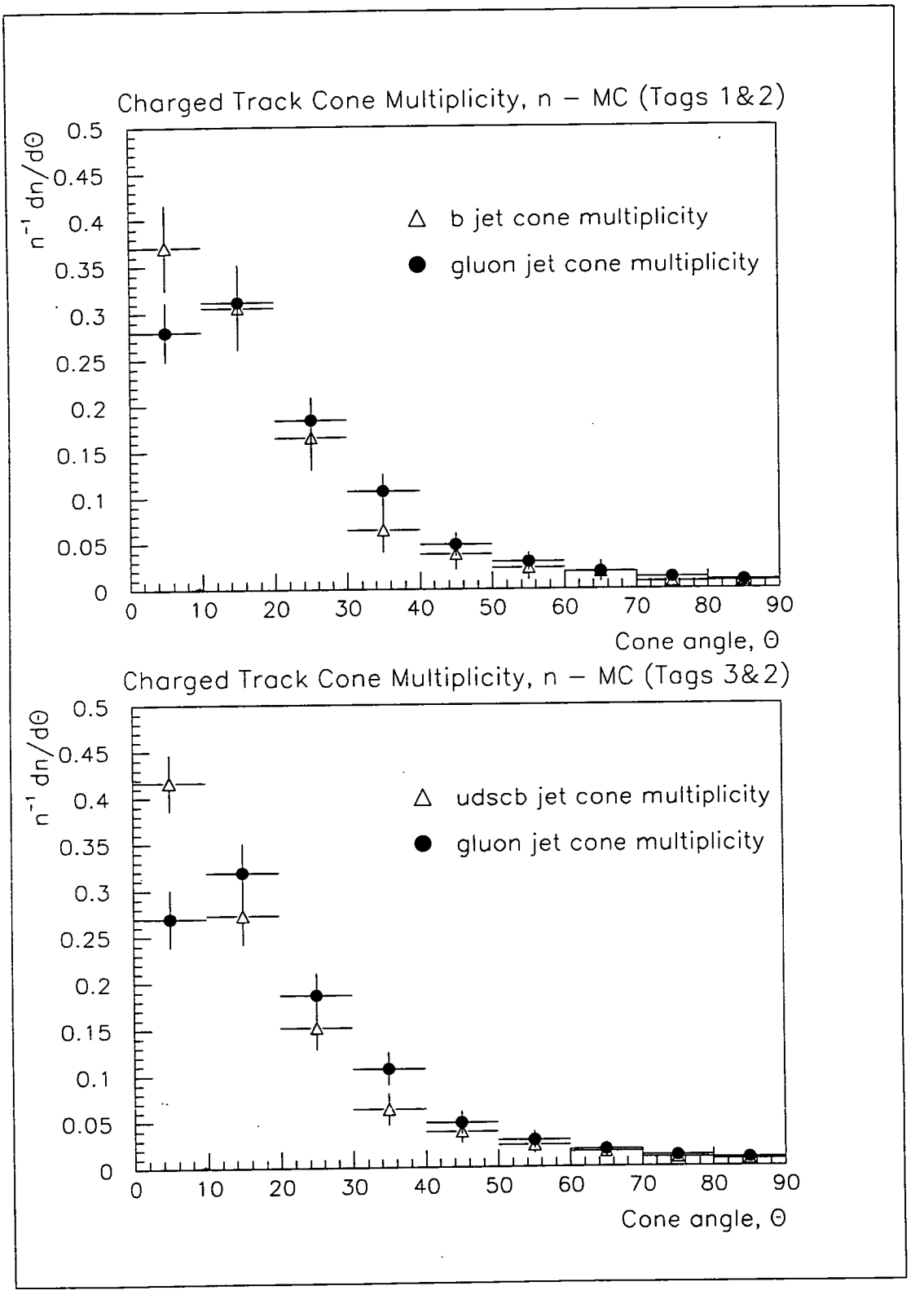


Figure 7.20: Jet cone charged track multiplicity - Monte Carlo data

### 7.5.7 Jet cone energy

Using exactly the same method as above the jet cone energy was measured. The energy of all charged and neutral particles contained in each jet cone was summed and then divided by the total measured jet energy. This provided a clear measurement of the jet energy profiles. The resulting distributions shown in Figures 7.21 and 7.22 were globally normalised to the number of jets in each sample.

Once again the Monte Carlo distributions are remarkably similar to the real data. Both demonstrate strikingly how the quark jets (particularly the mixed flavour sample) have a much more collimated profile than the wider gluon jets.

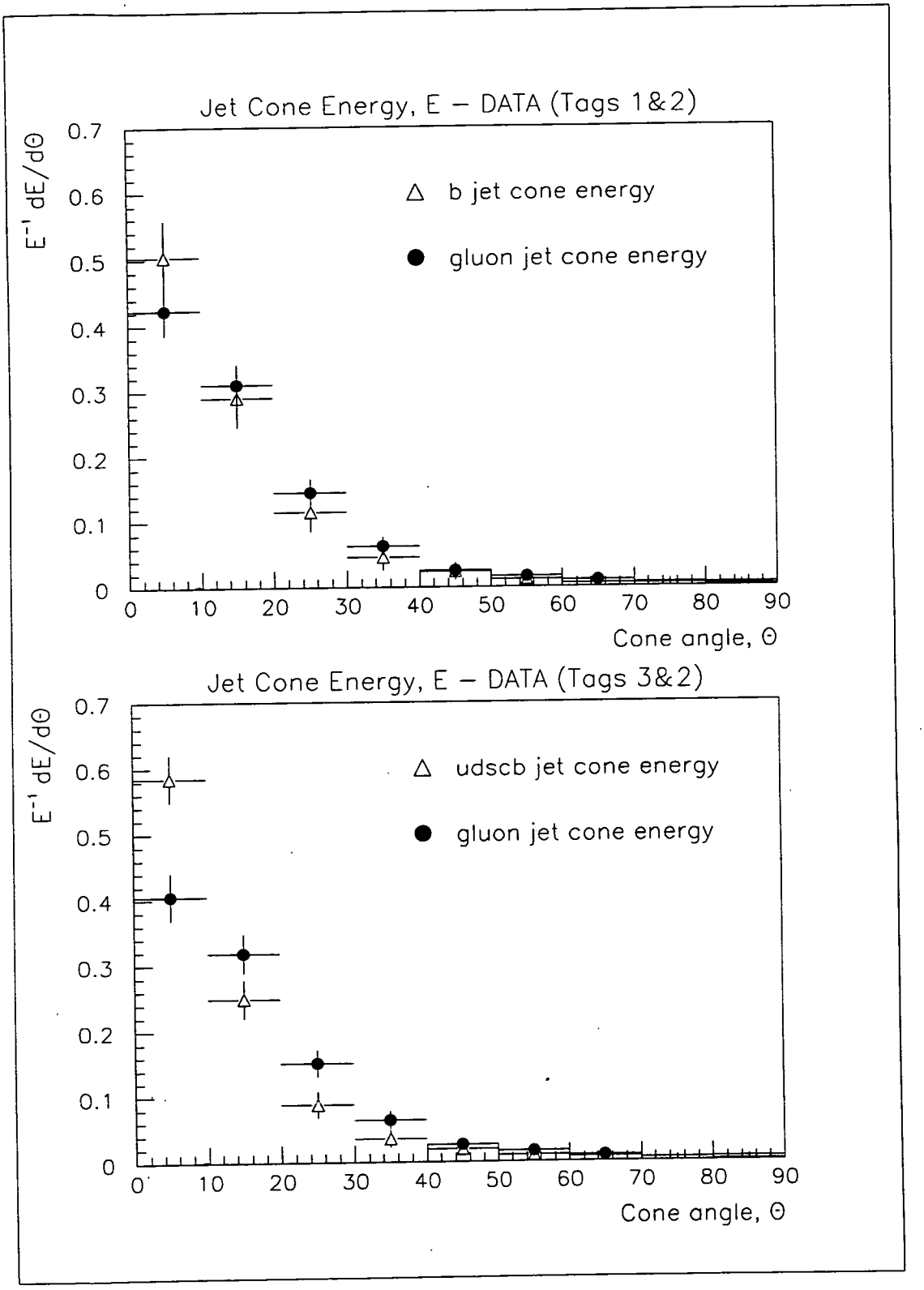


Figure 7.21: Jet cone energy fraction - real data

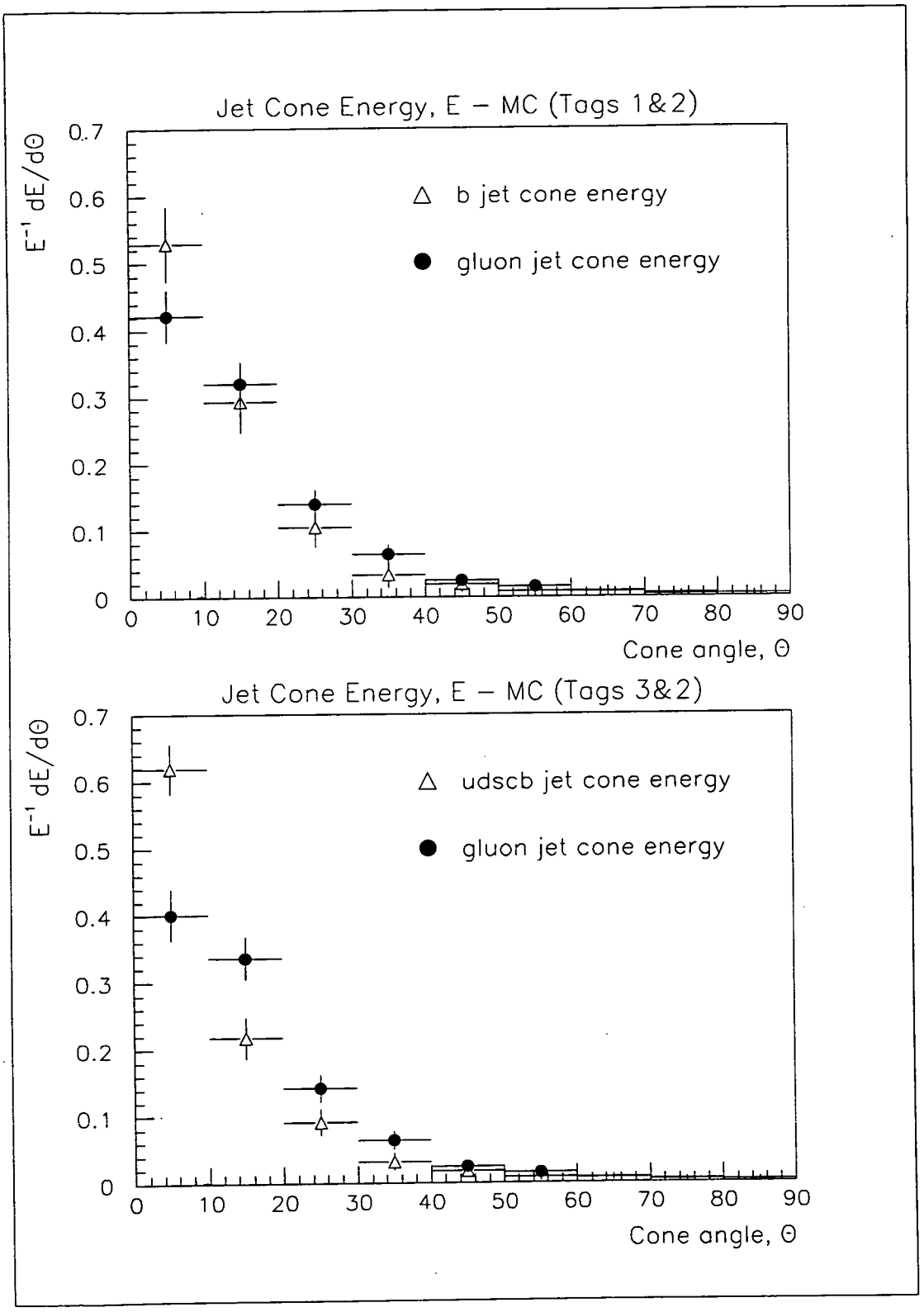


Figure 7.22: Jet cone energy fraction - Monte Carlo data

# Chapter 8

# Conclusions

This thesis has reported the definition and application of a method to identify the quark and gluon jets in 3-jet events using high $P_\perp$ lepton tagging. Two separate analyses have been described and their results presented. This short chapter reviews the two analyses and their final results.

## 8.1 The Dalitz Plot Analysis

An event sample of 3-jet events from the ALEPH 1990,1991, and 1992 data sets were selected. These events were required to contain two high $P_\perp$ leptons selected using the LEPTAG package and associated with separate jets, each with $P_\perp >$ 0.5GeV. The resulting flavour composition of the sample was found to be ~88% $b$-quark. The two jets containing the high $P_\perp$ leptons were identified as quark jets. The remaining jet was identified by default as a gluon jet. Using a carefully defined method, which relied on Monte Carlo parton level truth information, the purity of the gluon jet sample was found to be $(86 \pm 1 \pm 3)\%$. The first error is statistical, the second systematic. The assessed systematic error arose from those events where the truth information found the tag to be ambiguous.

By projecting the three jets onto the event plane, the energy of each jet was calculated. The variables $x_1 = \frac{2E_q}{E_{cm}}$ and $x_2 = \frac{2E_q}{E_{cm}}$ were constructed from the calculated quark jet energies and a 2-dimensional Dalitz plot was constructed. Plots for both real data and fully reconstructed ALEPH JETSET 7.3 parton

shower Monte Carlo were created using approximately the same number of events for each.

Comparing the real and Monte Carlo data distributions using a novel log-likelihood test, the two distributions were found to be the same with a confidence level of:

$$C.L. = 97\%. \tag{8.1}$$

Five generator level Monte Carlo data sets were compared with a benchmark JETSET 7.3 parton shower generator level sample. Of the other Monte Carlo data sets, only the matrix element scalar gluon model was found to be excluded by the prior result. It can be stated with certainty that a spin 0 gluon does not fit the measured data correctly and is therefore a bad hypothesis as a source for the strong interaction.

## 8.2 Quark and Gluon Jet Differences

The presence of a high $P_\perp$ lepton in a quark jet was found to bias the observable quantities. In this second analysis a method was devised to minimise all such biases. QCD predicts that quark and gluon jets should have small but measurable differences. However, exact theoretical predictions are not available due to the complexity of their calculation. For quark and gluon jets of the same energy, QCD predicts that the gluon jet particle multiplicity should be higher, a gluon jet should be wider than a quark jet , and the gluon jet should have a softer particle energy spectrum.

The analysis used a symmetric event configuration to ensure the lower energy quark and gluon jet had approximately the same energy. Three different tagging configurations were used and from these, observables were extracted by solving a simple set of simultaneous equations. Quark jet measurements for a $b$-quark rich sample and a mixed flavour sample were extracted. These were compared with gluon jet measurements extracted from the same data.

A large number of measurements were presented and it would serve no purpose to recapitulate each here. Instead, those results of particular interest which

were measured from the real data are mentioned.

Measuring the charged track multiplicity for $b$-jets and gluon jets provided an early surprise:

$$\begin{aligned} n_g &= 8.01 \pm 0.17 \\ n_q &= 7.98 \pm 0.27 \\ n_g/n_q &= 1.003 \pm 0.053 \end{aligned}$$

Instead of a higher gluon multiplicity, the two measurements were equal. Measuring the charged track multiplicity for a mixed flavour sample it was found that:

$$\begin{aligned} n_g &= 8.21 \pm 0.17 \\ n_q &= 7.07 \pm 0.17 \\ n_g/n_q &= 1.162 \pm 0.051 \end{aligned}$$

In this case the enhanced gluon jet multiplicity was clearly evident. It was postulated that the lack of a difference in the $b$-jet sample may be due to the additional multiplicity arising from the decay of the $B$ meson (also known as "non-leading fragmentation"). The mixed flavour result was found to be at odds with a similar result published by the OPAL collaboration. No reason was discovered to explain this discrepancy.

The same measurement was made using both charged tracks and neutral objects. The observed difference between the jets was markedly reduced. It was suggested that this may be caused by the inherent granularity of the neutral object determination of the energy flow algorithm and therefore, any measurements which used these objects should be treated with caution.

Identical measurements were repeated using Monte Carlo data and showed that the fully reconstructed JETSET 7.3 events were overestimating the quark-gluon jet differences.

By measuring the charged track rapidity it was hoped to show that quark jets contained more particles whose longitudinal momentum with respect to the jet axis was large. The gluon jets were expected to contain fewer such particles and hence exhibit lower average values of rapidity. The mixed flavour quark jet and gluon jet rapidity measurements confirmed this hypothesis, albeit with less

dramatic differences than might have been expected. Much smaller differences between the $b$-jet and gluon jet distributions were discernable. Again this was attributed to the non-leading fragmentation.

The fragmentation variable, $X_E = \frac{E_{particle}}{E_{jet}}$ was expected to show that gluon jet fragmentation was softer than that of a quark jet due to the gluon's enhanced colour charge. The charged track $b$-jet and gluon jet measurements indicated that gluon jets might be slightly softer. This effect was further enhanced in the mixed flavour quark and gluon jet comparison. Again, the Monte Carlo overestimated the differences. Using charged and neutral objects, no discernable difference was evident between the distributions.

The suggestion that quark jets should be narrower implies lower average values of particle transverse momentum in such a jet. This variable was studied for charged tracks and charged tracks and neutral objects. Whilst there was some indication that the $b$-jet particles had lower average values of $P_\perp$, this result was by no means conclusive. The mixed flavour quark and gluon jet comparison showed essentially identical distributions of $P_\perp$ for both jet types.

As expected the distributions of the ratio of charged to neutral energy in quark and gluon jets were found to be identical.

The final two measurements provided the most direct proof that gluon jets are softer and wider than quark jets. Measuring the charged track multiplicity in a series of cones aligned along the jet axis resulted in very different distributions for the quark and gluon jets. The quark jet contains significantly more of its particles in the first $10^\circ$ cone than a gluon jet.

The same method was used to measure the total energy of the particles in each cone. The quark jets were found to contain significantly more of their energy in the first $10^\circ$ cone than the gluon jets. In addition, the gluon jets exhibited a wider spread of energy across the jet profile.

In both measurements the effects were most pronounced in the mixed flavour jet and gluon jet comparison but they are still clearly visible in the $b$-jet and gluon jet plots. The Monte Carlo modelled both of these distributions particularly well.

## 8.3 Concluding Remarks

The method of tagging quark jets in 3-jet events using high $P_\perp$ leptons has been shown to be a useful and powerful tool. The Dalitz plot analysis has shown that the angular distribution of quark jets in 3-jet events is well described by the JETSET Monte Carlo program which is based on the principles of quantum chromodynamics. The Abelian scalar gluon model has been excluded. The symmetric event study has shown that, although small, measurable differences between quark and gluon jets of the same energy do exist. Gluon jets are wider and have a softer particle energy spectrum than quark jets.

The present mathematical formalism of quantum chromodynamics precludes the prediction of accurate numerical values for the measurable quark and gluon jet differences. It is hoped that values obtained for these differences in this study can be used to improve the present JETSET Monte Carlo predictions which tend to overestimate them.

Only time will tell if the Monte Carlo models now used to generate hadronic events at LEP truly represent reality. It is strongly believed that progress in our understanding of fragmentation will only be made gradually through experimental studies such as have been presented here.

# Appendix A

# Proof of the log-likelihood method

This Appendix presents the derivation of the log-likelihood test used in the Dalitz plot analysis of Chapter 6.

Given a distribution of N bins there is a probability $p_i$ associated with each bin that an entry falls in bin $i$. $p_i$ is constrained by

$$\sum_{i=1}^{N} p_i = 1. \tag{A.1}$$

In a sample of $D$ entries, $d_i$ are found to fall into the $i^{th}$ bin.

$$D = \sum_{i=1}^{N} d_i. \tag{A.2}$$

From Bayes theorem, given a set of values $d_i$, the likelihood of a set of probabilities being correct is $L$ where

$$\ln L = \sum_{i=1}^{N} d_i \ln p_i. \tag{A.3}$$

Maximising Equation A.3 subject to the constraint given in Equation A.1 gives the unsurprising result that

$$p_i = \frac{d_i}{D}. \tag{A.4}$$

Now, consider two sets of data, D and M (where D can be thought of as the real data distribution and M the Monte Carlo distribution) then

$$\ln L = \sum_{i=1}^{N} (d_i \ln p_i + m_i \ln q_i) \tag{A.5}$$

where $q_i = \frac{m_i}{M}$ by the same argument as above. This has a maximum value of

$$\ln L_0 = \sum_{i=1}^{N} \left[ d_i \ln \left( \frac{d_i}{D} \right) + m_i \ln \left( \frac{m_i}{M} \right) \right]. \tag{A.6}$$

If it is desired to test that the underlying probability distributions are the same (ie. $p_i = q_i$), then the maximum likelihood is given by

$$r_i = \frac{d_i + m_i}{D + M}, \tag{A.7}$$

$$\Rightarrow \ln L_1 = \sum_{i=1}^{N} \left[ (d_i + m_i) \ln \left( \frac{d_i + m_i}{D + M} \right) \right]. \tag{A.8}$$

The log-likelihood test can therefore be constructed from these likelihoods and is given by

$$\ln L_0 - \ln L_1 = \sum_{i=1}^{N} \left[ d_i \ln \frac{d_i(D+M)}{(d_i + m_i)D} + m_i \ln \frac{m_i(D+M)}{(d_i + m_i)M} \right]. \tag{A.9}$$

This can also be written as

$$\begin{aligned} \ln L_0 - \ln L_1 \;=\; & \sum_{i=1}^{N} \left[ d_i \ln \left\{ 1 + \left( \frac{d_i}{D} - \frac{m_i}{M} \right) \frac{M}{d_i + m_i} \right\} + \right. \\ & \left. m_i \ln \left\{ 1 - \left( \frac{d_i}{D} - \frac{m_i}{M} \right) \frac{D}{d_i + m_i} \right\} \right]. \end{aligned} \tag{A.10}$$

If $D$ and $M$ are $\gg d_i$ and $m_i$ then the above equation approximates to

$$\begin{aligned} \ln L_0 - \ln L_1 \;\simeq\; & \sum_{i=1}^{N} \left[ d_i \left( \frac{d_i}{D} - \frac{m_i}{M} \right) \frac{M}{d_i + m_i} - \right. \\ & \left. m_i \left( \frac{d_i}{D} - m_i M \right) \frac{D}{d_i + m_i} \right] \end{aligned} \tag{A.11}$$

$$= \sum_{i=1}^{N} \left[ \left( \frac{d_i}{D} - \frac{m_i}{M} \right) \left( \frac{d_i M - m_i D}{d_i + m_i} \right) \right] \tag{A.12}$$

$$= \sum_{i=1}^{N} \left[ \left( \frac{d_i}{D} - \frac{m_i}{M} \right) \left( d_i \frac{MD}{D} - m_i \frac{DM}{M} \right) \left( \frac{1}{d_i + m_i} \right) \right] \tag{A.13}$$

$$= \sum_{i=1}^{N} \left[ \left( \frac{d_i}{D} - \frac{m_i}{M} \right)^2 \left( \frac{DM}{d_i + m_i} \right) \right]. \tag{A.14}$$

If it is now assumed that $D = M$ then it follows that

$$\sum_{i=1}^{N} \left[ \left( \frac{d_i}{D} - \frac{m_i}{M} \right)^2 \left( \frac{DM}{d_i + m_i} \right) \right] = \sum_{i=1}^{N} \frac{(d_i - m_i)^2}{d_i + m_i} \equiv \frac{\chi^2}{2}. \tag{A.15}$$

# Bibliography


[1] D. Abbaneo, L. Bellantoni, P. Dornan, A. Falvard, F. Ligabue, P. Perret, and R. Tenchini. Lepton and jet definitions for the lepton paper. ALEPHnote 92-101, ALEPH, 1992.

[2] G. Altarelli, R. Kleiss, and C. Verzegnassi, editors. *Z Physics at LEP 1*, volume 1. CERN, 1989. CERN 89-08.

[3] B. Bloch-Devaux. A new measurement of the Z peak cross-section using a high precision silicon-tungsten luminosity calorimeter (SiCAL) in ALEPH. ALEPHnote 93-178, ALEPH, 1993.

[4] A. Blondel and E. Blucher. Hadronic event selection with charged tracks. ALEPHnote 90-171, ALEPH, 1990.

[5] M. Bowler. *Femtophysics.* Pergamon Press, 1990.

[6] J. C. Brient, S. Orteu, A. Rougé, and M. Verderi. A method for photon reconstruction in ALEPH. ALEPHnote 93-107, ALEPH, 1993.

[7] L. S. Brown, D. L. Nordstrom, and S. G. Brown, editors. *Physical Review D, Review of Particle Properties*, volume 45. The American Physical Society, June 1992.

[8] N. Brown and W. J. Stirling. Jet cross sections at leading double logarithm in $e^+e^-$ annihilation. *Physics Letters B*, 252:657–662, 1990.

[9] N. Brown and W. J. Stirling. Finding jets and summing soft gluons: a new algorithm. *Zeitschrift für Physik C*, 53:629–636, 1992.

[10] O. Callot. *ALEPH Shift Crew Training Course.* ALEPH, May 1992.

[11] O. Callot. *ALEPH Shift Leader Training Course.* ALEPH, June 1992.

[12] D. Casper. ALEPH 101 - an introduction to the ALEPH offline system. ALEPHnote 93-026, ALEPH, 1993.

[13] S. Catani, Yu. L. Dokshitzer, M. Olson, G. Turnock, and B. R. Webber. New clustering algorithm for multijet cross sections in $e^+e^-$ annihilation. *Physics Letters B*, 269:432–438, 1991.

[14] S. Catani, B. Webber, Y. Dokshitzer, and F. Fiorani. Average multiplicities in two- and three-jet $e^+e^-$ annihilation events. CERN-TH 6419/92, CERN, 1992.

[15] D. Cinabro, R. Johnson, and V. Sharma. Fitting the $b\bar{b}$ asymmetry from the spectrum of prompt leptons. ALEPHnote 91-35, ALEPH, 1991.

[16] ALEPH Collaboration. The ALEPH handbook 1989. ALEPHnote 89-077, ALEPH, 1989.

[17] ALEPH Collaboration. Properites of hadronic Z decays and test of QCD generators. *Zeitschrift für Physik C*, 55:209–234, 1992.

[18] ALEPH Collaboration. Heavy flavour production and decay with prompt leptons in the ALEPH detector. CERN-PPE 94-017, CERN, 1994.

[19] ALEPH Collaboration. Heavy quark tagging with leptons in the ALEPH detector. CERN-PPE 94-023, CERN, 1994.

[20] CDF Collaboration. Evidence for top quark production in $p\bar{p}$ collisions at $\sqrt{s} = 1.8TeV$. FERMILAB PUB 94 116-E, Fermilab, 1994.

[21] Mark II Collaboration. Charged multiplicity of hadronic events containing heavy quark jets. *Physical Review Letters*, 54(24):2580–2583, 1985.

[22] Mark II Collaboration. Studies of jet production rates in $e^+e^-$ annihilation at $E_{cm} = 29GeV$. *Zeitschrift für Physik C*, 43:331–340, 1989.

[23] OPAL Collaboration. A study of differences between quark and gluon jets using vertex tagging of quark jets. *Zeitschrift für Physik C*, 58:387–404, 1993.

[24] P. Colrain, A. Halley, I. ten Have, M. Parsons, B. Maitland, and M. Smith. The BTAGDST: A data set for heavy flavour analyses based on the miniDST. ALEPHnote 92-150, ALEPH, 1992.

[25] G. Cowan, April 1994. Private e-mail correspondence.

[26] G. Dissertori. A study of the 3-jet Dalitz plot. ALEPHnote 94-041, ALEPH, 1994.

[27] M. Einhorn and B. Weeks. Jet production by a gluon source in QCD. *Nuclear Physics B*, 146:445–456, 1978.

[28] J. Ellis, M. Gaillard, and G. Ross. Search for gluons in $e^+e^-$ annihilation. *Nuclear Physics B*, 111:253–271, 1976.

[29] D. Decamp et al. ALEPH: A detector for electron-positron annihilations at LEP. *Nuclear Instruments and Methods*, A294:121–178, 1990.

[30] E. Veitch et al. Online monitoring in the ALEPH experiment at LEP. ALEPHnote 92-170, ALEPH, 1992.

[31] G. Batignani et al. Recent results and running experience of the new ALEPH vertex detector. ALEPHnote 91-158, ALEPH, 1991.

[32] P. D. Acton et al. A study of differences between quark and gluon jets using vertex tagging of quark jets. CERN-PPE 93-02, CERN, 1993.

[33] B. Foster, editor. *Electron-Positron Annihilation Physics.* Adam Hilger, 1990.

[34] G. Hanson et al. Evidence for structure in hadron production by $e^+e^-$ annihilation. *Physical Review Letters*, 35:1609–1612, 1975.

[35] R. Gilmore. *Single Particle Detection and Measurement.* Taylor & Francis, 1992.

[36] S. Glashow, J. Illipoulos, and L. Maiani. Weak interactions with lepton-hadron symmetry. *Physical Review D*, 2:1285, 1970.

[37] B. Ioffe. Associated production of gluonic jets and heavy mesons in $e^+e^-$ annihilation. *Physics Letters B*, 78:277–280, 1978.

[38] JADE Collaboration. Experimental studies on multi-jet production in $e^+e^-$ annihilation at PETRA energies. *Zeitschrift für Physik C*, 33:23–31, 1986.

[39] F. James. Random numbers according to any histogram. Short program writeup V150, CERN, 1978.

[40] P. Janot. Performance of the ALEPH detector at LEP [Section 9]. Draft alephnote, ALEPH, 1993.

[41] V. Khoze. On the profiles of jets initiated by light and heavy quarks. SLAC-PUB 5909, SLAC, 1992.

[42] K. Konishi, A. Ukawa, and G. Veneziano. A simple algorithm for QCD jets. *Physics Letters B*, 78:243–248, 1978.

[43] E. Lançon, P. Perez, and F. Perrier. Photons in hadronic events. ALEPH-note 90-066, ALEPH, 1990.

[44] J. Lees. About the lepton $P_\perp$ definition. ALEPHnote 92-51, ALEPH, 1992.

[45] G. Marchesini, B. R. Webber, G. Abbiendi, I. G. Knowles, M. H. Seymour, and L. Stance. HERWIG: a monte carlo event generator for simulating hadron emission reactions with interfering gluons (version 5.1 - april 1991). *Computer Physics Communications*, 62:465–, 1992.

[46] S. Myers and E. Picasso. The design, construction and commissioning of the CERN Large Electron-Positron collider. *Contemporary Physics*, 31(6):387–403, 1990.

[47] H. Nilles and K. Streng. Quark-gluon separation in three-jet events. *Physical Review D*, 23(9):1944–1950, 1981.

[48] M. Parsons and I. ten Have, February 1993. LEPTAG Version 3.21 user documentation stored in UPHY.DOC.

[49] D. Schlatter, G. Redlinger, and P. Perrodo. ALEPH in numbers. ALEPH-note 93-058, ALEPH, 1993.

[50] K. Shizuya and S. Tye. Gluon jets from quantum chromodynamics. *Physical Review Letters*, 41(12):787–791, 1978.

[51] T. Sjöstrand. QCD and jets at LEP. CERN-TH 5902/90, CERN, 1990.

[52] W. J. Stirling. Hard QCD working group - theory summary. In *Workshop on Jet Studies at LEP and HERA*, pages B49–B61, 1991.

[53] T. Sjöstrand. PYTHIA 5.6 and JETSET 7.3, physics and manual. CERN Report CERN-TH.6488/92, CERN, 1992.

[54] B. R. Webber, September 1993. Private e-mail correspondence.

[55] M. Worris. *Measurements of the B meson semileptonic branching function.* PhD thesis, Cornell University, 1991.